Cracking the calcium code: modelling molecular determinants of calcium signalling in health and disease

Molly Ann Hawker

A thesis submitted in partial fulfilment of the requirements of Liverpool John Moores University for the degree of Doctor of Philosophy

April 2024

Declaration

I declare that no portion of the work referred to in this thesis has been submitted in support of an application for another degree or qualification of this or any other university or other institute of learning

Molly Ann Hawker

Date: 22/04/2024

Acknowledgements

I would first like to thank my supervisors, Ivo, Ross, Pengxing and James for your continued support and Liverpool John Moores University for funding my PhD. Ivo, thank you for always believing in me. You have supported me so much throughout the past three years, listened to my concerns and celebrated every success. Ross, Pengxing and James thank you for all the advice and knowledge you have shared. A special thank you to Jo and Victoria from the Doctoral Academy. The sessions you put on and the support you give to PhD students are invaluable and made a huge difference to my PhD journey. Amer, thank you for always being a friendly face when I was in the office. Saul, thank you for instilling belief in me when it was often lost.

To my friends, Hannah, Katie and Charlotte. I am so lucky to have met you during our undergraduate degree, thank you for always being there to listen to me during our catch-ups. Martha, soon to be Dr Joddrell, for keeping in touch despite the long distance. Ol, for all your support.

I would not have been able to complete this PhD without the uncon-

ditional love and endless support of my family. To my parents, thank you for always listening to me, for sitting through endless practice presentations, celebrating all the wins and always showing an interest in my work. To Neil and Liz, thank you for being there for me during my moments of panic and worry and calming me down. To Em, thanks for all the adventures, walks, kitchen discos and car karaoke over the past three years - I hope we plan many more. Maeve, being your auntie has brought so much joy to my life. I always look forward to your visits when I am working. Lyd, thank you for always encouraging me. To my Nanny Lena, you never got to see me finish my PhD, but I am eternally grateful for all the love you gave me. Nan and Grandad, thank you for your love, support and countless Sunday dinners.

This thesis is dedicated to my family.

Abstract

The release of calcium ions into the cytoplasm of a cell through inositol-1,4,5 trisphosphate receptors plays a vital role in various physiological processes within the human body. Examples include the secretion of saliva in salivary glands and insulin in pancreatic beta-cells, the contraction of heart muscles and the firing of neurons. Calcium is essential for these functions to occur properly. A dysregulated calcium signalling system has been linked to a large variety of human diseases, such as neurological diseases, heart disease, diabetes and abnormal salivary gland function. Mathematical models of the calcium signalling system can provide interesting insights into inositol-1,4,5 trisphosphate receptor and calcium dynamics. For example, we can ask: how does mutation affect the frequency of calcium events and how does the behaviour of the inositol-1,4,5 trisphosphate receptor differ between cell types?

In this thesis, we develop a calcium puff model based on integrodifferential equations. Our model is parameterised using stationary single channel

and calcium puff data from HEK-3KO cells, obtained through collaboration with the Yule Lab, Rochester. In Chapter 2, analysis of stationary single channel and calcium puff data is conducted. We compare the results from three calcium puff data sets and parameterise three statistical distributions using interpuff interval data. The statistical distributions are evaluated qualitatively and quantitatively, concluding with the best fit. In Chapter 3, we introduce a calcium puff model based on integrodifferential equations. Our model expands current calcium puff models by enabling investigation of the *memory* of an inositol-1,4,5 trisphosphate receptor and the impact of differing lengths on calcium dynamics. In Chapter 4, we parameterise our mathematical model using experimental data from healthy and mutated inositol-1,4,5 trisphosphate receptors, initially presented in Chapter 2.

Using our mathematical model, one can directly relate the integral terms to the delayed response of the inositol-1,4,5 trisphosphate receptor, observed in patch clamp experiments. Furthermore, our novel mathematical models, parameterised with experimental data, offer a deeper insight into the prolonged effects of alterations to the inositol-1,4,5 trisphosphate receptor on the calcium signalling system. This extends our understanding beyond the time frames achievable in experimental conditions.

Publication and dissemination of results

Journal articles

- **Molly Hawker** and Ivo Siekmann. "People" meet "Markovians"—Individual-based modelling with hybrid stochastic systems. *Journal of Biological Systems*. 2023. doi:10.1142/S0218339023400028. URL https://doi.org/10.1142/S0218339023400028

Talks and Conferences

- Livin' Mathematics seminar, in-person, Liverpool, UK. Talk. March 2024. *Mathematical modelling of the calcium signalling system*

- Rise of the machines workshop, in-person, Liverpool, UK. Talk. January 2024. *Data-driven modelling of calcium puffs using integrodifferential equations*

- The Casual Conference, in-person, Liverpool, UK. Talk. December 2023. *When biology and mathematics come together*

- Data-driven mechanistic models of complex biomedical systems workshop, in-person, Birmingham, UK. Talk. December 2023. *A calcium puff model based on integrodifferential equations*

- LJMU Postgraduate Researcher Conference, in-person, Liverpool, UK. Poster presentation. May 2023. *Mathematical modelling of the calcium signalling system: a simplified hybrid stochastic system*

- European Conference of Mathematical and Theoretical Biology, in-person, Heidelberg, DE. September 2022. Poster presentation. *Data-driven modelling of Ca^{2+} puffs*

- LJMU Postgraduate Researcher Conference, in-person, Liverpool, UK. May 2022. Poster presentation. *Cracking the calcium code - data-driven modelling of Ca^{2+} puffs*

- LJMU Research Cafe, online, Liverpool, UK. April 2022. Oral presentation. *Cracking the calcium code – modelling molecular determinants of calcium signalling in health and disease.*

Contents

List of Tables

List of Figures

1 Background

1.1 Motivation

The calcium (Ca^{2+}) signalling system contributes to physiological changes in both excitable and non-excitable cells (Fearnley et al., 2011; Bootman, 2012; Brini et al., 2014; Garcia and Boehning, 2017; Han et al., 2017; Glaser et al., 2019). This includes being a signal for life and death in the heart, playing a crucial role in healthy neuronal activity, and being a driver for insulin secretion in pancreatic beta-cells and salivary secretion in salivary glands. However, the Ca^{2+} signalling system is not infallible (Tveito and Lines, 2016; Terry et al., 2020; Fan et al., 2022a,b). An abnormal Ca^{2+} signalling system has been linked to hypertrophy and congestive heart failure, neurological diseases, such as Alzheimer's and Huntington's disease, as well as inhibiting saliva secretion (Berridge, 1997; Han et al., 2017; Glaser et al., 2019; Terry et al., 2020; Fan et al., 2022a,b). Therefore, it is important to understand Ca^{2+} and ion channel dynamics further, and this can be achieved by using data-driven mathematical modelling. Bringing together experimental data and mathematical models gives the advantage of linking together parameter changes with mutations that cause physiological changes within ion channels.

1.2 Biological background

To build a mathematical model that is a good representation of a cellular process, an understanding of the underlying dynamics of the cell is required. The literature provides useful insights into understanding ion channels, specifically inositol-1,4,5 trisphosphate receptors (IP_3R), and the drivers behind the Ca^{2+} signalling processes. This section explains the key biological processes that contribute to the formation of our mathematical model.

1.2.1 Ion Channels

Ion channels are important membrane proteins encoded by over 400 genes in the human genome (Capener et al., 2002; Imbrici et al., 2016). Existing in every cellular membrane, they change their conformations allowing ions specific to the channel type to move through their pore (Keener and Sneyd, 2009; Islam, 2020). This change of ion channel state is known as a gating process and, depending on the ion channel stimulant, can be triggered by membrane potential, the binding/unbinding of ligands or other agents (Resta and Becchetti, 2012). The movement of ions through the cell can trigger different vital processes to take place within the human body. Voltage-gated ion channels play a crucial role in the electrical signalling of excitable cells, such as those involved in muscle contraction and the firing of neurons. They are triggered by changes in transmembrane voltage (Capener et al., 2002; Bezprozvanny, 2009). Ligand-gated ion channels are stimulated by an effector ligand and triggered by further changes in ligand concentration. These changes are essential for the signalling of non-excitable cells, such as the gating of fluid secretion within the salivary gland and activation of embryo

fertilization (Rückl et al., 2015; Han et al., 2017; Swann, 2023).

Scientists have been able to gain a better understanding of ion channels through experiments. In the early 1950s, Hodgkin and Huxley (1952) shared the first complete description of using electrophysiology experiments to measure the flow of electrical current through the surface of a giant nerve fibre (Hill and Stephens, 2021). Following this, Neher and Sakmann (1976) recorded the first opening and closing of an individual ion channel using the patch clamp experiment. This process involves using a glass electrode with a micro-pipette to make a seal on the surface of a cell and recording the membrane potential and/or current flowing through the channel (Neher and Sakmann, 1976; Hill and Stephens, 2021). The channel stochastically jumps between a nonzero current, showing the channel is open, and a zero current, indicating the channel is closed (Rahman and Taylor, 2009). Some ion channels, such as ryanodine-sensitive calcium channels (RyR) (Liu et al., 1989; Ding and Kasai, 1996) and voltage-gated sodium channels (Magistretti and Alonso, 2006), have been shown to express multiple levels of conductance at a fixed voltage level (Pollard et al., 1994). Pollard et al. (1994) state it is not uncommon to find at least 5 or 6 conductance levels in channel systems. By using an electrophysical technique, such as the patch clamp experiment, it is possible to study the functions and dysfunctions of cells (Hill and Stephens, 2021).

The structure of the inositol trisphosphate receptor

IP_3Rs are among the largest known ion channels. Approximately 90% of the channel is located in the cytosol while the remaining stalk embedded in intra-

cellular Ca^{2+} stores, called the endoplasmic reticulum (ER) or sarcoplasmic reticulum (SR) (Fan et al., 2015; Paknejad and Hite, 2018; Prole and Taylor, 2019). Fig 1.1 depicts the IP_3R in both the ER and SR (Rüdiger, 2013). The SR is the intracellular Ca^{2+} store in myocyte cells, while the ER is present in most eukaryotic cells (Taylor and Laude, 2002; Bootman, 2012; Baker et al., 2023). Mammals have three subtypes of IP_3R (IP_3R1, IP_3R2, IP_3R3) which have their characteristic features encoded by separate genes and differ in their sensitivity to IP_3, phosphorylation and regulation to Ca^{2+} and ATP (Ivanova et al., 2014; Kerkhofs et al., 2018; Fan et al., 2022a). IP_3R1 are highly expressed in neurons, IP_3R2 in cardiomyocytes and IP_3R3 in rapidly proliferating cells (Ivanova et al., 2014; Kerkhofs et al., 2018). Each IP_3R is formed of four subunits, which can be identical or different (Kerkhofs et al., 2018; Siekmann et al., 2019; Fan et al., 2022a).

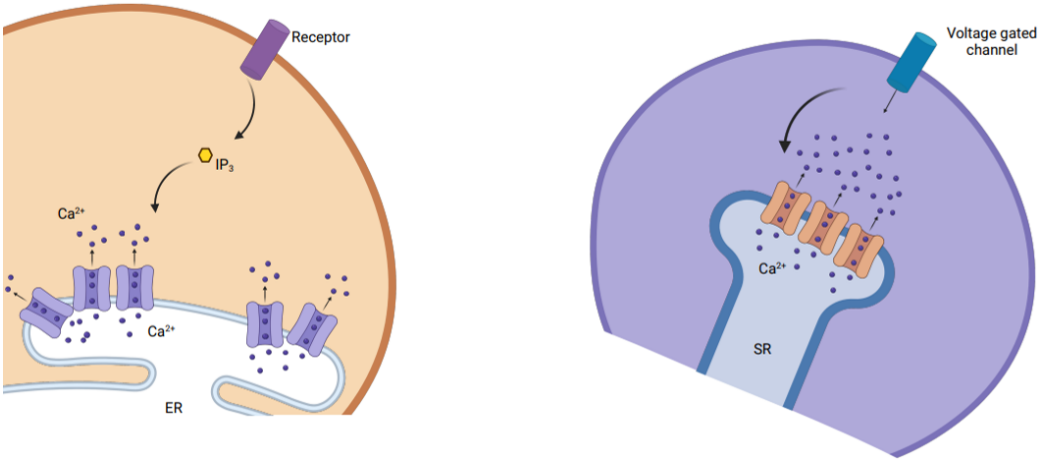

Figure 1.1: Representation of the endoplasmic reticulum (ER) and sarcoplasmic reticulum (SR) adapted from Rüdiger (2013). Created with BioRender.com

The 3-dimensional structure of the complete IP_3R and RyR channel proteins are complex, however, the use of single particle cryogenic electron mi-

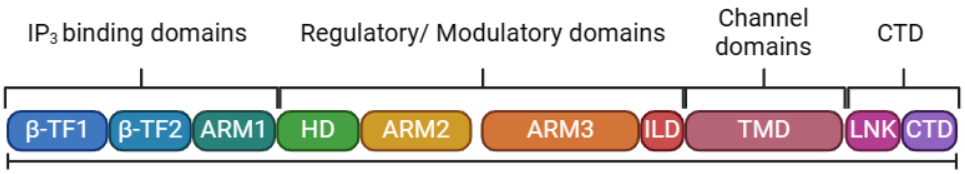

Figure 1.2: Schematic diagram of the domain structure of IP_3Rs. Adapted from Fan et al. (2022a); Baker et al. (2023)

croscopy (cryo-EM) has enabled structural characterisation of IP_3R (Fan et al., 2022a; Baker et al., 2023). A schematic diagram of the IP_3R structure is illustrated in Fig 1.2. The IP_3R consists of two β-trefoil domains (βTF1-2), three armadillo solenoid folds (ARM1-3), a helical domain (HD), an intervening lateral domain (ILD), a transmembrane domain (TMD), a linker domain (LD) and a C-terminal helical domain (CTD) (Fan et al., 2022a; Baker et al., 2023). Ca^{2+} binding sites have been found in the ligand-binding domains, which consist of βTF1-2 and ARM1, in the Ca^{2+} sensor region in ARM3 and in the luminal vestibule of the TMD (Fan et al., 2022b). A single IP_3 binding site exists at the N-terminus of each IP_3R subunit (Fan et al., 2022b).

Ca^{2+} signalling and inositol trisphosphate receptors

IP_3R are ligand-gated ion channels, activated by Ca^{2+} ions and IP_3 (Fan et al., 2022a). IP_3R can exist as a single entity or form clusters (Thurley et al., 2011; Siekmann et al., 2012; Garcia and Boehning, 2017). The binding of IP_3 to subunits of the IP_3R open the channel, releasing Ca^{2+} ions into the cytoplasm (Taylor and Laude, 2002; Thurley et al., 2012; Rückl et al., 2015; Han et al., 2017). The elevation in the Ca^{2+} concentration enhances the open probability of the IP_3R leading to a future release in Ca^{2+} ions

(Rüdiger and Shuai, 2019; Siekmann et al., 2019; Islam, 2020). Once the Ca^{2+} concentration becomes high, the open probability decreases and IP_3R is inhibited (Taylor and Laude, 2002). The release of Ca^{2+} ions from a cluster of IP_3Rs can be described in a hierarchical manner (Cao et al., 2013). When a single IP_3R opens, it causes a small increase in the cytoplasmic Ca^{2+} concentration, which is known as a Ca^{2+} blip (Parker and Yao, 1996; Swillens et al., 1999). The release of Ca^{2+} ions from a Ca^{2+} blip stimulates neighbouring IP_3-liganded IP_3Rs, increasing their open probability and releasing further Ca^{2+} ions into the cytoplasm (Parker and Yao, 1996; Swillens et al., 1999; Foskett et al., 2007; Rüdiger and Shuai, 2019; Siekmann et al., 2019; Islam, 2020). The Ca^{2+} released from a cluster of IP_3Rs is called a Ca^{2+} puff. The occurrence of Ca^{2+} puffs can trigger a wave of Ca^{2+} across the entire cell (Dickinson et al., 2012; Cao et al., 2013). Oscillatory Ca^{2+} can be observed through the fluctuations in the Ca^{2+} concentration and are controlled by Ca^{2+} fluxes (Berridge, 1990; Perc et al., 2008). A high concentration of Ca^{2+} inhibits the IP_3R channel and decreases its open probability (Foskett et al., 2007; Skupin and Falcke, 2010; Rüdiger and Shuai, 2019; Siekmann et al., 2019). Intracellular oscillations and waves are important cellular signals, and Ca^{2+} puffs are believed to play a vital role in generating Ca^{2+} waves that travel across the cell (Bootman et al., 1997; Marchant and Parker, 2001; Rückl et al., 2015; Cao et al., 2017). Fig 1.3 presents a visual representation of Ca^{2+} blips, puffs and waves.

Wagner and Yule (2012) used nuclear patch-clamp experiments to measure the activity of single IP_3R channels in DT40-3KO cells. They found that the channel exhibited two distinct levels of activity, demonstrated by an av-

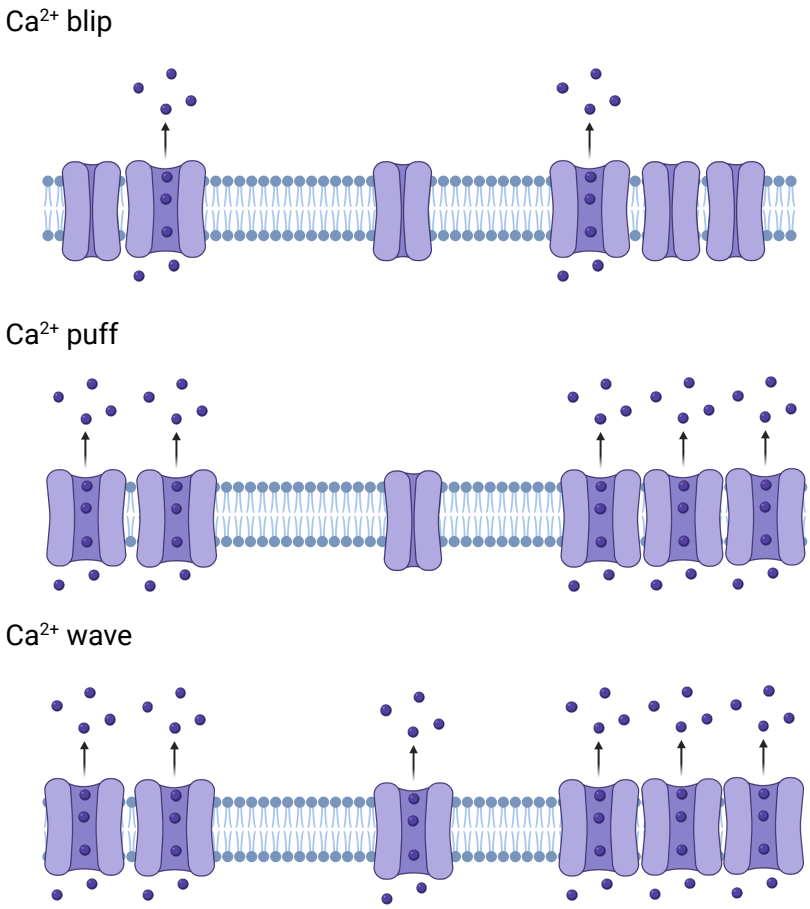

Figure 1.3: Representation of a Ca^{2+} blip, puff and wave adapted from Rüdiger (2013). Created with BioRender.com

erage open probability close to zero for low activity and an open probability for approximately 0.7 for high activity (Siekmann et al., 2014).

Ca^{2+} puffs are depicted by a large spike in the Ca^{2+} concentration followed by a slower decay (Marchant and Taylor, 1998). This quick release of Ca^{2+} is caused by ligands binding to the IP_3R and rapidly changing its confirmation (Marchant and Taylor, 1998; Thrower et al., 2000; Foskett et al., 2007). To understand this dynamic within a single IP_3R , Mak et al. (2007) used nuclear patch-clamp techniques and investigated the response of individual IP_3R channels to rapid fluctuations in ligand concentration. This method contrasts more common patch-clamp experiments in which the ligand concentration is kept constant. By switching between high and low ligand concentrations, Mak et al. (2007) examined the kinetics of channel activation and deactivation. Their study revealed IP_3Rs exhibit a delay (latency) before responding to changes in ligand concentration with the longest mean latency being for IP_3R recovery from Ca^{2+} inhibition. This latency has been shown to be responsible for the refractory behaviour of Ca^{2+} release sites, *in vivo* (Ilyin and Parker, 1994; Mak et al., 2007). Following a Ca^{2+} puff, the IP_3R cannot respond to ligand stimulation for several seconds (Ilyin and Parker, 1994).

1.2.2 Calcium dysregulation and the effect on the human body

The Ca^{2+} signalling system plays a crucial role in various processes within the human body. When this complex system gets dysregulated in some way, it can negatively affect a person's health. Several human diseases have been

associated with an abnormal Ca^{2+} signalling system, including Alzheimer's Disease, Huntington's Disease, cancers, heart failure, diabetes, and changes to neurodevelopment (Etcheberrigaray et al., 1998; Berridge, 2003; Pchitskaya et al., 2018; Tong et al., 2018; Islam, 2020; Grady and Morgan, 2021; Klocke et al., 2023). This section focuses on studies that have linked human diseases with abnormal Ca^{2+} signalling systems.

Alzheimer's and Huntington's Disease

Precise control of the Ca^{2+} signalling system within specific compartments is crucial for healthy neuronal function (Pchitskaya et al., 2018; Calvo-Rodriguez and Bacskai, 2021), including energy production, survival, learning, memory, and cell death (Calvo-Rodriguez and Bacskai, 2021). Change to Ca^{2+} signals has the potential to have harmful effects (Pchitskaya et al., 2018). Dysregulation of the Ca^{2+} signalling system has been linked to various neurodegenerative diseases, such as Alzheimer's Disease (AD) and Huntington's Disease (HD) (Khachaturian, 1987; Bezprozvanny, 2009).

In the early 1980s, a hypothesis was proposed linking Ca^{2+} and the ageing process (Khachaturian, 1987). The theory suggested that changes in the regulation of cytosol Ca^{2+} concentrations could account for age-related neuronal changes (Khachaturian, 1987). Although this idea was initially considered speculative (Khachaturian, 1987), there have since been further studies that support the hypothesis and link Ca^{2+} signalling and AD (Bezprozvanny, 2009). Studies on the neurons of young and old rodents suggest that the Ca^{2+} signalling mechanisms undergo age-dependent changes (Bezprozvanny, 2009). A wide range of literature supports the hypothesis that Ca^{2+} home-

ostasis dysregulation is the cause of AD (Khachaturian, 1989; Bezprozvanny and Mattson, 2008; Briggs et al., 2017; Pchitskaya et al., 2018; Glaser et al., 2019). These studies show Ca^{2+} levels in the ER are high in AD and ageing neurons (Glaser et al., 2019). A review by Tong et al. (2018) suggests Ca^{2+} dysregulation, due to presenilin mutation, occurs before the formation of extracellular beta-amyloid (Aβ) plaques and neurofibrillary tangles in AD brains. The accumulation of Aβ plaques and neurofibrillary tangles are hallmarks associated with AD (Tiraboschi et al., 2004; Tong et al., 2018).

Familial AD is a form of AD caused by a gene mutation that typically emerges in individuals aged between 35-65 years who have a family history of AD (Wu et al., 2012; Cauwenberghe et al., 2016; Mehra and Kepp, 2021). In a clinical study conducted by Etcheberrigaray et al. (1998), it was found that a large proportion of individuals who have a relative with AD showed alterations in IP_3-mediated Ca^{2+} responses before exhibiting symptoms themselves. Bezprozvanny (2009) state Familial AD mutants in presenilins result in abnormal Ca^{2+} signalling.

HD is a genetic disorder, caused by a single mutation, that affects mood, cognition and movement (Bezprozvanny, 2009; Raymond, 2017). Dysregulation of the Ca^{2+} signalling system has been suggested to play an important role in HD (Raymond, 2017). Mutant Huntington proteins (mHtt) can bind to proteins and disbalance signalling pathways, such as IP_3R (Glaser et al., 2019). This causes IP_3R to have an increased affinity for IP_3 and enhances Ca^{2+} levels during the response to metabotropic glutamate receptor 1 and 5 receptors, a receptor type that activates many signalling pathways (Ribeiro, 2010; Glaser et al., 2019). Furthermore, Glaser et al. (2019) state that mHtt

has been linked to causing an increase of Ca^{2+} through RyR activation. Experimental results from mouse models have shown enhanced IP_3R activity in HD (Bezprozvanny, 2009; Glaser et al., 2019).

Cancer

Ca^{2+} signalling is not limited to healthy cells but is also present in tumour cells (Panda et al., 2022). In cancer cells, the Ca^{2+} signalling pathway can become overactive, inhibited, or adjusted to support the survival of the cell (Pratt et al., 2020). The remodelling of Ca^{2+} signalling has been suggested to contribute to cancer cell immortality, cell apoptosis resistance and reduced Ca^{2+} mediated cell death (Bruce and James, 2020). Breast cancer and prostate cancer are examples of cancers that have been linked to Ca^{2+} (Pratt et al., 2020; Bruce and James, 2020; Grady and Morgan, 2021; Panda et al., 2022). Defective Ca^{2+} channels, alterations in Ca^{2+} transport and signalling lead to tumour initiation, metastasis and progression (Grady and Morgan, 2021; Daba et al., 2023).

While there is evidence that Ca^{2+} channels are altered in different types of cancer, Bruce and James (2020) note it is difficult to determine if the change in signalling is a cause or consequence of cancer. Studies have suggested that targeting the Ca^{2+} channels in cancer cells could be used as a therapy for cancer (Bruce and James, 2020; Panda et al., 2022; Kang et al., 2023). Often these treatments are not enough to be used as a complete treatment for cancer and additional therapies are required, for example chemotherapy (Kang et al., 2023). Whilst the idea of targeting the Ca^{2+} signalling system to treat cancer is hopeful, due to Ca^{2+} channels existing in non-cancerous and cancerous

cells, treatments could have a negative impact on the healthy cells (Bruce and James, 2020; Panda et al., 2022). Therefore, it is important that specific Ca^{2+} channels that are only expressed in cancer cells are identified (Panda et al., 2022). For example, the regulation of Orai1, a plasma membrane channel, by the Secretory Pathway Ca^{2+}ATPase (SPCA2) is unique to breast cancer cells (Feng et al., 2010; Panda et al., 2022).

Cardiac disease

Ca^{2+} ions play an important role in the functioning of the heart. They regulate pacemaker activity, ventricular cell contraction and cardiac remodelling (Berridge, 2003; Garcia and Boehning, 2017). Cardiac remodelling is the phenotypic change that occurs during cardiac hypertrophy and congestive heart failure, in which persistent stress causes the heart to grow and leads to an irreversible state. Signalling pathways, including Ca^{2+} signalling, control this cardiac remodelling (Berridge, 2003). The increased expression and function of IP_3R during cardiac hypertrophy is thought to be the cause of this remodelling (Garcia and Boehning, 2017). Moreover, the increased expression of IP_3R has also been linked to dilated cardiomyopathy (Garcia and Boehning, 2017).

Salivary glands

According to Teos et al. (2015), the release of intracellular Ca^{2+} through IP_3R in acinar cells is the most crucial step in regulating fluid secretion by neurotransmitters. Without Ca^{2+} , saliva secretion becomes inhibited (Douglas and Rubin, 1961; Han et al., 2017), which can lead to oral health issues

and affect other body tissues such as the skin, heart and gastrointestinal system (Teos et al., 2015; Ambudkar, 2018).

Sjögren's Syndrome, a chronic autoimmune disease, and radiation treatment for head and neck cancers can cause irreversible damage to salivary glands (Teos et al., 2015; Han et al., 2017; Ambudkar, 2018). In a study conducted by Teos et al. (2015), a comparison was made between the acinar cell function of healthy volunteers and individuals with Sjögren's Syndrome. The results showed significant differences in Ca^{2+} signalling between the two groups. Sjögren's Syndrome patients' acini exhibited a decrease in IP_3R and a reduction in carbachol-stimulated intracellular Ca^{2+} release, in contrast to healthy volunteers.

Whilst radiotherapy is the main treatment for head and neck cancers, it can cause significant acute and long-term side effects on other tissues (Ambudkar, 2018). A study by Leslie and Dische (1991) investigated the effect radiotherapy had on patients in remission who were treated for a malignancy confined to one side of their head nine months after treatment. Using the side of the head without malignancy as a control, Leslie and Dische (1991) compared the saliva produced by the parotid glands. Their results demonstrated that parotid glands that had been impacted by the radiotherapy had a significant fall in saliva pH and flow. Results by Ambudkar (2018) show the impact of radiotherapy on salivary glands is caused by a reduction in STIM1 (an ER-Ca^{2+} binding protein) and store-operated Ca^{2+} entry. Furthermore, rodent models demonstrate the Ca^{2+} signalling system is immediately dysregulated in response to radiation with elevated intracellular Ca^{2+} levels being reported (Jasmer et al., 2020).

Mutations of the inositol trisphosphate receptor in experimental studies

Studies have shown the Ca^{2+} signalling system plays a crucial role in the human body, and its dysregulation can have adverse effects. Mutations have been identified in all four functional domains of the IP_3R, which can interfere with various aspects of its biology, including IP_3 binding, ion permeation, and stability (Terry et al., 2020). Various experimental studies have been conducted to investigate the impact of different mutations on the IP_3R.

In their study, Terry et al. (2020) investigated three different mutations in three specific domains of the IP_3R to determine their effect on channel activity. They found that all three mutations lead to a decrease in channel activity. The Arg-269 (R269) residue is important for binding in the IP_3R. Terry et al. (2020) substituted this residue with a point mutation (R269W) which is known to cause spinocerebellar ataxia in patients. They then examined the effect it had on IP_3 binding in the chicken lymphocyte cell line, DT40-3KO cells. Results showed cells with the R269W mutation resulted in reduced IP_3-binding activity and did not release measurable Ca^{2+} signals when stimulated by trypsin.

The second residue that was mutated was Asn-602 (N602) which introduced a negatively charged residue (N602D). The N602D mutation is associated with a diagnosis of ataxic cerebral palsy without cerebral atrophy. This mutation did not alter IP_3 binding in DT40-3KO cells and stimulation of trypsin did not produce measurable Ca^{2+} release.

Finally, Terry et al. (2020) investigated the G2498S mutation in IP_3R2, which they stated is expected to disrupt the channel pore. This mutation

has been linked with hypohidrosis. Similar to the N602D mutation, the G24985 mutation did not alter IP_3 binding; however, it resulted in the absence of Ca^{2+} release. When all the mutations were applied in human embryonic kidney-3KO (HEK-3KO) cells, activity was higher for the R269W and N602D mutations in comparison to the DT40-3KO cells. However, the G24985 mutation did not support Ca^{2+} release.

In a study by Arige et al. (2022), the 2002 glutamic acid residue was substituted with aspartic acid (E2002D), alanine (E2002A) or glutanine (E2002Q) in HEK-3KO cells to investigate the effect changes to the side chain charge has on the IP_3R activity. The results showed that Ca^{2+} signals were significantly reduced in cells with the aspartic acid mutation and not detected in those with alanine and glutamine mutations. Arige et al. (2022) concluded that the negative charge of glutamic acid side chain residue is important for IP_3R activity. Although the structure of the IP_3R did not change significantly from the mutations, analysis of single channel activity showed significant differences in the open probabilities of mutated IP_3R compared to wild-type IP_3R. For example, the maximum open probability of E2002D-type 1 IPR was 45% compared to a maximum open probability of 70% of the wild-type 1 IPR.

Tambeaux et al. (2023) replaced the D2594 residue in HEK-293 cell lines with lysine (D2594K) and alanine (D2594A). These substitutions resulted in enhanced IP_3 ligand sensitivity and a reduction of IP_3R function. The D2594K mutation, which involves replacing a negatively charged residue with a positively charged one at the channel's pore cytosolic exit, affected the gating behaviour of the ion channel. When investigating the effect on mutant

mice, male mice showed pathological changes, such as loss of fertility.

1.3 Modelling background

Mathematical models of the Ca^{2+} signalling system are often complex, requiring both the stochastic behaviour of the IP_3R and the deterministic behaviour of the Ca^{2+} puffs to be accounted for. Markov models are commonly used to simulate the random openings and closings of the IP_3R whilst ordinary differential equations (ODEs) are used to describe the release of Ca^{2+} into the cytoplasm. Due to our research focusing on the change in Ca^{2+} concentration over time, an ODE model is appropriate. However, if spatial dynamics were also being taken into consideration, partial differential equations would be more suitable. In this section, we describe the process of building a model of the Ca^{2+} signalling system.

1.3.1 Markov processes

Markov models are often written as a chemical reaction scheme, with a set of states, depicted by $S_n = S_1, \ldots, S_n$ in Figure 1.4, connected by non-negative transition rates (Siekmann et al., 2011; Tveito and Lines, 2016). The transition rates give the probability of changing state in a small-time interval, Δt, and can be constant or depend on voltages or concentrations (Tveito and Lines, 2016). The model's state determines the state transitions independent of past events.

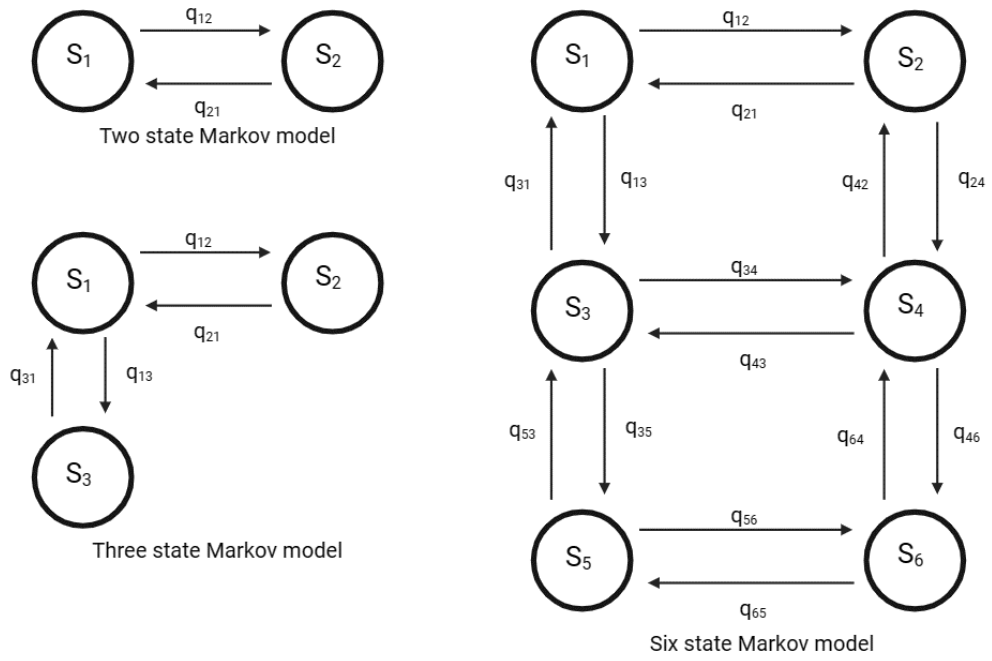

Figure 1.4: Example of Markov models. S_n represents the state of model and transition rates are shown by the parameters q

Modelling ion channels using Markov models

Siekmann et al. (2012) describe the aggregated continuous-time Markov model to be the most natural method for modelling the stochastic behaviour of a single ion channel. The states of the Markov model represent the open (O) and closed (C) states of the channel and the rates q_{co} and q_{oc} describe how quickly the channel opens or closes, respectively. If the channel is currently in the closed state, the probability of the channel going to an open state is $q_{co}\ \Delta t$. Similarly, the probability of going from an open to a closed state is given by $q_{oc}\Delta t$ (Tveito and Lines, 2016).

Mathematically, these probabilities can be written as:

$$q_{oc}\Delta t = P\left[S(t+\Delta t) = C | S(t) = O\right] \tag{1.1}$$

$$q_{co}\Delta t = P\left[S(t+\Delta t) = O | S(t) = C\right] \tag{1.2}$$

Using Markov models, the open and closed probability of the ion channel at time $t + \Delta t$ can be calculated, if the state at the current time, t, is known (Siekmann et al., 2016; Tveito and Lines, 2016). Within this thesis, we refer to the open probability as P_o and the closed probability as P_c. We assume that only one transition takes place within the time frame $[t, t + \Delta t]$. The probability of the channel being open at time $t + \Delta t$ is equal to the probability of the channel being open at time t, $P(S(t) = O)$ and not closing within the time frame Δt, $P(\text{not } (O \rightarrow C \text{ during } \Delta t))$ plus the probability of the channel being closed at time t, $P(S(t) = C)$ and being in the open state at time $t + \Delta t$, $P(C \rightarrow O \text{ during } \Delta t)$. Similarly, the probability of the channel being closed at time $t + \Delta t$ is equal to the probability of the

channel being closed at time t, $P(S(t) = C)$ and not opening within the time frame Δt, $P(\text{not}(C \rightarrow O \text{ during } \Delta t)$ plus the probability of the channel being open at time t, $P(S(t) = O)$ and being in the closed state at time $t + \Delta t$, $P(O \rightarrow C \text{ during } \Delta t)$.

The probabilities of the channel being in the open or closed state at time $t + \Delta t$ can be written as:

$$\begin{aligned} P_o(t + \Delta t) = P[S(t) = C \text{ and } (C \rightarrow O \text{ during } \Delta t)] \\ + P[S(t) = O \text{ and not } (O \rightarrow C \text{ during } \Delta t)] \end{aligned} \tag{1.3}$$

$$\begin{aligned} P_c(t + \Delta t) = P[S(t) = O \text{ and } (O \rightarrow C \text{ during } \Delta t)] \\ + P[S(t) = O \text{ and not } (C \rightarrow O \text{ during } \Delta t)] \end{aligned} \tag{1.4}$$

Furthermore, Eq 1.3-1.4 can be written as:

$$\begin{aligned} P_o(t + \Delta t) = P_c(t) \cdot P(S(t + \Delta t) = O | S(t) = C) \\ + P_o(t) \cdot P(S(t + \Delta t) = O | S(t) = O) \end{aligned} \tag{1.5}$$

$$\begin{aligned} P_c(t + \Delta t) = P_o(t) \cdot P(S(t + \Delta t) = C | S(t) = O) \\ + P_c(t) \cdot P(S(t + \Delta t) = C | S(t) = C) \end{aligned} \tag{1.6}$$

By introducing Eq 1.1-1.2 we get:

$$P_o(t + \Delta t) = P_c(t) q_{co} \Delta t + P_o(t)(1 - q_{oc} \Delta t) \tag{1.7}$$

$$P_c(t + \Delta t) = P_o(t) q_{oc} \Delta t + P_c(t)(1 - q_{co} \Delta t) \tag{1.8}$$

Expanding the right-hand-side, gathering like terms and dividing through

by Δt gives:

$$\frac{P_o(t+\Delta t) - P_o(t)}{\Delta t} = P_c(t)q_{co} - P_o(t)q_{oc} \tag{1.9}$$

$$\frac{P_c(t+\Delta t) - P_c(t)}{\Delta t} = P_o(t)q_{oc} - P_c(t)q_{co} \tag{1.10}$$

By introducing the limit $\Delta t \to 0$, thus considering Δt to be so small that only one transition takes place within the time frame $[t, t+\Delta t]$, we can calculate the derivative of $P_o(t)$ and $P_c(t)$(Tveito and Lines, 2016).

$$\frac{dP_o(t)}{dt} = P_c(t)q_{co} - P_o(t)q_{oc} \tag{1.11}$$

$$\frac{dP_c(t)}{dt} = P_o(t)q_{oc} - P_c(t)q_{co} \tag{1.12}$$

Here, we have shown the development of a two-state Markov model. Using the same process Markov models of any number of states can be created. The time-dependent probability distribution $p(t)$ would thus require a vector of probabilities and a matrix of transition rates, Q, known as the infinitesimal generator (Colquhoun and Hawkes, 1981; Siekmann et al., 2019). The general equation is shown in Eq 1.13. The Siekmann model (Siekmann et al., 2012) and Ullah model (Ullah et al., 2012a), shown in Fig 1.5, are examples of IP_3R Markov models with more states.

$$\frac{dp(t)}{dt} = p(t)Q, \quad p(0) = p_0 \tag{1.13}$$

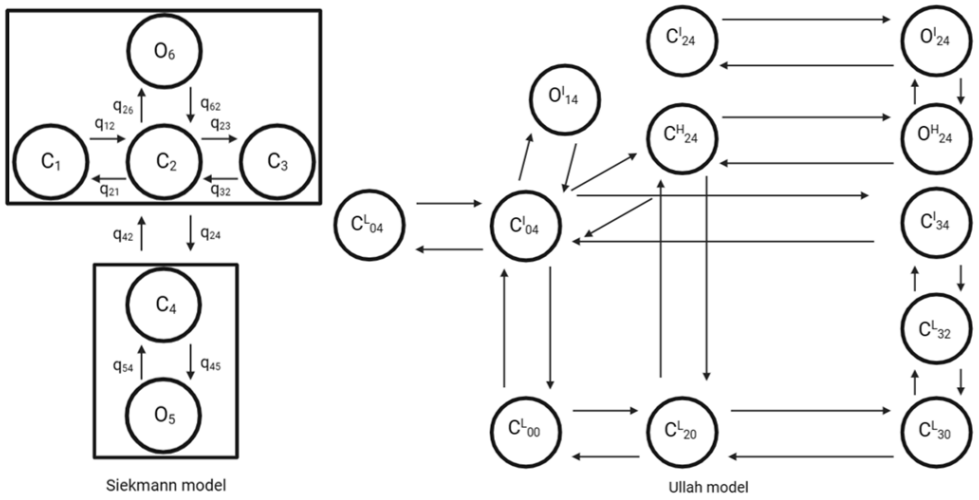

Figure 1.5: Siekmann model (Siekmann et al., 2012) and Ullah model (Ullah et al., 2012a)

1.3.2 Modelling of calcium dynamics

Mathematical models of the IP_3R help to understand Ca^{2+} dynamics (Colquhoun and Hawkes, 1981; Keizer and Young, 1994; Li and Rinzel, 1994; Swillens et al., 1994; Sneyd et al., 2004; Siekmann et al., 2012; Ullah et al., 2012a; Cao et al., 2013; Rüdiger, 2013; Cao et al., 2014; Dupont et al., 2016; Dupont and Sneyd, 2017; Han et al., 2017; Siekmann et al., 2019). Model development has improved greatly since Colquhoun and Hawkes (1977) first used a Markov model to describe the stochastic behaviour of single ion channels. Over the past decade, it has become evident that incorporating data into models, whilst challenging, leads to more accurate simulations (Siekmann et al., 2019).

Siekmann et al. (2019) claim the main challenge of modelling data-driven ion channels is defining a structure of Markov models that allows the inte-

gration of various sources of experimental data. Two models that account for all sources of data currently available are the Siekmann model and the Ullah model, presented in Fig 1.5 (Mak et al., 2007; Wagner and Yule, 2012; Siekmann et al., 2012; Ullah et al., 2012a; Cao et al., 2013; Siekmann et al., 2019).

Siekmann Model

A continuous–time Markov model by Siekmann et al. (2012) was created to accurately represent the kinetics of type I and II IP_3R depending on concentrations of IP_3, ATP and intracellular Ca^{2+}. The model was fitted directly to time-series data from a study conducted by Wagner and Yule (2012). The Siekmann model takes into consideration extended periods of inactivity alternating with intervals of bursting activity, known as mode changes. Transition rates connected aggregated states representing high and low IP_3R activity.

Alongside the stationary single channel data by Wagner and Yule (2012), Cao et al. (2013) incorporated non-stationary single channel data by Mak et al. (2007) into the Siekmann model. This was achieved by introducing four gating variables into the model that are similar to the Hodgkin-Huxley equations. The gating variables were qualitatively fit to the Mak et al. (2007) latency data. By using both stationary and non-stationary data, Cao et al. (2013) succeeded in creating a model that can simultaneously reproduce the correct IP_3R and Ca^{2+} puff statistics (Mak et al., 2007; Siekmann et al., 2012; Wagner and Yule, 2012; Cao et al., 2013). Further developments of the model have since been made, such as creating a two-state model by using quasi-steady-state approximation and ignoring low dwell times, simulating

the dynamics in HSY cells and understanding the dependencies of certain parameters on the interpuff interval (the waiting time between subsequent puffs) (Cao et al., 2014; Han et al., 2017; Cao et al., 2017).

Cao et al. (2014) demonstrate the six-state Cao et al. model (Siekmann et al., 2012; Cao et al., 2013) can be reduced to a two-state model by using quasi-steady-state approximation and ignoring low dwell times. Quantitatively similar Ca^{2+} puff statistics are produced by the simplified model, demonstrating that the intramodal structure is not key in producing the desired IP_3R and Ca^{2+} dynamics. Cao et al. (2014) also investigated if Ca^{2+} oscillations, which are caused by the stochastic behaviour of IP_3R , can be modelled deterministically. They converted their simplified two-state model into a deterministic model that consists of a system of four ODEs. The stochastic and deterministic models were used to simulate Ca^{2+} oscillations in airway smooth muscle cells. Their results show that a deterministic model can produce the same process of spike termination as a stochastic model.

Sneyd et al. (2017) used the methods by Siekmann et al. (2012); Cao et al. (2013, 2014) to construct a simplified three-state Markov model from the original six-state Siekmann model to simulate Ca^{2+} oscillations. Like Cao et al. (2014), Sneyd et al. (2017) treated the Ca^{2+} oscillations as deterministic. The model consists of two closed states and one open state and predicts the rate at which IP_3R activation responds to changes in Ca^{2+}, which is a crucial parameter for controlling periods of oscillations. The rates between the closed and open states are constant, whereas the rates between the closed states are Ca^{2+} and IP_3 dependent and were fit using data from DT40-3KO and airway smooth muscle cells.

Ullah Model

Ullah et al. (2012a) used a continuous-time Markov-chain model with nine closed states and three open states to simulate IP_3R. The model states are distinguished by how many particles of each ligand are bound to the channel. For example, $O_{13}{}^{I}$ denotes an open state that is in the intermediate mode with one Ca^{2+} and three IP_3 bound. Ullah et al. (2012a) incorporate the same steady-state, modal gating and latency data as Cao et al. (2013) into their model (Mak et al., 2007; Wagner and Yule, 2012). Their model gives concrete predictions regarding the single-channel response to rapid changes in the cytosolic ligand concentration of Ca^{2+} and IP_3.

Modelling calcium fluxes within the endoplasmic reticulum

Within this thesis, we focus on the regulation of Ca^{2+} ions by IP_3R. A schematic diagram of Ca^{2+} fluxes in a non-excitable cell is presented in Fig 1.6 (Siekmann et al., 2019; Rüdiger and Shuai, 2019). The binding of IP_3 to an activating site of an IP_3R opens the channel, releasing Ca^{2+} ions from the ER into the cytoplasm, described by the flux J_{IPR}. The increase in cytoplasmic Ca^{2+} enhances the probability of IP_3R opening, resulting in further Ca^{2+} release. This process is known as calcium-induced calcium release (CICR). As the concentration of calcium ions inside the cell increases, the IP_3 receptor is inhibited, and calcium ions are transported back into the endoplasmic reticulum via the SERCA pump, J_{SERCA}. Channels regulate the influx (J_{in}) and efflux (J_{pm}) of Ca^{2+} to and from the extracellular space (Han et al., 2017; Siekmann et al., 2019; Rüdiger and Shuai, 2019).

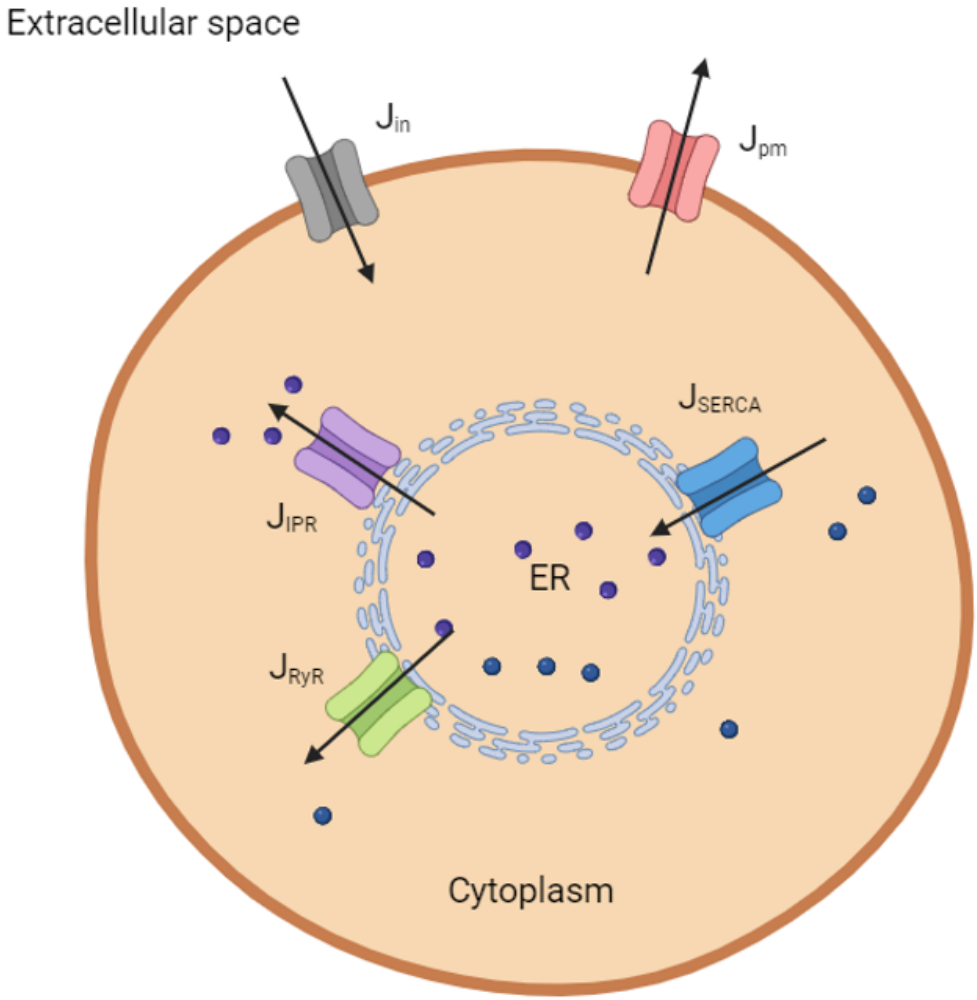

Figure 1.6: Schematic diagram of Ca^{2+} fluxes in a non-excitable cell adapted from Siekmann et al. (2019); Rüdiger and Shuai (2019). Created using BioRender.com
.

Calcium puff statistics

Stochastic Ca^{2+} traces, gathered from experimental data or mathematical simulations, are often analysed by taking into consideration three key statistics: the interpuff interval (IPI), the puff amplitude and the puff duration. IPIs are defined as being the time between the peak amplitude of Ca^{2+} puffs. We determine the start of a Ca^{2+} puff as being when the Ca^{2+} concentration is 20% of the peak amplitude. Similarly, the end of the puff is calculated as the time after the peak where the Ca^{2+} concentration is 20% of the peak amplitude. This allows us to compare our results directly to the experimental data which details the time for a Ca^{2+} puff to rise and fall to 20%, 50% and 100% of the peak amplitude (Ellefsen et al., 2014, 2019). See Chapter 2, Section 2.2 for further details. The difference in the end and start times determines the duration of the Ca^{2+} puff. An example of these metrics is shown in Fig 1.7. By presenting these statistics as probability distributions we can understand the underlying Ca^{2+} dynamics further.

1.4 Thesis overview and contributions

The work in this thesis details the beginning-to-end result of mathematically modelling the Ca^{2+} signalling system. The thesis begins by providing an in-depth statistical analysis of stationary single channel and Ca^{2+} puff data from different IP_3R . Next, we develop a novel mathematical framework for simulating Ca^{2+} puffs using a hybrid stochastic system with integrodifferential equations. Finally, this thesis ends with two new parameterised hybrid stochastic systems.

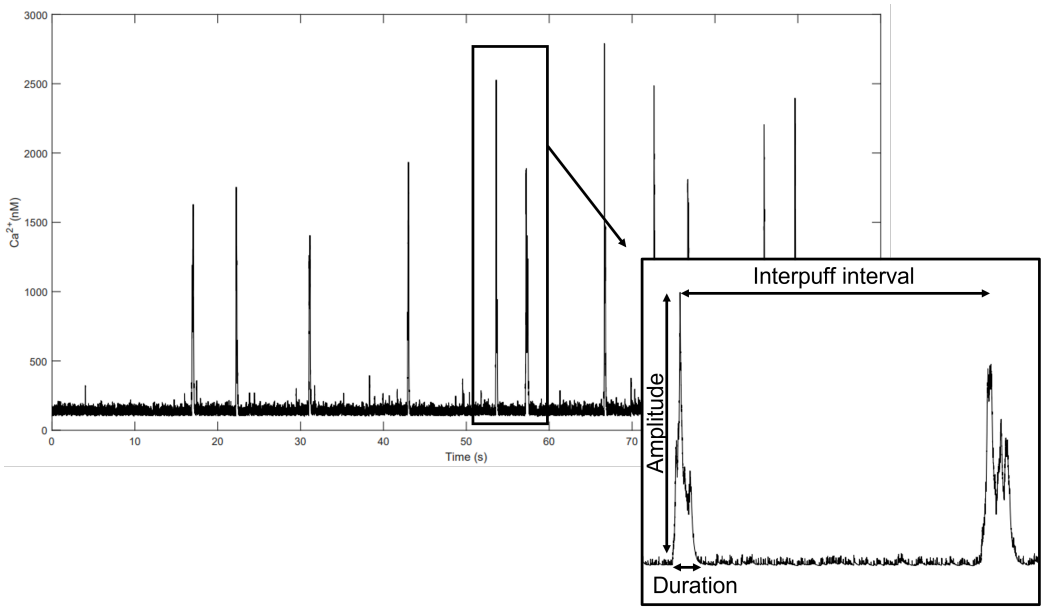

Figure 1.7: Example of Ca^{2+} trace and puff statistics gathered from trace.

In Chapter 2 we analyse the experimental data used throughout this thesis. The thesis uses experimental data from two IP_3R data sets. The first consists of unpublished Ca^{2+} puff data from exo 76 wild-type 1 IPR obtained through collaboration with the Yule Lab, Rochester. The second includes single-channel patch-clamp and Ca^{2+} puff data from wild-type 1 IPR and wild-type 1 IPR that has been substituted with aspartic acid at the 2002 glutamic acid residue (E2002D-type 1 IPR) (Arige et al., 2022). Data sets from all three IP_3R are analysed to provide insight into IPI, Ca^{2+} puff amplitude and Ca^{2+} puff durations. Using the IPI data, we parameterise three statistical distributions and compare the results qualitatively and quantitatively.

Our next step following the analysis of the experimental data is to build our hybrid stochastic system which is detailed in Chapter 3. We base our hybrid stochastic system on an existing model; this allows us to compare our

new model with the Cao et al., model (Siekmann et al., 2012; Cao et al., 2013). The benefit of our model using integrodifferential equations is that it allows us to directly relate the latency in the IP_3R responding to step changes in ligand concentrations, as demonstrated by Mak et al. (2007). This gives us the advantage of analysing how different length delays affect the Ca^{2+} dynamics.

Finally, in Chapter 4, we parameterise our mathematical model using the experimental data from wild-type 1 IPR and E2002D-type 1 IPR. We compare the summary statistics and distributions of Ca^{2+} puffs in our simulated model results to the experimental data.

In this thesis, we contribute the following:

- **Analyse stationary single channel and Ca^{2+} puff data** We analyse single-channel patch-clamp data from wild-type 1 IPR and E2002D-type 1 IPR (Arige et al., 2022). Ca^{2+} puff data from exo 76 wild-type 1 IPR, wild-type 1 IPR and E2002D-type 1 IPR is analysed and key statistical metrics are gathered (interpuff interval, Ca^{2+} puff amplitude and Ca^{2+} puff duration). We parameterise three statistical distributions using the IPIdata. Information criteria are calculated and conclude which statistical distribution best models the IPI distributions. Our analysis demonstrates that with the given experimental data, a refractory period may be present within the different IP_3R . Mathematical modelling of the Ca^{2+} signalling system using the experimental data can help to uncover this hypothesis further. See Chapter 2.

- **Derive a hybrid stochastic system based on integrodifferential equations to simulate Ca^{2+} puffs** We build a hybrid stochastic sys-

tem that uses integrodifferential equations to account for the delayed response in the IP_3R opening following a step change in Ca^{2+} concentration. We demonstrate our model is mathematically equivalent to hybrid stochastic equations in the literature, however, ours has the advantage of being able to directly relate gating variable behaviour to IP_3R dynamics. See Chapter 3

- **Derive two hybrid stochastic systems that can account for a wild type and mutated IP_3R** Using our hybrid stochastic system, we parameterise our model to be able to simulate Ca^{2+} puffs that have the same properties as the experimental data. We relate the mathematical differences within our two models to the biological mutation of the IP_3R. See Chapter 4.

2 Analysis of stationary single channel and Ca^{2+} puff data

2.1 Background

Dynamics of the Ca^{2+} signalling system can be understood in more depth through analysing Ca^{2+} puff statistics. Interpuff intervals (IPIs), Ca^{2+} puff amplitude and Ca^{2+} puff duration are commonly presented using histograms, which can provide insight into the IP_3R behaviour. For example, an Exponential IPI distribution suggests a fast recovery from Ca^{2+} inhibition (Siekmann et al., 2019). Amplitude distributions can estimate the number of IP_3R in a cluster or the number of IP_3R open during a Ca^{2+} puff (Dickinson et al., 2012; Dobramysl et al., 2016). Statistical distributions, parameterised using the Ca^{2+} puff data, are used to firstly understand the distribution of the data and secondly for ease of comparison between data sets. Within this chapter, we conduct a comprehensive literature review of statistical distributions used to describe IPI, Ca^{2+} puff amplitude and Ca^{2+} puff duration distributions. We analyse Ca^{2+} puff statistics from three different IP_3R data sets and, using the IPI data, parameterise the three commonly used statistical distributions for describing IPI distributions. We conclude which statistical distribution approximates the IPI data best by comparing their fit, calculating informa-

tion criteria and conducting the Kolmogorov-Smirnov goodness of fit test. We discuss which model scores the best AIC, BIC and WAIC values and the test statistics for each IPI distribution.

Statistical distributions parameterise Ca^{2+} puff statistics

Interpuff interval distribution

IPIs are defined as the time between successive Ca^{2+} puffs (Cao et al., 2017). The stochastic behaviour of IP_3R means IPI distributions can differ across cell and puff sites (Thurley et al., 2011). Therefore, one statistical distribution may be suitable for one data set, but be extremely unreasonable for another.

In 1995, Yao et al. (1995) analysed Ca^{2+} puffs in Xenopus laevis oocytes. They proposed that IPIs are defined by two factors. Firstly, in the initial few seconds following a puff the site may be refractory, therefore the probability of observing a second puff increases up to $\sim$ 9s. Secondly, the probability of observing a second puff decreases exponentially as the time following a puff increases. Yao et al. (1995) fit an Exponential distribution to IPIs longer than 10s. IPIs smaller than 8s declined progressively. Although an Exponential distribution fits well to longer IPIs, by choosing to use this distribution, Yao et al. (1995) are not able to accurately represent the shorter IPIs shown within their data.

Using the same data as Yao et al. (1995), Fraiman et al. (2006) analysed the sequences of Ca^{2+} puffs from Xenopus laevis oocytes. Fraiman et al. (2006) describe the IPI distribution as resembling a log-normal or Gamma

distribution. By considering non-Exponential distributions, Fraiman et al. (2006) account for the entire IPI distribution.

Thurley et al. (2011) demonstrate that there is variability in IPI distributions from SH-SY5Y and HEK 293 cells. Alongside the commonly used Exponential distribution, Thurley et al. (2011) introduce a new distribution, known as the Time-Dependent distribution, that accounts for the period of recovery following a Ca^{2+} puff. This occurrence, known as the refractory period, is characterised by the rebound from global negative feedback that occurs during the puff (Thurley and Falcke, 2011). The Time-Dependent distribution is an adapted version of the Exponential distribution and includes an additional parameter (ξ) to represent the recovery from Ca^{2+} inhibition. This Time-Dependent distribution is as follows:

$$P_t = \lambda \left(1 - e^{-\xi t}\right) e^{\left[-\lambda t + \lambda\left(1-e^{-\xi t}\right)/\xi\right]} \tag{2.1}$$

Thurley et al. (2011) fit both the Exponential and Time-Dependent distributions to different puff sites of the same cell type, emphasising the variability of IPIs. Puff sites that recover quickly from inhibition fit well to the Exponential distribution. In contrast, those that took longer to recover, i.e. the distribution has an ascending slope, fit best to the Time-Dependent distribution. If $\xi >> \lambda$ Eq 2.1 is reduced to the Exponential distribution. Using Ca^{2+} puffs simulated using their mathematical model, Cao et al. (2013) parameterised the Time-Dependent distribution and demonstrated that changes to the gating of the IP_3R affects the IPI distribution. A spatial multi-scale model by Dobramysl et al. (2016) was used to analyse Ca^{2+} puff statistics. Their model coupled the diffusion of ions with the stochastic dynamics of

IP_3Rs. When analysing their Ca^{2+} puff statistics, Dobramysl et al. (2016) only included IPIs greater than 0.25s apart, stating that IPIs less than 0.25s were caused by random channel re-openings. They fit their IPI distribution to a Gamma distribution.

Although the Exponential distribution has traditionally been used to describe the distribution of IPIs, it does not always capture the entire behaviour of the data. Distributions such as the Gamma distribution or Time-Dependent can describe the IPIs where the recovery from inhibition is slower.

Amplitude distribution

Amplitude distributions can be a key indicator of how many IP_3R exist in a cluster or the estimated mean number of IP_3R open during a Ca^{2+} puff (Dobramysl et al., 2016). Ca^{2+} puff amplitude distributions are often described as being asymmetric and few studies have fit statistical distributions to the Ca^{2+} puff amplitude data. However, statistical metrics, such as mean Ca^{2+} puff amplitude and maximum Ca^{2+} puff amplitude, can provide insight into IP_3R cluster dynamics.

Studies by Fraiman et al. (2006); Smith et al. (2009) describe the amplitude distributions as being asymmetric, with a higher frequency of low amplitudes. Dickinson et al. (2012) show amplitude distributions can be used to estimate the number of IP_3R that have contributed to a Ca^{2+} puff in SH-SU5Y cells. The amplitude distribution was formed of 7 Gaussian distributions, each representing the size of the channel cluster. When comparing amplitude distributions from mathematical simulations of Ca^{2+} puffs, Siekmann et al. (2019) fit the data to Gaussian distributions.

Although it is uncommon for statistical distributions to be fit to the Ca^{2+} puff amplitude distributions, here we have demonstrated the advantage of analysing this metric. Previous studies have used statistical metrics to estimate the IP_3R cluster size and the average number of IP_3R opening during a Ca^{2+} puff. While this provides valuable information on the structure of the IP_3R cluster, it also helps mathematicians in modelling the Ca^{2+} signalling system.

Duration distribution

The distribution of Ca^{2+} puff durations are rarely fit to statistical distributions. Literature of experimental data provides key statistics, without providing a visual description of puff durations. More commonly, mathematical modelling literature describes the puff duration's distributions.

Ullah et al. (2007) built a mathematical model that defines the critical determinants of Ca^{2+} signalling differentiation using Oocyte maturation. The study compared simulations from the Oocyte under three different conditions; the duration distributions were skewed to the right, however, no statistical distribution was fit to the data. Similarly, in a review by Siekmann et al. (2019) duration distributions are asymmetrical.

Thurley et al. (2012) state the Ca^{2+} puff duration distribution can be represented using the following statistical distribution:

$$d(t) = N\Gamma e^{-\Gamma t}(1 - e^{-\Gamma t})^{N-1} \tag{2.2}$$

where parameters include the duration of the puff (t), the number of channels open at the puff peak (N) and the average closing rate of the channels

(Γ).

Whilst duration distributions are a key metric when understanding the Ca^{2+} puff dynamics, fitting the distribution statistically is not common practice. Analysis of histogram appearance and statistical metrics can provide interesting insights into how IP_3R dynamics change within and across different cell types.

The aims of this chapter are:

2.1.1 Chapter Aims

- **Analyse Ca^{2+} puff statistics from human IP_3R1**

  Ca^{2+} puff statistics will be collected from experimental data, accessed through collaboration with Professor David Yule (Professor of Pharmacology and Physiology, University of Rochester). Data from exo 76 wild-type 1 IPR, wild-type IPR 1 and E2002D-type IPR 1 will be analysed and Ca^{2+} puff statistics compared (Arige et al., 2022).

- **Parameterise IPI distributions**

  IPI distributions are often described using the Exponential, Gamma or Time-Dependent distributions. We will parameterise the Exponential, Gamma and Time-Dependent distributions using IPI data from the three IP_3R and compare our results.

- **Calculate information criterion to determine statistically the strongest statistical distribution to represent the IPI distributions**

  Akaike information criterion, Bayesian information criterion and Watanabe Akaike information criterion will be calculated for each statistical

distribution. Comparison of values will help determine which statistical distribution best describes all variations of IPI distribution.

- **Investigate the statistical significance between the IPI distributions and statistical distributions**

  The Kolmogorov-Smirnov goodness of fit test will be conducted to compare each IPI distribution with the Exponential, Gamma and Time-Dependent distributions. The results from the statistical tests will be discussed and used to identify which statistical distribution best represents the IPI distributions.

2.2 Methods

2.2.1 Experimental data

Patch clamp testing

Patch clamp tests are used to analyse the current passing through an ion channel when ligand conditions are constant. A current of $\sim$ 0pA indicates a closed channel, whereas a current of ~ -40pA indicates an open channel. Through performing these tests, one can learn how the channel responds under different conditions and use results, such as the open probability and dwell time distributions (see Chapter 4) to parameterise a mathematical model that simulated similar behaviour.

Arige et al. (2022) investigated the effects of substitutions of the E2002 site on the fundamental Ca^{2+} signal's mediated by IP_3R. Stably over-expressed wild type hIP_3R were substituted at the 2002 glutamic acid residue with as-

partic acid. The number of puffs per cell, puff sites per cell and percentage of cells in which Ca^{2+} signals globalized were reduced in E2002D-type 1 IPR compared to wild-type 1 IPR. Through collaboration with the Yule lab, we have access to the data sets from both the wild-type 1 IPR and E2002D-type 1 IPR. Fig 2.1 and 2.2 present the patch clamp results by Arige et al. (2022) for wild-type 1 IPR and E2002D-type 1 IPR, respectively. Within these experiments ATP and IP_3 were kept constant at 5mM and 10µM, respectively.

We calculate the open probabilities for the wild-type 1 IPR and E2002D-type 1 IPR by using a threshold value of 50% of the maximum open current (-40pA) (Wagner and Yule, 2012). Values less than -20pA indicated the channel was open, while those above indicated the channel was closed. The open probability is calculated by summing the time the channel spends in the open state and dividing this result by the total number of transitions.

Dwell times were computed from the wild-type and E2002D type 1 IPR single channel data. These values show how long the IP_3R spends in the open or closed state conformation. Transition rates were calculated by taking the inverse of the average dwell time for each Ca^{2+} concentration.

Ca^{2+} puff data

To detect changes in Ca^{2+} concentrations within stable hIP_3R1, cells must go through a process of being washed with imaging buffer and incubated. Stable hIP_3R1 cells are firstly cultured on glass coverslips before being washed with imaging buffer. After going through different incubation periods, the coverslip is mounted in a chamber and imaged. Cells are illuminated using a laser to excite the fluorescent dye and the emitted dye is collected. Details of

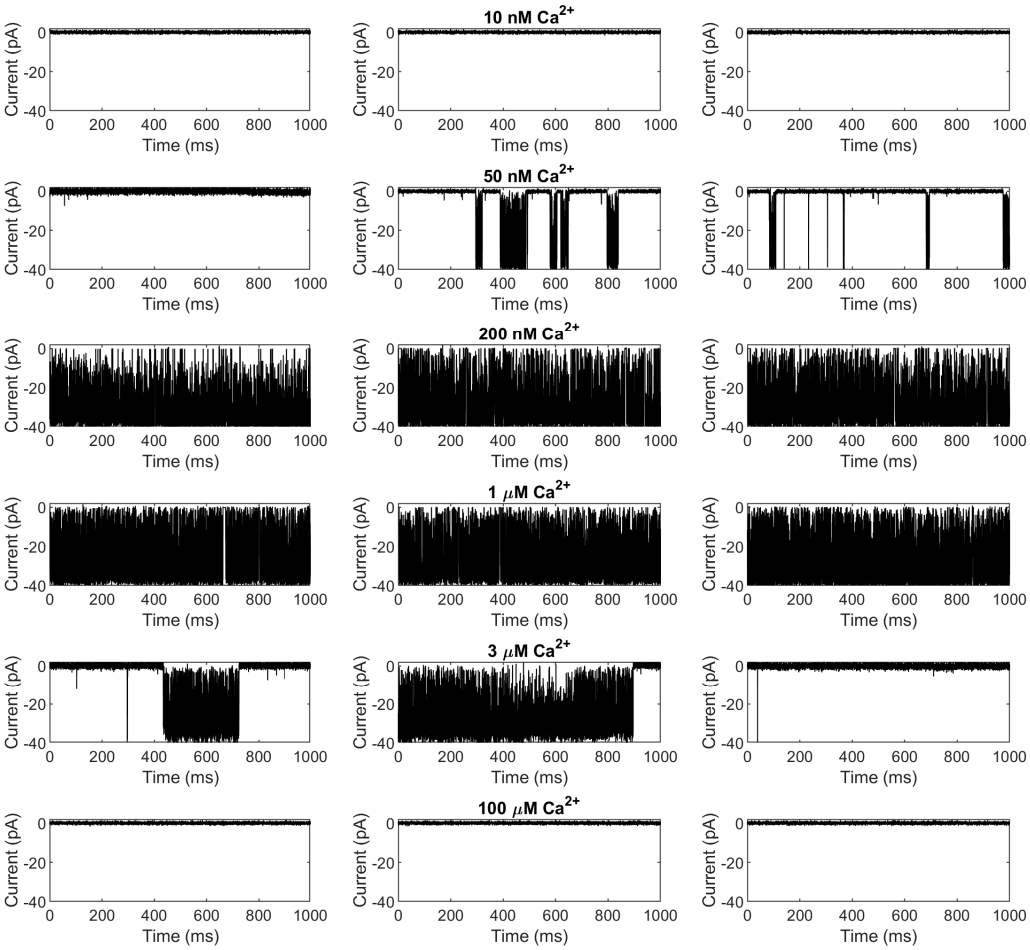

Figure 2.1: Patch clamp data from wild-type 1 IPR (Arige et al., 2022). IP_3 concentration was kept constant at $10\mu M$. The Ca^{2+} concentration is indicated above each plot.

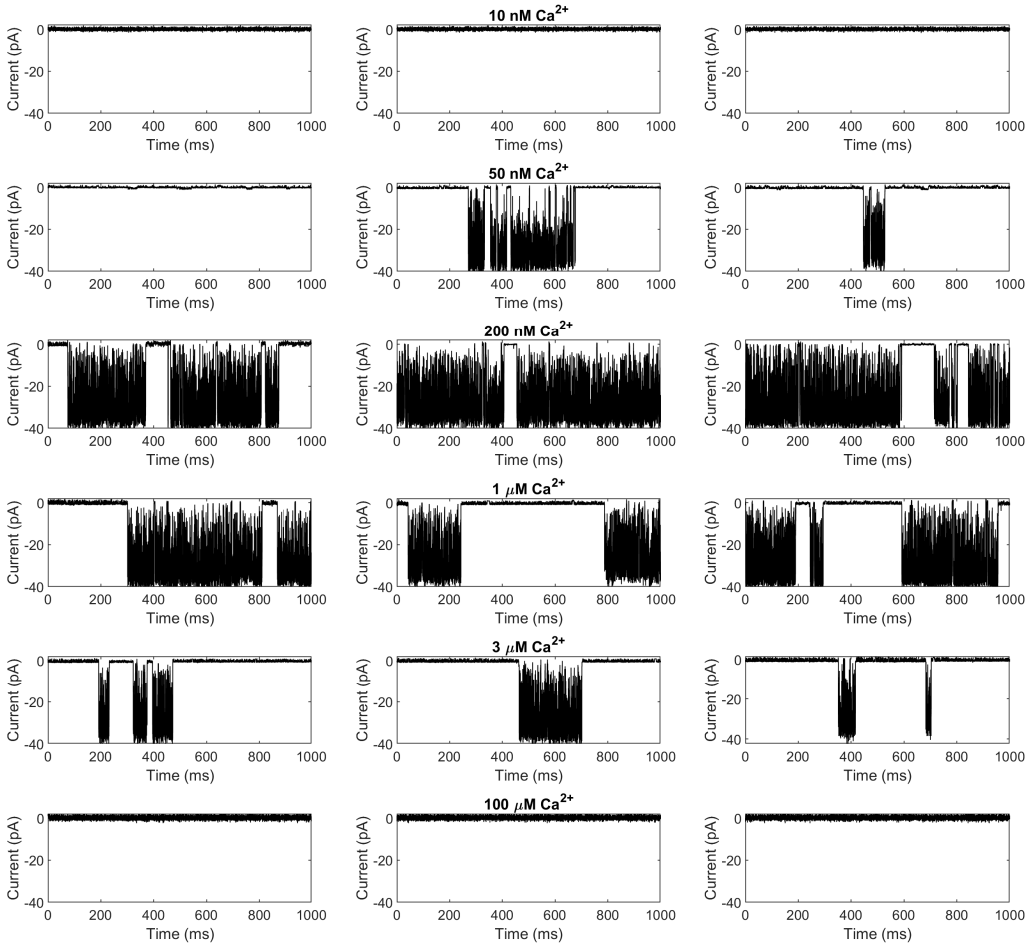

Figure 2.2: Patch clamp data from E2002D-type 1 IPR (Arige et al., 2022). IP_3 concentration was kept constant at $10\mu M$. The Ca^{2+} concentration is indicated above each plot.

the experimental conditions of the exo 76 wild-type 1 IPR, wild-type 1 IPR and E2002D-type 1 IPR can be found in Emrich et al. (2021); Arige et al. (2022). Examples of the images captured by Arige et al. (2022) are presented in Fig 2.3-2.4. In Fig 2.3, at 10s one can see two small bright areas in the frame. Over the frames, the Ca^{2+} concentration across the cell increases, shown by the spread of bright areas. In Fig 2.4 a singular bright area can be seen at 50s.

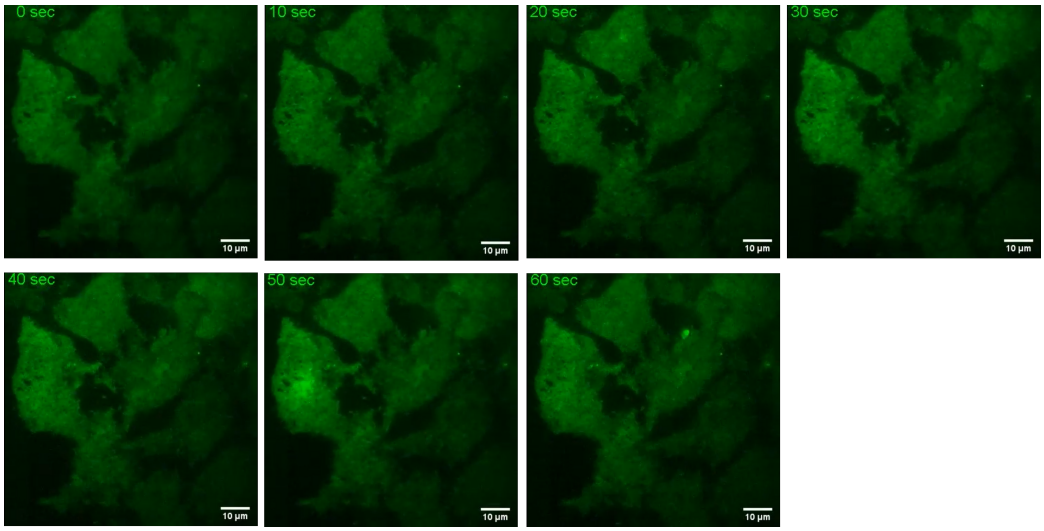

Figure 2.3: Frames from a Ca^{2+} puff experiment by Arige et al. (2022) from wild-type 1 IPR. Bright areas within the figure show a high concentration of Ca^{2+}. Permission to reproduce this image has been granted by Professor David Yule, University of Rochester, and Professor Irina Seryshevam, The University of Texas Health Science Center. `https://creativecommons.org/licenses/by-nc-nd/4.0/`

Fluorescence Ca^{2+} image stacks are converted into time series data using the Python-based platform, FLIKA (Ellefsen et al., 2014, 2019). This process was completed by Emrich et al. (2021); Arige et al. (2022) prior to our statistical analysis and further details can be found there. First, the raw movie is spatially and temporally filtered. Within FLIKA, the user can

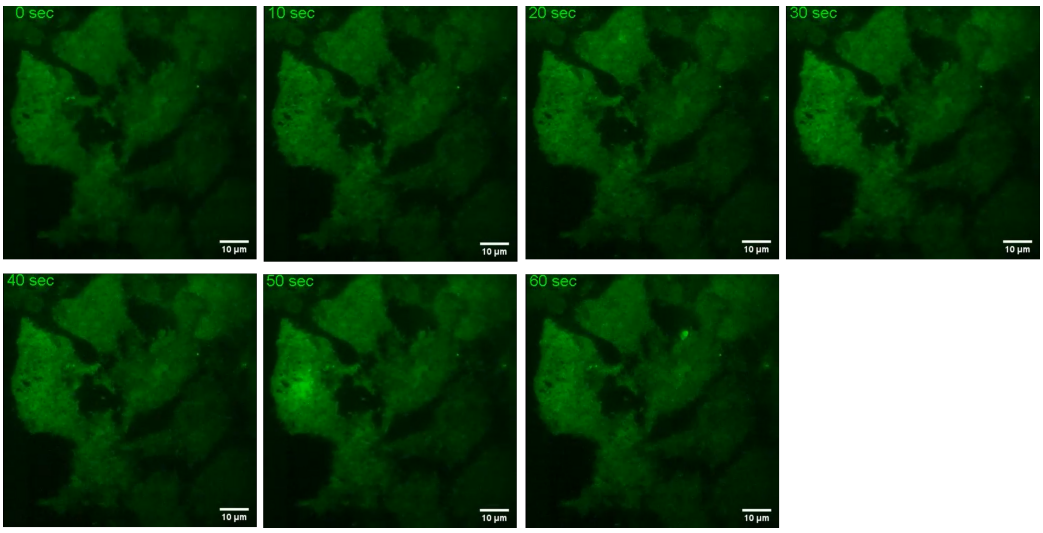

Figure 2.4: Frames from a Ca^{2+} puff experiment by Arige et al. (2022) from E2002D-type 1 IPR. Bright areas within the figure show a high concentration of Ca^{2+}. Permission to reproduce this image has been granted by Professor David Yule, University of Rochester, and Professor Irina Seryshevam, The University of Texas Health Science Center. `https://creativecommons.org/licenses/by-nc-nd/4.0/`

choose the filter best suited for their analysis (Ellefsen et al., 2014, 2019), Emrich et al. (2021); Arige et al. (2022) opted for the Gaussian filter. Next, the movie is thresholded using a user-defined threshold, chosen as 1.0 by Emrich et al. (2021); Arige et al. (2022). Pixels in the image stack above the threshold are marked as being part of a Ca^{2+} event. The pixels about the threshold are grouped into clusters using a clustering algorithm (Rodriguez and Laio, 2014; Ellefsen et al., 2019) which enables FLIKA to analyse the temporal evolution of each puff. Statistics, such as the peak amplitude, rise and fall times are saved in an Excel file (Ellefsen et al., 2019). Fig 2.5 shows an example of the Excel output from the FLIKA analysis.

In this chapter, we analyse two Ca^{2+} puff data sets. The first data set, named exo 76 wild-type 1 IPR in this thesis, is from unpublished data gained

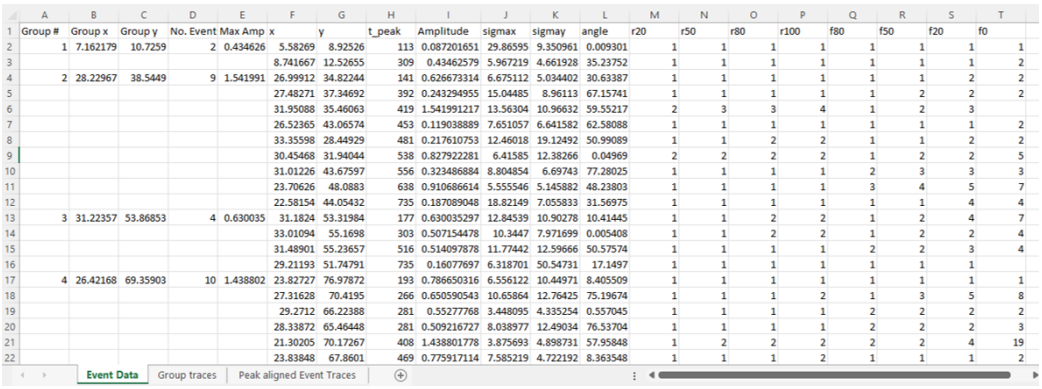

	A	B	C	D	E	F	G	H	I	J	K	L	M	N	O	P	Q	R	S	T
1	Group #	Group x	Group y	No. Event	Max Amp	x	y	t_peak	Amplitude	sigmax	sigmay	angle	r20	r50	r80	r100	f80	f50	f20	f0
2	1	7.162179	10.7259	2	0.434626	5.58269	8.92526	113	0.087201651	29.86595	9.350961	0.009301	1	1	1	1	1	1	1	1
3						8.741667	12.52655	309	0.43462579	5.967219	4.661928	35.23752	1	1	1	1	1	1	1	2
4	2	28.22967	38.5449	9	1.541991	26.99912	34.82244	141	0.626673314	6.675112	5.034402	30.63387	1	1	1	1	1	1	2	2
5						27.48271	37.34692	392	0.243294955	15.04485	8.96113	67.15741	1	1	1	1	1	2	2	2
6						31.95088	35.46063	419	1.541991217	13.56304	10.96632	59.55217	2	3	3	4	1	2	3	
7						26.52365	43.06574	453	0.119038889	7.651057	6.641582	62.58088	1	1	1	1	1	1	1	2
8						33.35598	28.44929	481	0.217610753	12.46018	19.12492	50.99089	1	1	2	2	1	1	2	2
9						30.45468	31.94044	538	0.827922281	6.41585	12.38266	0.04969	2	2	2	2	1	2	2	5
10						31.01226	43.67597	556	0.323486884	8.804854	6.69743	77.28025	1	1	1	1	2	3	3	3
11						23.70626	48.0883	638	0.910686614	5.555546	5.145882	48.23803	1	1	1	1	3	4	5	7
12						22.58154	44.05432	735	0.187089048	18.82149	7.055833	31.56975	1	1	1	1	1	1	4	4
13	3	31.22357	53.86853	4	0.630035	31.1824	53.31984	177	0.630035297	12.84539	10.90278	10.41445	1	1	2	2	1	2	4	7
14						33.01094	55.1698	303	0.507154478	10.3447	7.971699	0.005408	1	1	2	2	1	2	2	4
15						31.48901	55.23657	516	0.514097878	11.77442	12.59666	50.57574	1	1	1	1	2	2	3	4
16						29.21193	51.74791	735	0.16077697	6.318701	50.54731	17.1497	1	1	1	1	1	1	1	
17	4	26.42168	69.35903	10	1.438802	23.82727	76.97872	193	0.786650316	6.556122	10.44971	8.405509	1	1	1	1	1	1	1	1
18						27.31628	70.4195	266	0.650590543	10.65864	12.76425	75.19674	1	1	1	2	1	3	5	8
19						29.2712	66.22388	281	0.55277768	3.448095	4.335254	0.557045	1	1	1	1	2	2	2	2
20						28.33872	65.46448	281	0.509216727	8.038977	12.49034	76.53704	1	1	1	1	2	2	2	3
21						21.30205	70.17267	408	1.438801778	3.875693	4.898731	57.95848	1	2	2	2	2	2	4	19
22						23.83848	67.8601	469	0.775917114	7.585219	4.722192	8.363548	1	1	1	2	1	1	1	2

Event Data | Group traces | Peak aligned Event Traces

Figure 2.5: Example of the Excel output from FLIKA analysis. Units of metrics are in the number of frames. Definitions of the metrics can be found in Ellefsen et al. (2014).

through collaboration with the Yule Lab, Rochester. For this data set, we convert the frame rate into seconds at a ratio of 166 frames per second as detailed in Emrich et al. (2021). The aim of using the exo 76 wild-type 1 IPR data set is to compare wild-type Ca^{2+} puff statistics and investigate variability amongst data sets.

The second Ca^{2+} puff data set has been previously published by Arige et al. (2022). This data set includes Ca^{2+} puff data from wild-type 1 IPR and wild-type 1 IPR that have been substituted at the 2002 glutamic acid residue with aspartic acid (E2002D-type 1 IPR). The frame rate to seconds ratio is converted as 50 frames per second and further experimental details can be found in Arige et al. (2022).

IPIs are calculated by finding the time between the termination of the first Ca^{2+} puff to the onset of the next Ca^{2+} puff. We define the termination of a Ca^{2+} puff as the time the Ca^{2+} concentration is 20% of the peak puff amplitude after the Ca^{2+} peak. Similarly, the onset of a Ca^{2+} puff is the time at which the Ca^{2+} concentration is 20% of the peak puff amplitude before the

Ca^{2+} peak. Thus, the Ca^{2+} puff durations are calculated as the difference between the termination and onset of a Ca^{2+} puff.

2.2.2 Probability Distributions

We parameterise the Exponential, Gamma and Time-Dependent distributions using IPI data. Maximum likelihood estimates (MLE) are used to estimate parameters of models (Myung, 2003; Brooks-Bartlett, 2018). Through using MLE the parameter values of a chosen probability distribution that best represent the observed data can be found (Myung, 2003). MLE is used within a variety of statistical tests such as the chi-square test, Bayesian method and model selection criteria such as AIC and BIC (Myung, 2003). It is calculated by first, finding the likelihood function, that is the product of the density terms of the chosen statistical distribution. Second, the natural log of the likelihood function is taken. Finally, the log-likelihood is differentiated and set equal to zero giving the value at which the likelihood is maximised (Stephens, 2004).

The statistical distributions are as follows:

Exponential Distribution

$$P_{IPI} = \lambda e^{-\lambda t} \tag{2.3}$$

λ represents the rate parameter.

Gamma Distribution

$$P_{IPI} = \frac{\beta^{\alpha}}{\Gamma(\alpha)} x^{\alpha-1} e^{-\beta t} \tag{2.4}$$

α and β represent the shape and rate parameters, respectively.

Time-Dependent

$$P_{IPI} = \lambda \left(1 - e^{-\xi t}\right) e^{\left[-\lambda t + \lambda\left(1 - e^{-\xi t}\right)/\xi\right]} \tag{2.5}$$

λ and ξ represent the rate and refractory period parameters, respectively.

2.2.3 Information criteria for model selection

Information criterion is used to provide a statistical indication as to which probability distribution fits the data best. We calculate the Akaike information criteria (AIC), Bayesian information criteria (BIC) and Watanabe Akaike information criteria (WAIC) and compare the results across the different distributions and for different experimental data sets.

Akaike Information Criteria

AIC is calculated by taking the log predictive density, also referred to as the log-likelihood, and subtracting a penalty factor, k, which represents the number of estimated parameters and is used to correct for overfitting. The calculation is scaled by -2 (Gelman et al., 2013).

$$AIC = -2log_p\left(y|\hat{\theta}_{mle}\right) + 2k \tag{2.6}$$

For small sample sizes, where $\frac{n}{k} < 40$, an adjusted version of AIC is used that includes a second-order bias correction (Burnham and Anderson, 2004):

$$AIC_s = -2log_p\left(y|\hat{\theta}_{mle}\right) + 2k + \frac{2k(k+1)}{n-k-1} \tag{2.7}$$

Bayesian Information Criterion

BIC is calculated by taking the log-likelihood and adding a penalty factor which takes into consideration the sample size of the observed data, n (Schwarz, 1978; Gelman et al., 2013).

$$BIC = -2log_p\left(y|\theta\right) + kln(n) \tag{2.8}$$

Watanabe-Akaike Information Criterion

To calculate WAIC, the entire posterior distribution, $p(\theta|y)$, is used. This is calculated by combining the likelihood $p(y|\theta)$ and the prior density, $p(\theta)$ and summaries all current knowledge about θ (Lee, 2014; Annis et al., 2017). That is:

$$p(\theta|y) = \frac{p(\theta)p(y|\theta)}{\int p(\theta)p(y|\theta)d\theta} \tag{2.9}$$

Bayes Theorem can be written as:

$$p(\theta|y) \propto p(y|\theta) \cdot p(\theta) \ \ (Lee,\ 2014) \tag{2.10}$$

The posterior distribution can be calculated using numerical methods, or for more complex models, by using a Markov chain Monte Carlo (MCMC) algorithm. Within our analysis, we opt to use MCMC within the Stan (Stan-Development-Team., 2019; Stan-Development-Team, 2020). See Section 2.2.5 for more details on using Stan within R.

WAIC is calculated by taking the log pointwise predictive density (lppd) and adjusting for overfitting (Watanabe, 2010; Gelman et al., 2013).

The lppd is computed by, firstly, calculating the predictive density. This

involves drawing S samples from the posterior distribution and calculating the predictive density for each sample, $p(y_i|\theta^S)$. The predictive densities are then averaged. Next, the log of the approximated average predictive density is calculated and summed over the number of data points, n. The lppd is an overestimate of the expected lppd for future data, therefore it can be used as an estimate for future data (Gelman et al., 2014; Vehtari et al., 2017).

$$lppd = \sum_{i=1}^{n} log\left(\frac{1}{S}\sum_{S=1}^{S} p\left(y_i|\theta^S\right)\right) \tag{2.11}$$

p_{WAIC2} is used to adjust for overfitting and can be interpreted as an approximation to the number of 'unconstrained' parameters in the model (Gelman et al., 2013). p_{WAIC2} is calculated by taking the variance of the log-likelihood for each observation and summing over the number of observations.

$$P_{WAIC2} = \sum_{i=1}^{n} var_{post}\left(logp\left(y_i|\theta\right)\right) \tag{2.12}$$

WAIC is scaled by -2 to make it comparable with other information criterion (Gelman et al., 2013).

$$WAIC = -2lppd + 2p_{WAIC} \tag{2.13}$$

To calculate WAIC, a prior distribution needs to be chosen for each of the unknown parameters. Formally, the prior is used to encode relevant information to the problem being analysed, however, it is often used as a means of stabilising inferences in complex, high-dimensional problems (Vehtari et al., 2017). When all parameters are believed to be equally as likely and exist within a finite interval, uniform, or flat distributions are sometimes chosen

(Annis et al., 2017). This results in the prior having little effect on the posterior (Vehtari et al., 2017). Within this analysis, the Exponential distribution is chosen as a prior and is represented by Eq 2.14, where r is the rate parameter of the prior. By setting r to be very small, the Exponential distribution decays slowly making it appear like a non-informative uniform distribution for a small λ. Whilst λ can span $[0, \infty]$, $P(\lambda)$ penalises very fast λ values.

$$P(\lambda) = re^{-r\lambda} \tag{2.14}$$

2.2.4 Kolmogorov-Smirnov goodness of fit test

The Kolmogorov-Smirnov goodness of fit test investigates the statistical difference between observed data and a chosen statistical distribution (Kanji, 2006). To use this test, data must be continuous (Panik, 2005). Within this thesis, we use the Kolmogorov-Smirnov test to compare the IPI distributions, calculated from each of our experimental data sets, with the Exponential, Gamma and Time-Dependent distributions. We let $X_1, X_2, ...X_n$ be the IPI data from the Ca^{2+} puff statistics, gathered from the exo 76 wild-type 1 IPR, wild-type 1 IPR and E2002D-type 1 IPR experimental data and $F_n(x)$ be the empirical cumulative distribution function (CDF) from each IPI data set (Kvam et al., 2023).

The hypothesis test is:

$$\begin{aligned} H_0 &: F(x) = F_0(x) \\ H_1 &: F(x) \neq F_0(x) \end{aligned} \tag{2.15}$$

Where $F_0(x)$ represents the CDF from either the Exponential, Gamma, or Time-Dependent distribution. We use a significance level, α, of 0.05. The Kolmogorov-Smirnov test statistic, D, is calculated as the maximum vertical difference between the empirical CDF, $F_n(x)$, and the theoretical CDF, $F_0(x)$ (Panik, 2005).

$$D_n = max|F_n(x_i) - F_0(x_i)| \tag{2.16}$$

If D_n is large, it suggests the theoretical CDF is not a good representation of the empirical CDF. We plot the empirical and theoretical CDF against each other to allow us to compare the distributions visually (Kvam et al., 2023). Alongside performing the Kolmogorov-Smirnov test statistic, we calculate the p-value. If $p < \alpha$, we reject H_0.

2.2.5 Numerical methods

We calculate the IPI, Ca^{2+} puff amplitude and Ca^{2+} puff duration using MATLAB. Statistical analysis of the Ca^{2+} puff statistics including parameterisation and information criterion was calculated using R. WAIC was calculated using the rstan package by Vehtari et al. (2017) (Annis et al., 2017; Vehtari et al., 2017; Stan-Development-Team., 2019; Stan-Development-Team, 2020).The Exponential and Gamma distributions are built into the Stan application, however, for the Time-Dependent distribution a user-defined distribution was built. This involved defining the log-likelihood of the Time-Dependent distribution within Stan. Once completed, the distribution can be called like a built-in distribution (Annis et al., 2017; Vehtari et al., 2017; Stan-Development-Team., 2019; Stan-Development-Team, 2020). We used a warmup step of 1000, an interation step of 2000 and 4 chains when running

our MCMC algorithm. All figures were created in MATLAB.

2.3 Results

2.3.1 Stationary single channel data analysis

In Fig 2.6 we present the open probabilities for the wild-type and E2002D-type 1 IPR. A clear distinction between the wild-type and E2002D-type 1 IPR open probabilities is that the substitution of the 2002 glutamic acid residue with aspartic acid causes a less active IP_3R evidenced by the smaller open probabilities. Although this substitution reduces the open probability of the IP_3R , the open probability curve retains its bell-shaped curve.

A Ca^{2+} concentration of 10nM and 100µM does not activate the IP_3R, however when the Ca^{2+} concentration is at 200nM or 1µM the channel is very active. In comparison to results from the wild-type 1 IPR, the E2002D-type 1 IPR is less active. Transition rates and P_o values are given in Table 2.1. The higher transition rates observed in the wild-type 1 IPR, in comparison to those in the mutated channel, indicate that the wild-type channel is more active.

Table 2.1: Transition rates and P_o for the wild-type 1 IPR and E2002D-type 1 IPR

Ca^{2+} (nM)	Wild-type 1 IPR			E2002D-type 1 IPR		
	$q_{oc\infty}(s^{-1})$	$q_{co\infty}(s^{-1})$	P_o	$q_{oc\infty}$	$q_{co\infty}$	P_o
10	-	-	0	-	-	0
50	2.009	0.3933	0.1627	0.8527	0.1313	0.1305
200	0.9749	4.4678	0.8208	1.0773	1.0655	0.4948
1000	1.7389	5.6471	0.7645	1.0155	0.9006	0.4638
3000	1.5654	0.6536	0.2937	1.0903	0.3319	0.2259
100 000	-	-	0	-	-	0

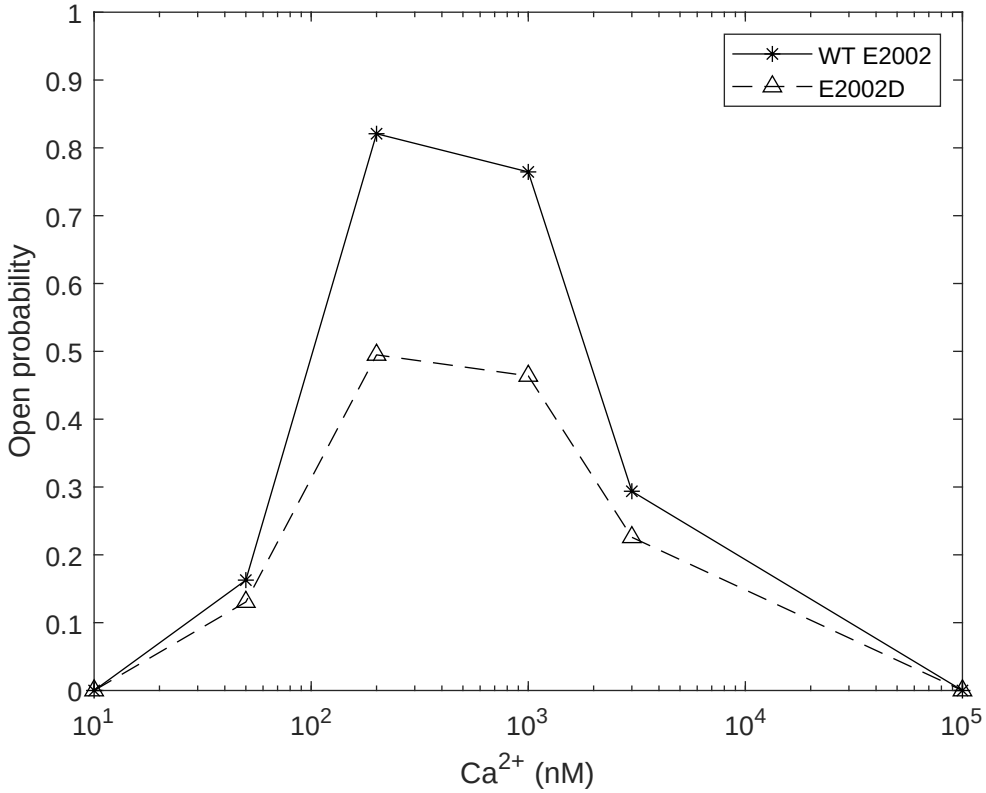

Figure 2.6: Pooled open probabilities from wild-type 1 IPR and E2002D-type 1 IPR (Arige et al., 2022).

In Fig 2.7 we compare the open state dwell time distributions for differing Ca^{2+} concentrations for the wild-type 1 IPR and E2002D-type 1 IPR. Due to the IP_3R being consistently closed when the Ca^{2+} concentration was 10nM and 100µM, there are no open state dwell times. A clear difference between the distributions is that the wild-type 1 IPR is much more active, evidenced by the significantly higher count of open events. The time spent in the open state for the wild-type 1 IPR is often much shorter than the E2002D-type 1 IPR.

Fig 2.8 shows the close state dwell time distributions for the wild-type 1 IPR and E2002D-type 1 IPR. Both IP_3R exhibit short and long dwell times. The E2002D-type 1 IPR spends more time in the closed state. Comparison of the open and close state dwell time distributions demonstrates, firstly the wild-type 1 IPR is more active than the E2002D-type 1 IPR shown by the higher frequency of events. Secondly, the E2002D-type 1 IPR spends a longer time in a closed state.

2.3.2 Statistical analysis of Ca^{2+} puffs

This section details the results of statistical analysis conducted on two data sets. Firstly, we analyse Ca^{2+} puffs from unpublished data gained through collaboration with the Yule Lab, Rochester. Secondly, we analyse Ca^{2+} puff data from Arige et al. (2022). This includes Ca^{2+} puff data from wild-type 1 IPR and wild-type 1 IPR that have been substituted at the 2002 glutamic acid residue with aspartic acid (E2002D-type 1 IPR). Results from wild-type 1 IPR and E2002D-type 1 IPR will be used in Chapter 4 of this thesis.

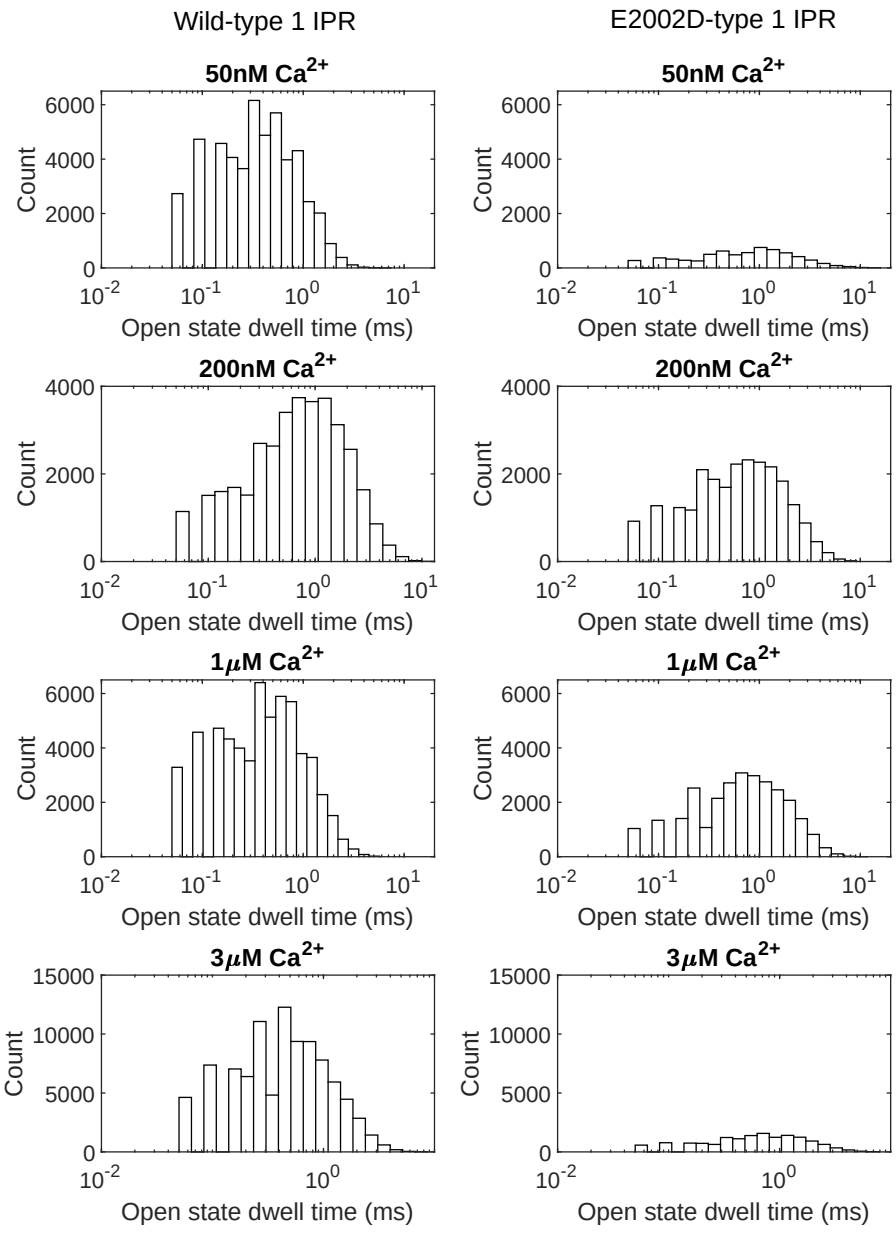

Figure 2.7: Open state dwell times for different Ca^{2+} concentrations for the wild-type 1 IPR and E2002D-type 1 IPR. The open state dwell time distributions have been log-transformed.

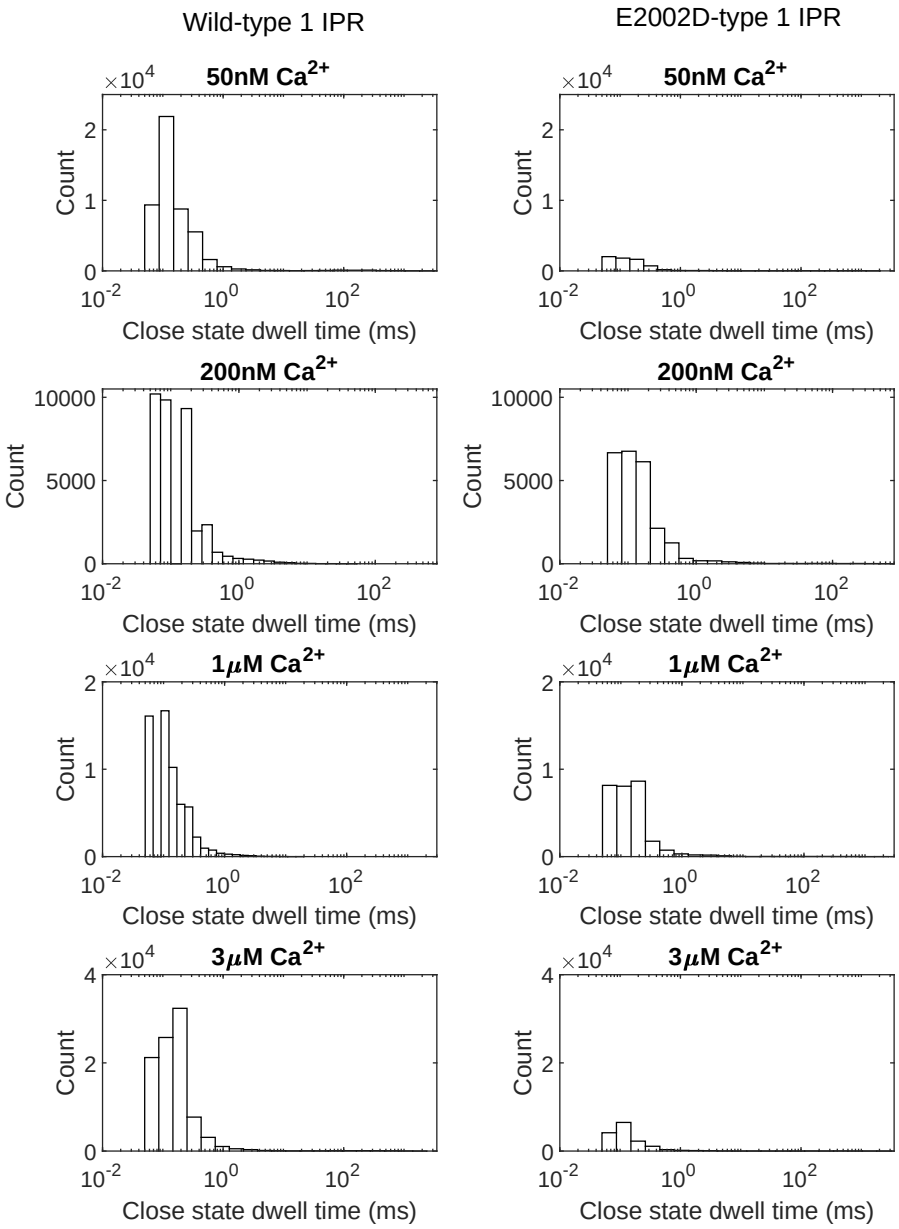

Figure 2.8: Close state dwell times for different Ca^{2+} concentrations for the wild-type 1 IPR and E2002D-type 1 IPR. The closed state dwell time distributions have been log-transformed.

Exo 76 wild-type IPR In Fig 2.9, we compare the Ca^{2+} puff statistics distributions from exo 76 wild-type IPR. Each row in Fig 2.9 contains Ca^{2+} puff statistic data from different experimental groups produced by exo wild-type 1 IPR. All IPI distributions are skewed to the right with a higher frequency of short IPIs. Although the data is derived from the same IP_3R , the distributions exhibit variability. Some IPIs have a higher frequency of shorter durations, which gives rise to an Exponential distribution. On the other hand, some IPI distributions have an ascending slope before decaying. All amplitude distributions are skewed to the right, peaking at a lower Ca^{2+} concentration. Qualitatively, the puff duration distributions appear to be right-skewed. All distributions have a long tail, with the maximum duration across all data sets being 0.33s.

In Table 2.2 we present the summary statistics for each experimental group. The mean and median values for each group are similar. The range of IPIs is very large, suggesting that the IP_3R have times of high and low activity. The minimum Ca^{2+} puff amplitude is 72.97nM, whereas the largest is 2467.19nM. The median and mean values for each experimental group are similar.

In Fig 2.10, we compare the spread and density of the Ca^{2+} puff statistics using violin plots. We present data from each experimental group and pooled results. Whilst all amplitude and duration distributions appear to be uni-modal, showing a high density of low values, only two of the IPI distributions follow this shape. One of the experimental groups in the study has a distribution with a higher density of larger IPI when compared to the other groups. However, it is important to note that this group has fewer data

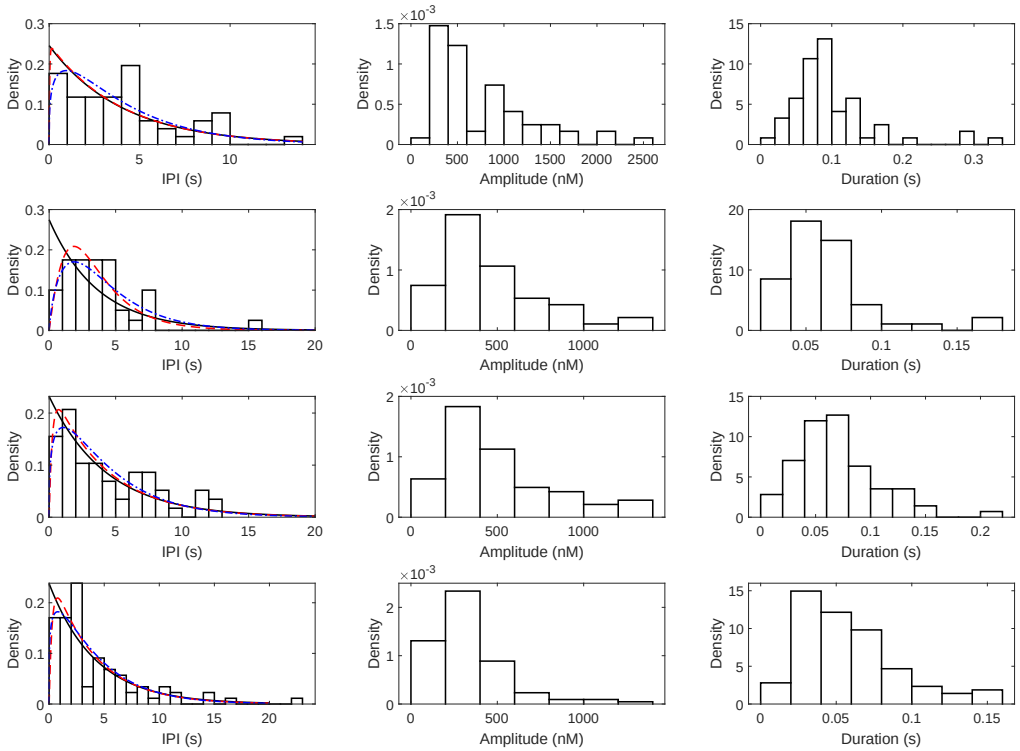

Figure 2.9: Ca^{2+} puff statistics for different experimental groups from exo 76 wild-type 1 IPR. The plots show the Exponential distribution as a solid black line, the Gamma distribution as a dot-dashed blue line, and the Time-Dependent distribution as a red-dashed line.

Table 2.2: Exo 76 wild-type 1 IPR Ca^{2+} puff summary statistics

Exo 76 wild-type 1 IPR summary statistics						
Interpuff interval (s)						
	Min.	1st Qu.	Median	Mean	3rd Qu.	Max.
1	0.06	1.53	3.78	4.07	5.33	13.03
2	0.12	1.67	3.44	3.64	4.52	15.81
3	0.19	1.52	3.19	4.31	6.64	12.83
4	0.10	1.41	2.72	4.21	5.80	22.64
Ca^{2+} puff amplitude (nM)						
	Min.	1st Qu.	Median	Mean	3rd Qu.	Max.
1	190.79	324.63	552.32	764.57	1065.82	2467.19
2	161.25	247.20	380.31	473.90	586.30	1373.05
3	102.30	267.58	403.68	508.76	646.41	1341.89
4	72.97	196.80	296.05	344.35	414.92	1378.47
Ca^{2+} puff duration (s)						
	Min.	1st Qu.	Median	Mean	3rd Qu.	Max.
1	0.01	0.07	0.09	0.10	0.11	0.33
2	0.02	0.04	0.05	0.06	0.07	0.17
3	0.01	0.04	0.07	0.07	0.09	0.21
4	0.01	0.04	0.05	0.06	0.07	0.15

points which may have caused the difference in distribution shape. Despite this difference, the mean and median values are similar for each group.

We parameterise the Exponential, Gamma and Time-Dependent distributions using the IPI data. Parameter results are presented in Table 2.3 and the statistical distributions are shown in Fig 2.9. Thurley et al. (2011); Cao et al. (2013) explain that the Time-Dependent distribution can be reduced to an Exponential distribution when $\xi >> \lambda$. All ξ estimates for our data are greater than the λ estimates. Estimated α parameters for the Gamma distribution are greater than 1 and β parameters are less than 0.5. This suggests the IPI distributions show refractoriness - $\alpha > 1$, therefore the probability of having smaller IPIs is lower. All λ estimates for the Exponential distributions range between 0.0232 and 0.275, emphasising the average IPI is similar across each data set. The Time-Dependent and Gamma distributions qualitatively follow a similar shape for three of the IPI distributions. A gradual rise can be seen in three of the IPI distributions which the Exponential distribution cannot model. This is due to the Exponential distribution having a faster rate caused by the higher frequency of short IPIs leading to the distribution underestimating longer IPIs. The Gamma distribution appears to model the shape of these distributions better. We pooled the IPI data for all four data sets and estimated the parameters for the Exponential, Gamma and Time-Dependent distributions. The pooled experimental data and statistical distributions are presented in Fig A.1.

To statistically determine which statistical distribution is the best representation of IPI distributions, we calculate AIC, BIC and WAIC values and compare them for each data set. The information criterion results are

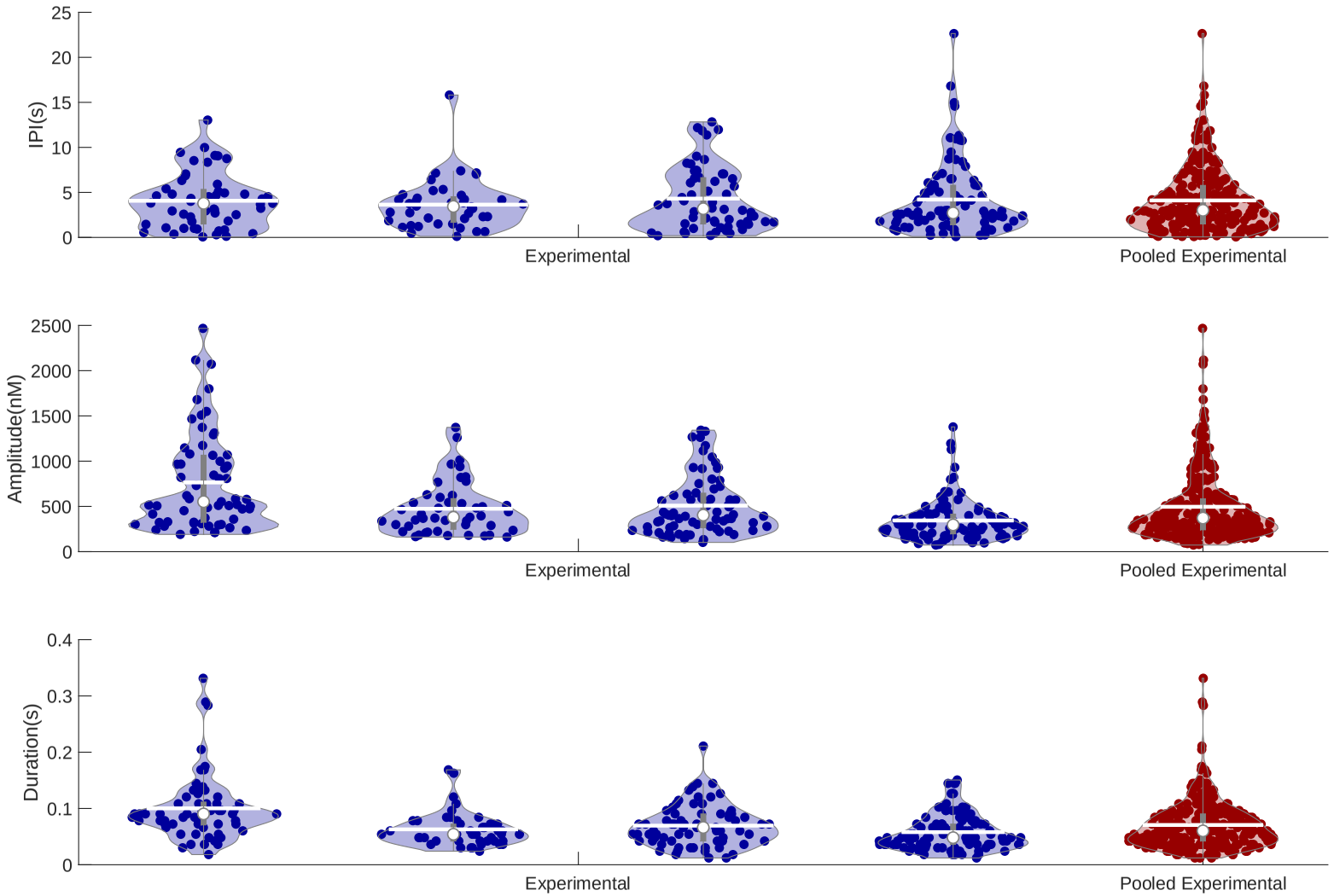

Figure 2.10: Violin plots of the Ca^{2+} puff statistics for exo 76 wild-type 1 IPR

Table 2.3: Parameter estimates using MLE for interpuff interval distributions from exo 76 wild-type 1 IPR

Data set	Exponential	Gamma		Time-Dependent	
	λ	α	β	λ	ξ
1	0.2457	1.3048	0.3206	0.2475	33.2900
2	0.2747	1.7914	0.4921	0.4197	0.6144
3	0.2320	1.3290	0.3084	0.2454	4.1489
4	0.2378	1.2271	0.2918	0.2538	3.6404
Pooled	0.2435	1.3347	0.3249	0.2597	3.7766

presented in Table 2.4. The lowest value indicates the best-fitting statistical distribution. Our first observation from comparing each information criterion is that they are very similar for each data set and model. For the first data set, the smallest AIC value is for the Gamma distribution, however, the smallest BIC is for the Exponential distribution and the smallest WAIC value is for the Time-Dependent distribution. This suggests the three statistical distributions can model the IPI data equally well. When comparing results for the second data set, AIC, BIC and WAIC are all lowest for the Gamma distribution. The third data set had the lowest AIC value for the Time-Dependent distribution, BIC value for the Exponential distribution and WAIC value for the Gamma distribution. AIC and WAIC values were lowest for the Time-Dependent distribution for the fourth data set, however, WAIC was lowest for the Exponential distribution. We calculated the AIC, BIC and WAIC values for the pooled experimental data; all three information criteria had the smallest values for the Gamma distribution.

Fig 2.11 presents the empirical CDF from IPI samples from the exo 76 wild-type IPR compared with model CDF. The Exponential CDF has the worst fit to the empirical CDF for all IPI data sets. The Gamma and Time-

Table 2.4: Information criteria for exo 76 wild-type 1 IPR

	Exponential			Gamma			Time-Dependent		
	AIC	BIC	WAIC	AIC	BIC	WAIC	AIC	BIC	WAIC
1	247.18	**249.11**	246.69	**247.12**	250.98	247.29	248.75	252.61	**246.68**
2	185.36	187.06	184.97	**180.51**	**183.89**	**181.70**	180.79	184.17	184.91
3	287.47	**289.53**	287.17	286.80	290.92	**286.53**	**286.75**	290.87	287.16
4	430.82	**433.30**	430.82	430.65	435.61	431.04	**429.27**	434.22	**430.72**
Pooled	1145.59	1149.06	1145.27	**1136.37**	**1143.31**	**1136.29**	1139.65	1146.58	1145.18

Dependent CDF are more comparable to the empirical CDF. Table 2.5 shows the p-value and test statistic calculated from conducting the Kolmogorov-Smirnov test. Across all IPI data sets, including the pooled IPI data, we reject H_0 for the Exponential CDF at the 5% level of significance. There is not enough evidence to reject H_0 at the 5% significance level for the Gamma and Time-Dependent distribution. A comparison of the empirical CDF for the pooled IPI data and each model CDF is shown in Fig A.2.

Table 2.5: Kolmogorov-Smirnov Test: p-value and test statistics for exo wild-type 1 IPR IPI distributions

		Exponential	Gamma	Time-Dependent
1	P-value	$4.8374e^{-32}$	0.5643	0.2005
	Test statistic	0.8296	0.1072	0.1469
2	P-value	$2.5610e^{-28}$	0.8804	0.8902
	Test statistic	0.8770	0.0891	0.0879
3	P-value	$3.4843e^{-37}$	0.7468	0.7247
	Test statistic	0.8401	0.0864	0.0882
4	P-value	$9.4509e^{-61}$	0.2458	0.4359
	Test statistic	0.8772	0.1072	0.0909
Pooled	P-value	$9.8075e^{-152}$	0.9984	0.4890
	Test statistic	0.8575	0.0244	0.0535

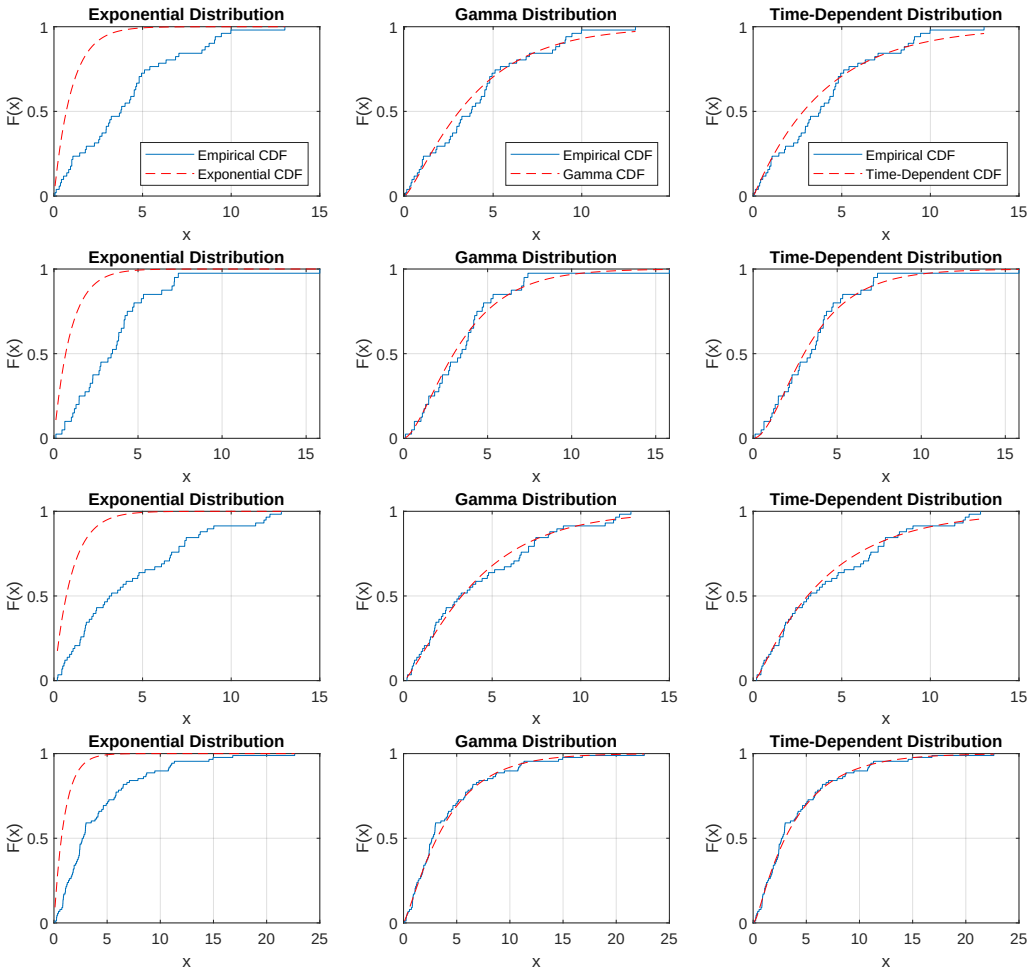

Figure 2.11: Comparison of the Exponential, Gamma and Time-Dependent cumulative density function with the empirical cumulative density function of the IPI sample from the exo 76 wild-type 1 IPR IPI data

Ca^{2+} puff data from Arige et al. (2022)

Wild-type 1 IPR In Fig 2.12-2.13 we present the Ca^{2+} puff statistics from 10 experimental data sets. Each IPI distribution is parameterised with the Exponential, Gamma and Time-Dependent distributions. All IPI distributions are skewed to the right and have a high frequency of short IPIs. Most IPI distributions range between 0 and 6s, except for two data sets which include longer IPIs. Pooled IPI data, presented in Fig A.1, shows an increase in IPI density prior to an exponential decay. The amplitude distributions are all right-skewed, evidencing at a high frequency of smaller Ca^{2+} puff events. Whilst the maximum Ca^{2+} puff amplitude for most data sets is ≈3000nM, one data set includes extremely high Ca^{2+} puff amplitudes with a maximum of 10 668.57nM. Many of the duration distributions are right-skewed with a peak close to 0.1s. The largest Ca^{2+} puff duration is 0.48s. Summary statistics can be found in Table 2.3.2.

Fig 2.14 presents violin plots of the Ca^{2+} statistics for each wild-type 1 IPR experimental group and the pooled data. As shown in Fig 2.12-2.13, the spread of the IPI data in each experimental group is very similar. All IPI, Ca^{2+} puff amplitude and Ca^{2+} puff duration distributions are uni-modal. IPI distributions have a high frequency of small IPIs with comparable mean and median values. Similarly, the amplitude distributions all have a high frequency of short amplitudes. It is difficult to determine whether there is a correlation between data sets with long IPIs and amplitudes as this is only observed in one data set. A study by Fraiman et al. (2006) showed a strong correlation between Ca^{2+} puff size and IPI duration in Xenopus laevis Oocytes. However, this was only observed in conditional distributions.

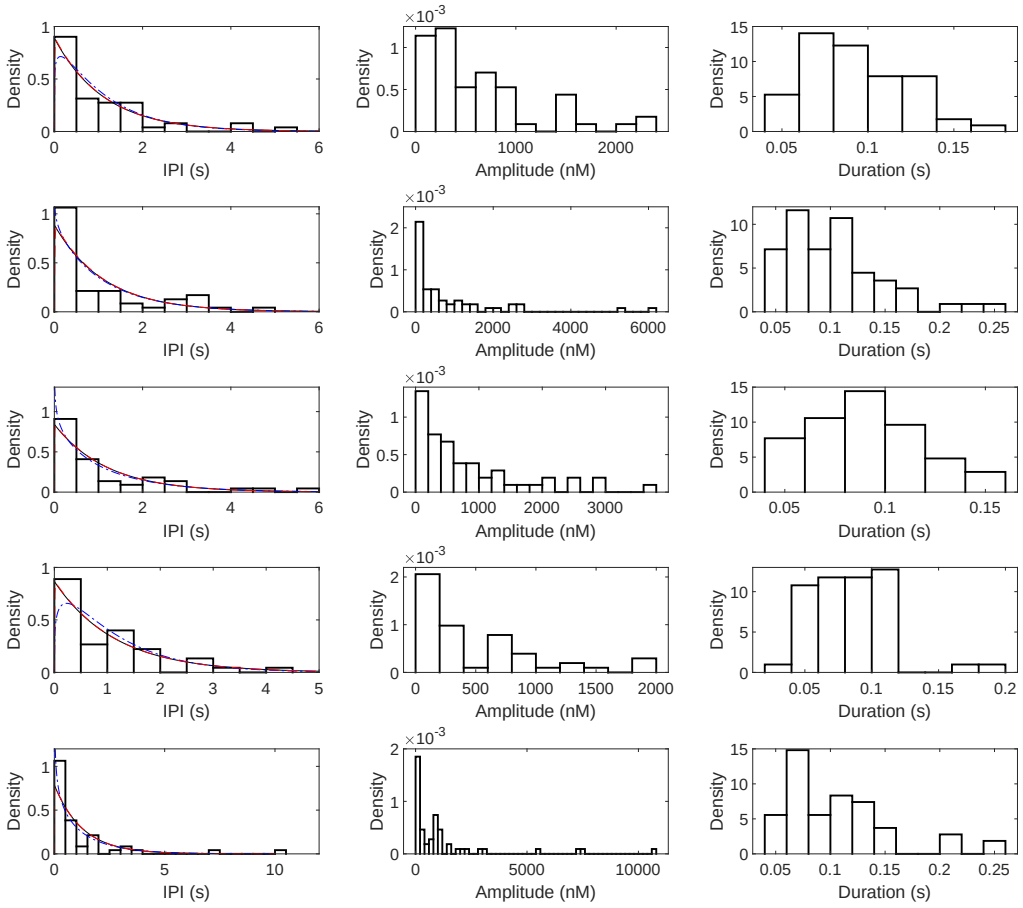

Figure 2.12: Ca^{2+} puff statistics for wild-type 1 IPR. Data sets 1-5. The plots show the Exponential distribution as a solid black line, the Gamma distribution as a dot-dashed blue line, and the Time-Dependent distribution as a red-dashed line.

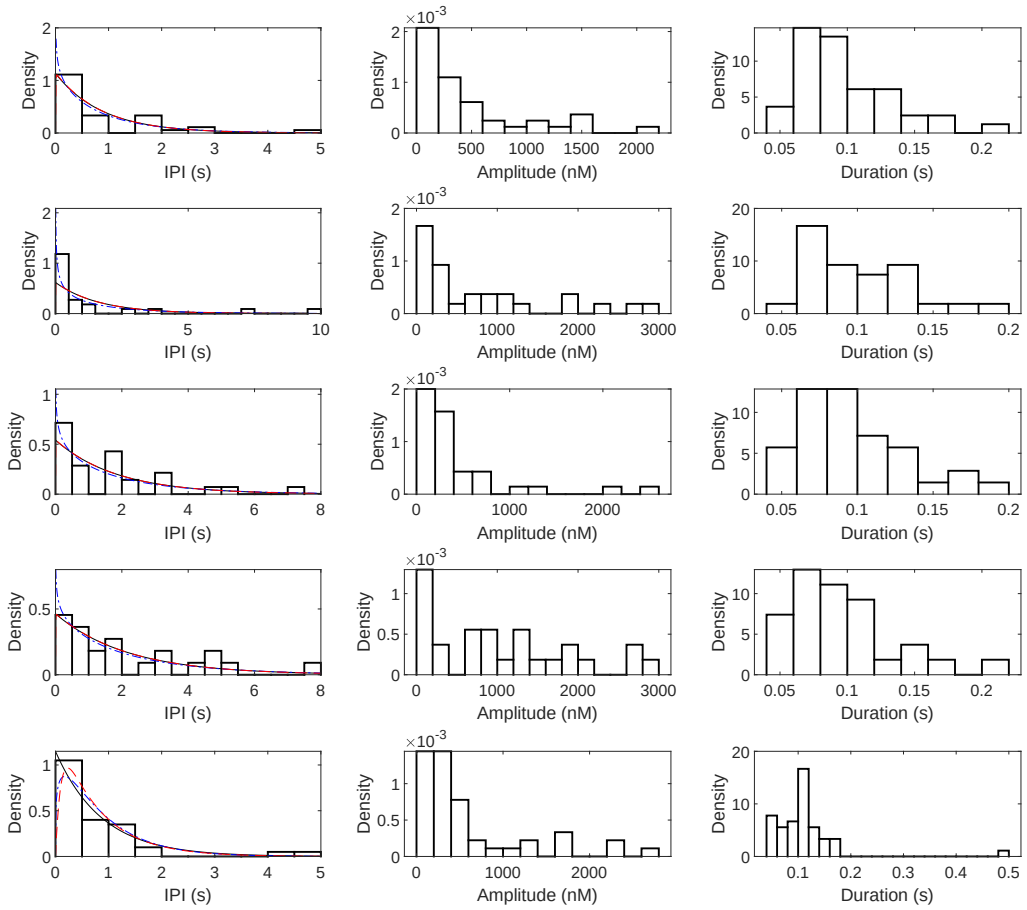

Figure 2.13: Ca^{2+} puff statistics for wild-type 1 IPR. Data sets 6-10. The plots show the Exponential distribution as a solid black line, the Gamma distribution as a dot-dashed blue line, and the Time-Dependent distribution as a red-dashed line.

Table 2.6: Wild-type 1 IPR Ca^{2+} puff summary statistics

Exo 76 wild-type 1 IPR summary statistics						
Interpuff interval (s)						
	Min.	1st Qu.	Median	Mean	3rd Qu.	Max.
1	0.02	0.36	0.76	1.12	1.61	5.02
2	0.02	0.28	0.46	1.13	1.67	4.58
3	0.02	0.28	0.59	1.19	1.90	5.96
4	0.02	0.42	1.04	1.15	1.62	4.02
5	0.02	0.31	0.56	1.27	1.62	10.06
6	0.02	0.28	0.4	0.88	1.50	4.86
7	0.02	0.28	0.44	1.62	1.28	9.80
8	0.02	0.37	1.58	1.85	2.42	7.42
9	0.02	0.56	1.37	2.16	3.44	7.92
10	0.02	0.30	0.55	0.87	1.04	4.52
Ca^{2+} puff amplitude (nM)						
	Min.	1st Qu.	Median	Mean	3rd Qu.	Max.
1	84.85	236.87	507.15	648.78	829.52	2227.16
2	36.46	128.06	267.17	816.97	1109.99	6020.77
3	37.33	186.82	468.55	850.60	1151.57	3680.11
4	49.77	132.31	288.32	510.53	748.78	1970.19
5	64.98	165.07	613.81	1223.65	1085.34	10668.57
6	33.06	104.15	228.84	456.60	549.36	2107.56
7	58.77	120.47	312.87	779.80	1056.13	2932.99
8	14.77	124.41	257.46	430.40	432.73	2489.80
9	61.68	189.04	923.71	1068.24	1740.99	2834.78
10	43.95	164.96	308.15	604.01	691.46	2656.14
Ca^{2+} puff duration (s)						
	Min.	1st Qu.	Median	Mean	3rd Qu.	Max.
1	0.04	0.06	0.08	0.08	0.1	0.18
2	0.04	0.06	0.08	0.09	0.12	0.26
3	0.04	0.06	0.08	0.08	0.1	0.16
4	0.02	0.06	0.08	0.08	0.1	0.2
5	0.04	0.06	0.08	0.1	0.12	0.26
6	0.04	0.06	0.08	0.09	0.11	0.22
7	0.04	0.06	0.08	0.09	0.12	0.18
8	0.04	0.06	0.08	0.09	0.1	0.18
9	0.04	0.06	0.08	0.09	0.1	0.22
10	0.04	0.06	0.1	0.1	0.12	0.48

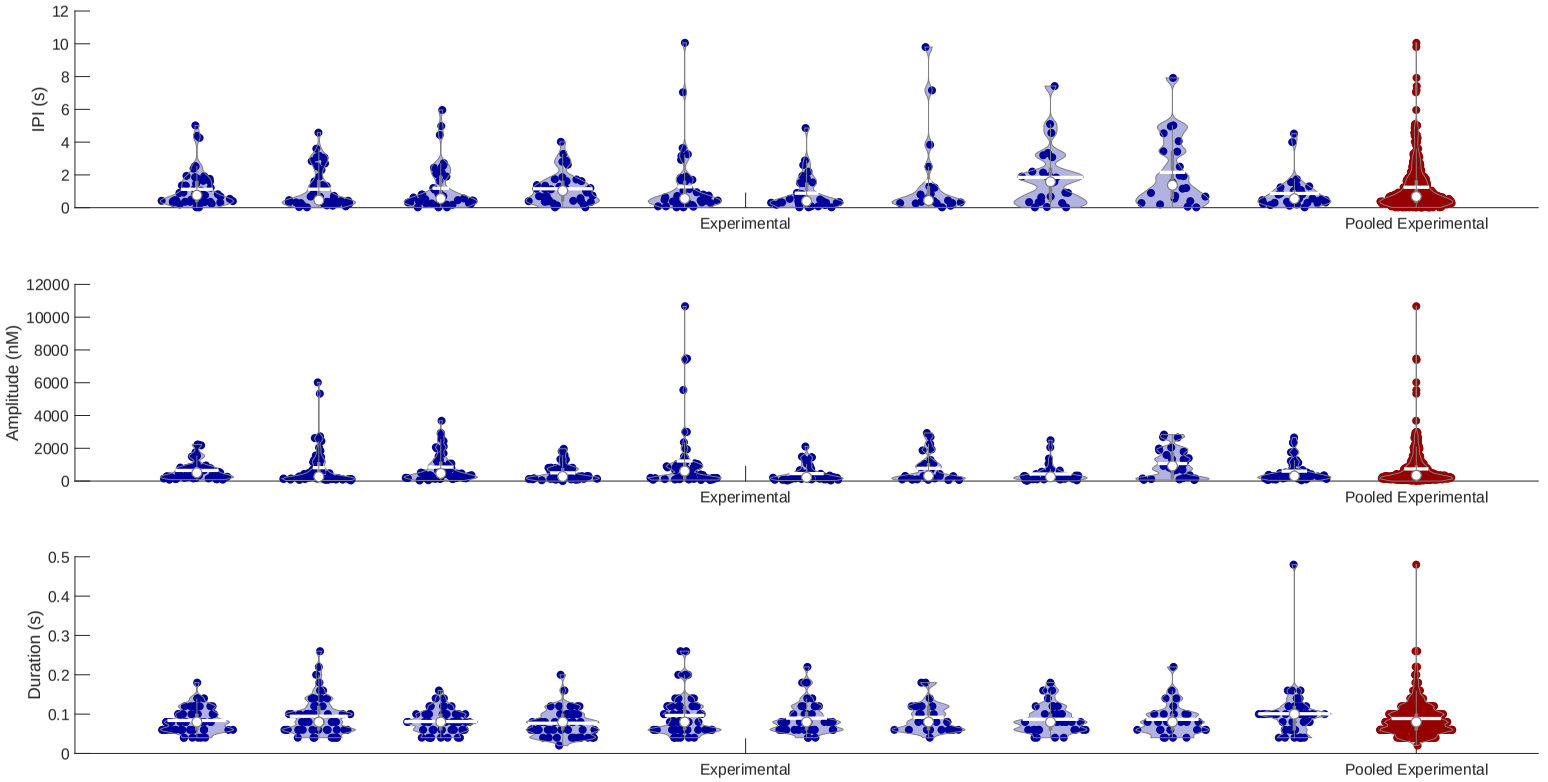

Figure 2.14: Violin plots of Ca^{2+} puff statistics from wild-type 1 IPR

We parameterised the Exponential, Gamma and Time-Dependent distributions using IPI data from wild-type 1 IPR. Parameter results are presented in Table 2.3.2. All ξ values are much greater than λ for the Time-Dependent distribution, which results in a distribution that is similar to the Exponential distribution. Three of the Gamma distributions have α and β values greater than 1. This creates a distribution that suggests a refractory period. The remaining Gamma distributions have α values close to 1, creating the appearance of an Exponential distribution. The Exponential distribution can account for the steep decay present in the IPI distributions. We pooled the experimental data from each group and estimated the parameters for each statistical distribution. The large ξ parameter, again, emphasises the pooled data forms an Exponential distribution. The pooled data and statistical distributions are presented in Fig A.1.

Table 2.7: Parameter estimates for interpuff interval distributions from wild-type 1 IPR

	Exponential	Gamma		Time-Dependent	
	λ	α	β	λ	ξ
1	0.8899	1.1427	1.0168	0.8948	159.9999
2	0.8865	0.9366	0.8302	0.8946	97.2116
3	0.8420	0.8587	0.7231	0.8453	221.911
4	0.8665	1.2502	1.0834	0.8702	193.6261
5	0.7869	0.7443	0.5857	0.7900	192.1179
6	1.1327	0.8349	0.9457	1.1388	211.9104
7	0.6177	0.6352	0.3924	0.6195	222.4789
8	0.5411	0.8124	0.4396	0.5422	268.045
9	0.4635	0.8534	0.3956	0.4645	234.1589
10	1.1494	1.2475	1.4339	1.2925	9.7665
Pooled	0.8015	0.8749	0.7013	0.8049	196.4999

Table 2.8 presents the AIC, BIC and WAIC values for each statistical

distribution. All values are very similar. Most information criteria are the smallest for the Exponential distribution. The Gamma and Time-Dependent distribution have the lowest information criteria for 9 of the results, inclusively. Our results suggest there is no refractory period following a Ca^{2+} puff from wild-type 1 IPR. This is evidenced by the Exponential distribution fitting the IPI distributions the best.

We calculated the AIC, BIC and WAIC values for each statistical distribution parameterised using the pooled experimental data. Interestingly, only the BIC value was smallest for the Exponential distribution, with the AIC and WAIC values being smallest for the Gamma distribution.

We conducted a Kolmogorov Smirnov test for each wild-type 1 IPR IPI data set to determine at the 95% confidence level if the data comes from an Exponential, Gamma, or Time-Dependent distribution. Our p-values and test statistics are presented in Table 2.3.2. At the 5% significance level, we fail to reject H_0 for all three distributions for seven data sets. H_0 is rejected at the 5% significance level for the Exponential distribution for three data sets (data set 6,8 and 9). The Gamma distribution has the smallest test statistic for seven IPI data sets. We perform the Kolmogorov Smirnov test for the pooled wild-type 1 IPR IPI data. We reject H_0 at the 5% significance level for all statistical distributions. In Fig 2.15 - 2.16, we present the empirical CDF and model CDFs for each wild-type 1 IPR IPI data set. Results for the pooled data can be seen in Fig A.3.

E2002D-type 1 IPR Fig 2.17 presents histograms of Ca^{2+} puffs from pooled E2002D-type 1 IPR experimental data. Due to the low frequency of Ca^{2+} events, we are unable to compare the distributions of each experimental

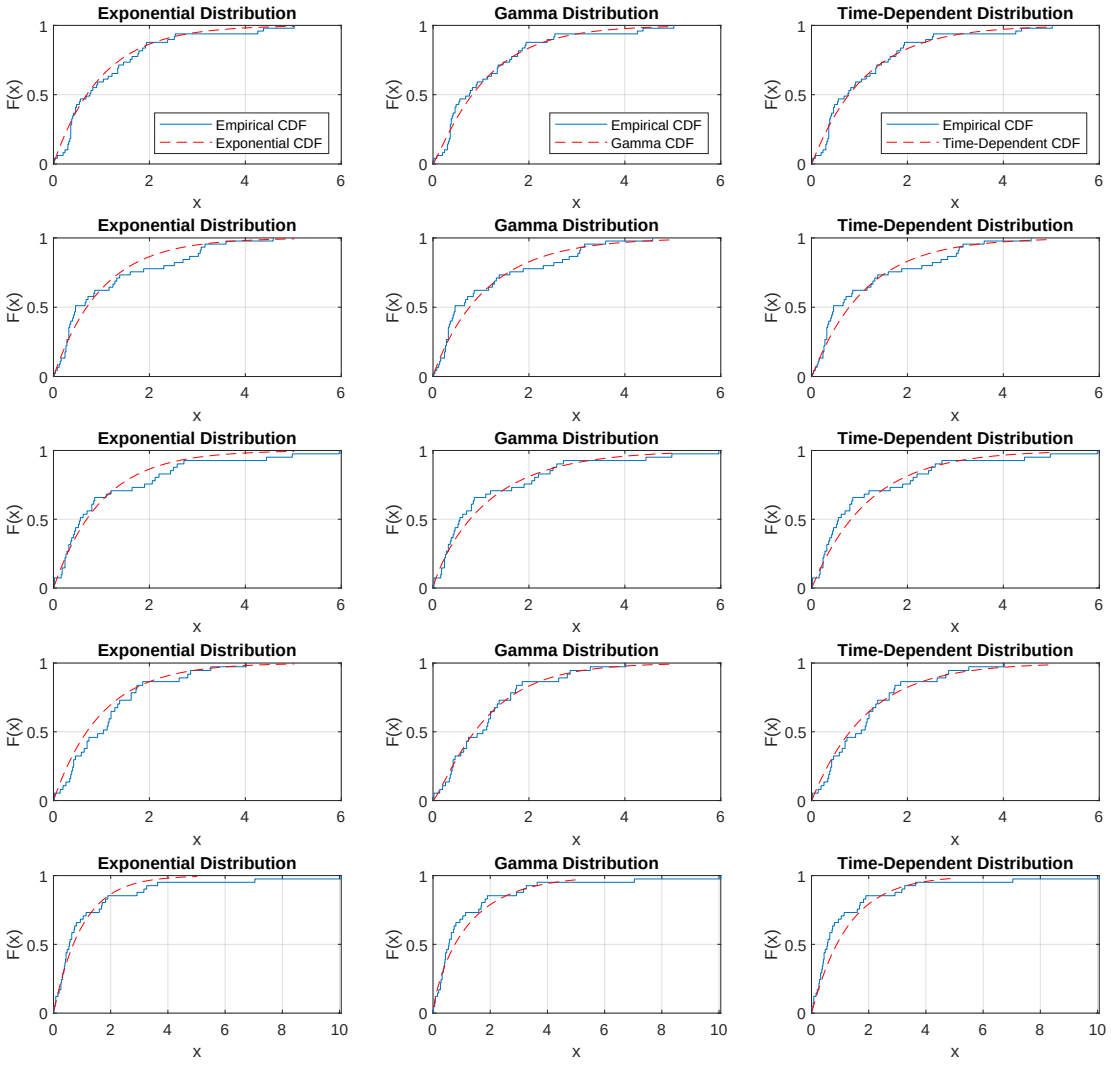

Figure 2.15: Comparison of Exponential, Gamma and Time-Dependent cumulative density function with the empirical cumulative distribution function of the IPI sample from the wild-type 1 IPR IPI data (data sets 1 - 5).

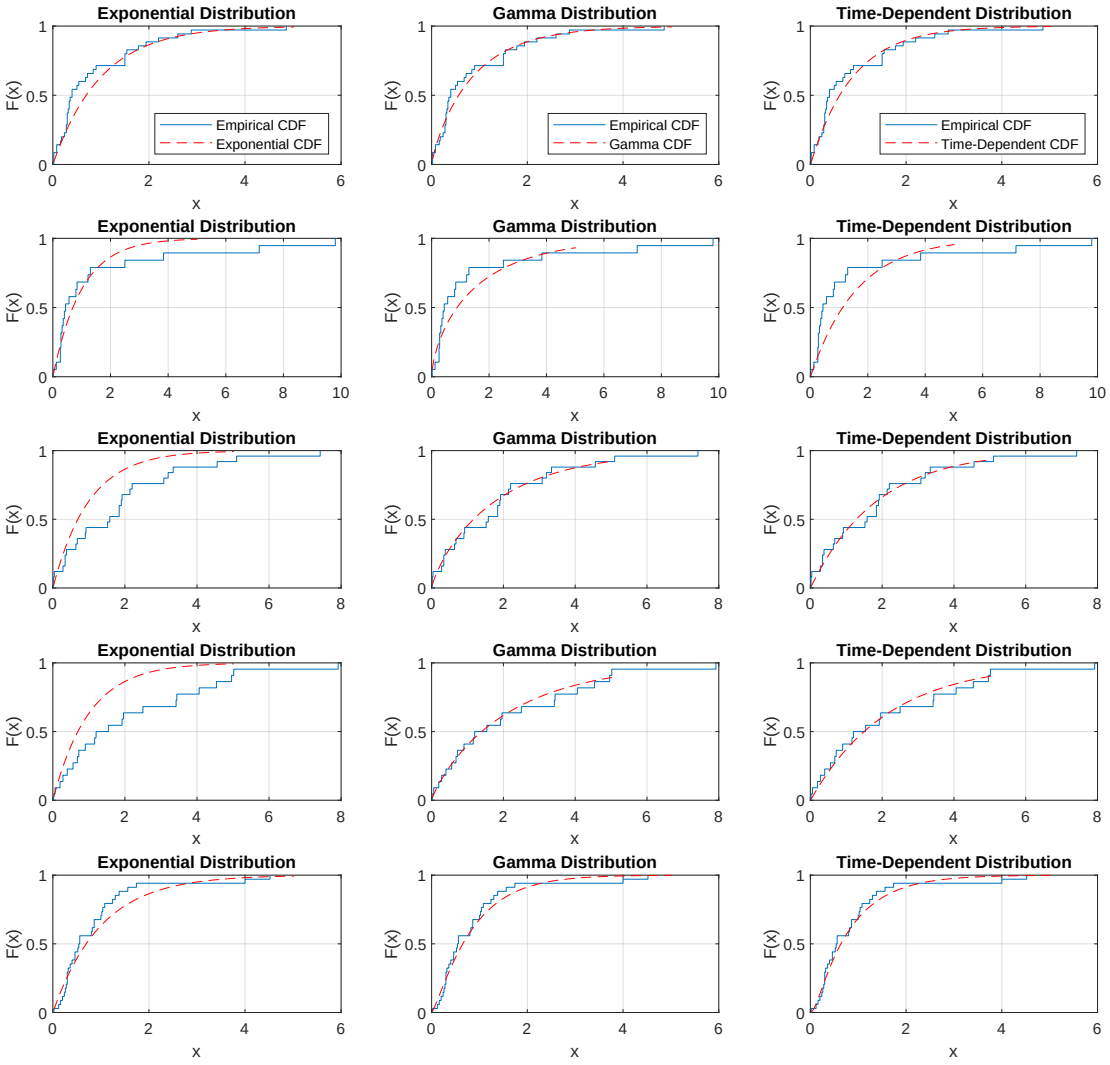

Figure 2.16: Comparison of Exponential, Gamma and Time-Dependent cumulative density function with the empirical cumulative distribution function of the IPI sample from the wild-type 1 IPR IPI data (data sets 6 - 10).

Table 2.8: Information criteria for wild-type 1 IPR

	Exponential			Gamma			Time-Dependent		
	AIC	BIC	WAIC	AIC	BIC	WAIC	AIC	BIC	WAIC
1	**111.81**	**113.74**	**111.41**	112.89	116.68	113.43	113.05	116.83	111.43
2	**102.84**	**104.65**	**103**	104.71	108.32	104.62	104.37	107.98	103.12
3	**100.44**	**102.18**	**100.78**	101.77	105.24	101.88	102.20	105.67	**100.78**
4	**86.60**	**88.21**	86.33	87.52	90.75	87.99	88.36	91.58	**86.31**
5	**103.65**	**105.36**	105.14	103	106.42	**104.09**	105.4	108.82	105.08
6	**63.28**	**64.83**	**63.63**	64.48	67.59	64.74	64.99	68.10	63.66
7	58.31	59.25	60.55	**57.18**	**59.07**	**58.16**	60.23	62.11	60.53
8	**82.71**	**83.92**	**82.74**	83.94	86.38	84.20	84.62	87.06	82.80
9	**79.83**	**80.92**	79.92	81.45	83.63	81.67	81.76	83.94	**79.88**
10	**60.53**	**62.06**	60.96	61.56	64.61	62.63	60.64	63.69	**60.89**
Pooled	854.39	**858.25**	854.75	**852.13**	859.83	**852.27**	854.26	861.97	854.44

group. Despite the infrequent events, Fig 2.17 demonstrates that Ca^{2+} puffs occur within a close time frame when triggered. This is evident through the high frequency of shorter IPIs. The amplitude and duration distributions are skewed to the right with a higher frequency of short amplitudes and durations. Summary statistics of the Ca^{2+} puffs are presented in Table 2.10.

In Fig 2.18 we present violin plots of the Ca^{2+} puff statistics. The low frequency of Ca^{2+} puff events is evident in these plots. As shown in Fig 2.17, the IPI distribution has a higher density for shorter IPIs, amplitudes and durations.

We parameterise the Exponential, Gamma and Time-Dependent distributions using the pooled IPI data. Parameter results are shown in Table 2.11. Both the Gamma and Time-Dependent distributions appear to follow an Exponential distribution. A low α and β value as shown in Fig 2.17 emphasises the high frequency of smaller IPIs. Furthermore, a high ξ value indicates the Time-Dependent distribution can be reduced to the Exponential distribution (Thurley et al., 2011).

Table 2.9: Kolmogorov-Smirnov Test: p-value and test statistics for wild-type 1 IPR IPI distributions

		Exponential	Gamma	Time-Dependent
1	P-value	0.0631	0.5812	0.3568
	Test statistic	0.1841	0.1079	0.1291
2	P-value	0.2550	0.1647	0.0957
	Test statistic	0.1475	0.1628	0.1799
3	P-value	0.1993	0.5190	0.3327
	Test statistic	0.1636	0.1235	0.1438
4	P-value	0.0607	0.8805	0.6425
	Test statistic	0.2124	0.0925	0.1176
5	P-value	0.3862	0.3137	0.0800
	Test statistic	0.1374	0.1462	0.1938
6	P-value	0.0243	0.4307	0.1811
	Test statistic	0.2453	0.1431	0.1804
7	P-value	0.1963	0.3956	0.0659
	Test statistic	0.2383	0.1977	0.2899
8	P-value	$2.6842e^{-06}$	0.6382	0.8193
	Test statistic	0.4997	0.1426	0.1208
9	P-value	$8.2354e^{-06}$	0.9255	0.9090
	Test statistic	0.5090	0.1102	0.1136
10	P-value	0.1723	0.6915	0.7453
	Test statistic	0.1849	0.1176	0.1120
Pooled	P-value	$4.1802e^{-06}$	0.0115	$1.5955e^{-14}$
	Test statistic	0.1363	0.0856	0.1158

Table 2.10: E2002D-type 1 IPR Ca^{2+} puff summary statistics

E2002D-type 1 IPR summary statistics					
Interpuff interval (s)					
Min.	1st Qu.	Median	Mean	3rd Qu.	Max.
0.20	0.41	1.80	1.93	3.24	5.44
Ca^{2+} puff amplitude (nM)					
Min.	1st Qu.	Median	Mean	3rd Qu.	Max.
61.69	248.99	624.42	655.58	987.55	1908.57
Ca^{2+} puff duration (s)					
Min.	1st Qu.	Median	Mean	3rd Qu.	Max.
0.04	0.045	0.06	0.07	0.08	0.16

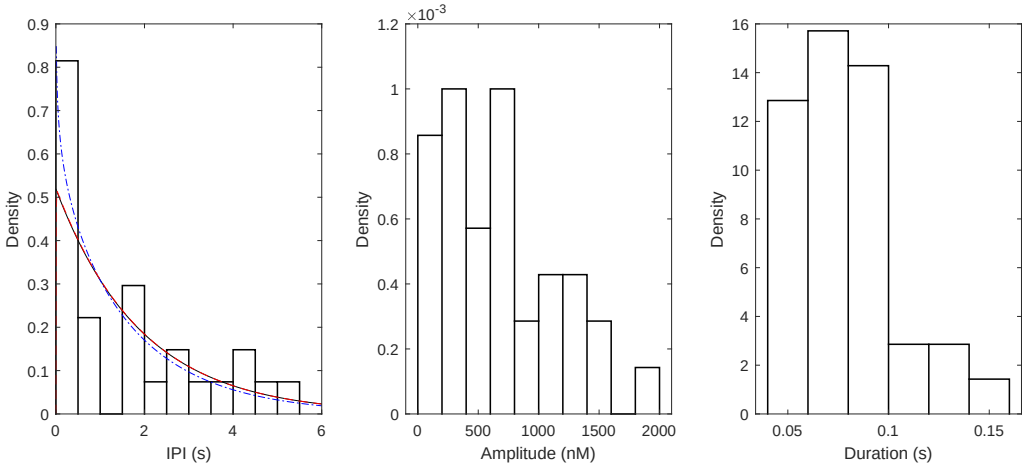

Figure 2.17: Ca^{2+} puff statistics from E2002D-type 1 IPR

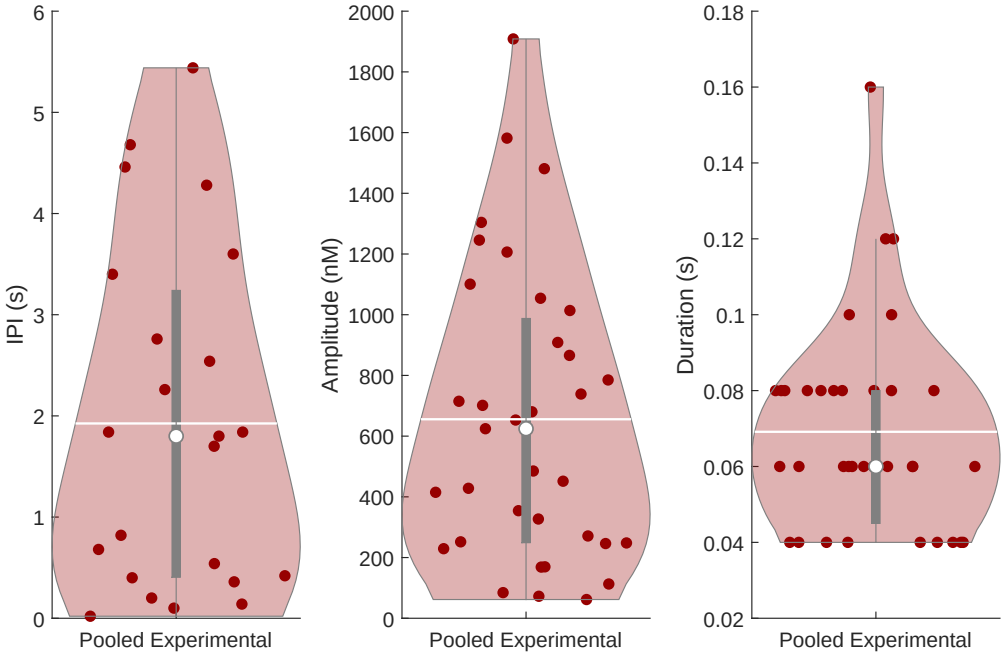

Figure 2.18: Violin plots of pooled Ca^{2+} puff statistics from E2002D-type 1 IPR

Table 2.11: Parameter estimates for the pooled interpuff interval distribution from E2002D-type 1 IPR

	Exponential	Gamma		Time-Dependent	
	λ	α	β	λ	ξ
Pooled	0.5194	0.8924	0.4637	0.5207	220.2454

Table 2.12: Information Criterion for E2002D-type 1 IPR

	Exponential			Gamma			Time-Dependent		
	AIC	BIC	WAIC	AIC	BIC	WAIC	AIC	BIC	WAIC
Pooled Data	**78.13**	**79.27**	**77.96**	79.93	82.20	80.10	80.05	82.32	78.13

In Table 2.12 we compare the AIC, BIC and WAIC results for our three parameterised statistical distributions. Unanimously, the smallest information criteria value is for the Exponential distribution.

We conducted a Kolmogorov Smirnov test to determine at the 95% confidence level if the pooled E2002D-type 1 IPR IPI data comes from an Exponential, Gamma, or Time-Dependent distribution. Our p-values are presented in Table 2.13. At the 5% significance level, we reject H_0 for the Exponential distribution and fail to reject H_0 for the Gamma and Time-Dependent distribution. In Fig 2.19, we present the empirical CDF and compare our results with model CDFs. Our results show that the difference between the empirical CDF and the Exponential CDF is the largest. This is confirmed by the Kolmogorov Smirnov test statistic, presented in Table 2.13.

Table 2.13: Kolmogorov-Smirnov Test: p-value and test statistic for the pooled E2002D-type 1 IPR IPI distribution.

	Exponential	Gamma	Time-Dependent
P-value	$2.3270e^{-05}$	0.2713	0.1492
Test statistic	0.4436	0.1862	0.2129

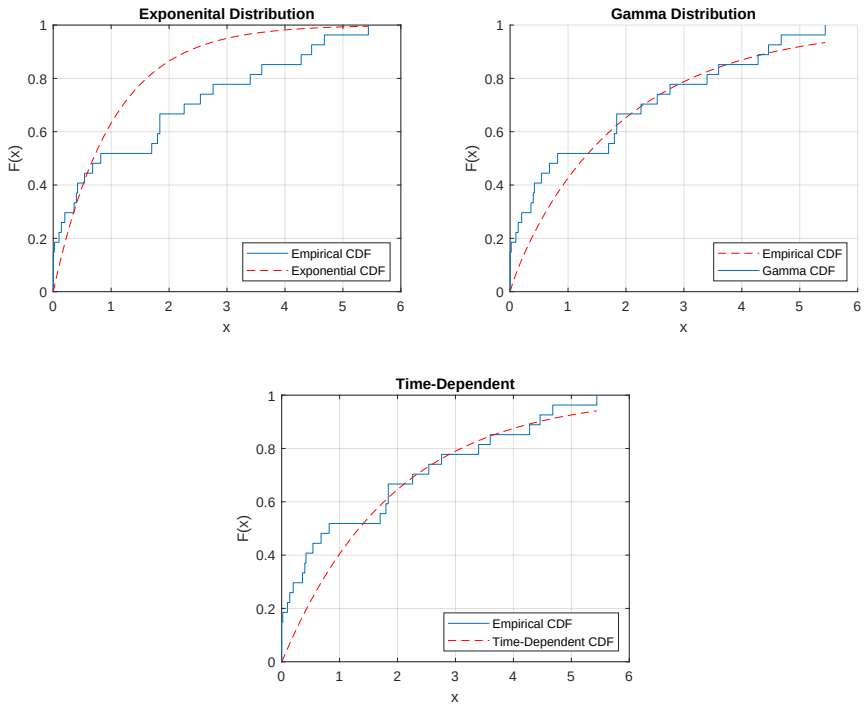

Figure 2.19: Comparison of Exponential, Gamma and Time-Dependent cumulative density function with the empirical cumulative distribution function from the pooled E2002D-type 1 IPR IPI data.

2.4 Chapter discussion

Experimental Ca^{2+} puff statistics help to provide an in-depth understanding of Ca^{2+} and IP_3R dynamics. Using statistical distributions to model the IPI distribution provides the advantage of being able to compare results from different experimental data groups and understand how changes to the IP_3R effect Ca^{2+} dynamics (Cao et al., 2013, 2017). In this chapter, we used the Exponential, Gamma and Time-Dependent distributions to explore the question: do IPIs from exo 76 wild-type 1 IPR, wild-type 1 IPR and E2002D-type 1 IPR (Arige et al., 2022) exhibit refractoriness? The investigation into this question informs us of the behaviour of IP_3Rs and how they respond to change in Ca^{2+} concentrations. Our results demonstrate a refractory period is evident in the exo 76 wild-type 1 IPR data sets. This is demonstrated by the peak of the IPI distribution not being close to 0, as seen within an Exponential distribution, demonstrating the IP_3R recovers slowly from Ca^{2+} inhibition (Cao et al., 2013). IPI distributions calculated from the wild-type 1 IPR Ca^{2+} puff statistics are exponentially distributed. This indicated a fast recovery from Ca^{2+} inhibition. However, there are indications of a refractory period in the pooled wild-type 1 IPR data set. This suggests that, with our current data set size, we are at the limit of determining if this is truly the case. In Chapter 3 and 4, we develop a mathematical model that is parameterised using wild-type 1 IPR and E2002D-type 1 IPR data. Our model will allow us to observe the behaviour of IPIs over longer simulation periods than those achievable through experimentation

2.4.1 Single channel data

We compared the single channel data from wild-type 1 IPR and wild-type 1 IPR that have had a substitution at the 2002 glutamic acid residue to aspartic acid (E2002D-type 1 IPR)(Arige et al., 2022). We did not have access to stationary single channel data from exo 76 wild-type 1 IPR which are also discussed within this chapter.

Substitution at the 2002 glutamic acid residue to aspartic acid causes the open probability of the IP_3R, shown in Fig 2.6, to reduce to ~ 0.45 from 0.7 (Arige et al., 2022). The time spent in a closed state increases due to this substitution, therefore impacting the frequency of Ca^{2+} puffs.

2.4.2 Comparison of Ca^{2+} puff statistics

Within this chapter, we compared the Ca^{2+} statistics from exo 76 wild-type 1 IPR, wild-type 1 IPR and E2002D-type 1 IPR experimental data. Ca^{2+} puff data is extremely informative, providing us with an insight into how healthy IP_3Rs work within different cells and how changes to these IP_3R affect the Ca^{2+} signalling system. The exo 76 wild-type 1 IPR produces IPIs that are slightly longer in comparison to wild-type 1 IPR and E2002D-type 1 IPR IPIs. Amplitude and duration results are similar to those produced by wild-type 1 IPR.

Comparison of Ca^{2+} puffs from wild-type 1 IPR and E2002D-type 1 IPR, presented in Fig 2.12-2.13 and Fig 2.17, demonstrate that the substitution at the 2002 glutamic acid residue to aspartic acid causes the channel to be less active. Data from E2002D-type 1 IPR had to be pooled to ensure a meaningful statistical analysis could be conducted. Whilst the number of

Ca^{2+} puffs is extremely reduced, this does not appear to affect the IPI time, i.e when a Ca^{2+} puff occurs, the time until the next Ca^{2+} puff is similar to the wild-type 1 IPR data.

Ca^{2+} puff amplitude distributions from both wild-type 1 IPR and pooled E2002D-type 1 IPR were right-skewed, evidencing that most Ca^{2+} puffs occur from a small number of IP_3R opening. The average puff amplitude for the pooled E2002D-type 1 IPR data is similar to the wild-type 1 IPR data. However, the maximum amplitude is much smaller than that of the wild-type 1 IPR cell. This suggests that the substitution of the 2002 glutamic acid residue to aspartic acid may affect the number of IP_3R opening during a Ca^{2+} puff. Statistics for the wild-type 1 IPR and pooled E2002D-type 1 IPR durations are similar, suggesting that puff durations are not affected by the substitution at the 2002 glutamic acid residue.

2.4.3 Probability distributions to model IPI distributions

We parameterised the Exponential, Gamma and Time-Dependent distributions using IPI data from the three IP_3R. Whilst all IPI distributions for the wild-type 1 IPR and E2002D-type 1 IPR data appear to be exponentially distributed, some distributions from the exo 76 wild-type IPR data have a lower frequency of short IPIs (see Fig 2.9). Therefore, their distributions are akin to a Gamma or Time-Dependent distribution. Thurley and Falcke (2011); Cao et al. (2013) state this shaped IPI distribution demonstrates the IP_3R is subject to refractoriness. Within our study, the Exponential distribution is not able to describe the true shape of the exo 76 wild-type 1 IPR

IPI distributions. We estimated both the λ and ξ parameters of the Time-Dependent distribution. In contrast, Thurley et al. (2011); Cao et al. (2017) found good fits to experimental data from human neuroblastoma SH-SY5Y and human embryonic kidney cells when λ was fixed as the reciprocal of the mean IPI and ξ was estimated using a non-linear fitting. We find the estimate of λ is similar for both the Exponential and Time-Dependent distribution. The ξ estimates are greater than the λ estimate for all experimental groups. Thurley et al. (2011) state the Time-Dependent distribution can therefore be reduced to an Exponential distribution. However, whilst $\xi >> \lambda$ for all of our Time-Dependent distributions, if we reduced it to the Exponential distribution we would not describe the gradual rise seen in some of the distributions. Wild-type 1 IPR and E2002D-type 1 IPR IPI distributions evidence a fast recovery rate from Ca^{2+} inhibition. IPI distributions with a refractory period have been shown in the analysis of Yao et al. (1995); Fraiman et al. (2006); Thurley et al. (2011); Cao et al. (2013). Comparison of each statistical distribution for the exo 76 wild-type 1 IPR IPI data in Fig 2.9 shows the Exponential distribution does not capture the shorter events that evidence a refractory period. The Gamma and Time-Dependent distributions estimate this data better. The Exponential distribution fits the wild-type 1 IPR and E2002D-type 1 IPR IPI distributions well, see Fig 2.12-2.13 and Fig 2.17.

2.4.4 Statistically comparing distributions using information criteria

Information criteria were used to compare the fit of statistical distributions to the IPI data sets. The Exponential distribution has the largest AIC and

WAIC values for all exo 76 wild-type 1 IPR data sets, suggesting this distribution is the worst-fitting model. Three of the lowest BIC values were for the Exponential distribution. However, this could be due to BIC favouring simpler models i.e. where there are fewer parameters. The Gamma distribution has the lowest AIC and WAIC value for two of four data sets and qualitatively fits the IPI distributions well. Similarly, the Time-Dependent distribution has the lowest AIC and WAIC values for the remaining two data sets. The majority of the smallest information criterion for the wild-type 1 IPR and E2002D-type 1 IPR data were for the Exponential distribution. A difficulty found in our analysis is that different minima were obtained for the information criteria when applied to various distributions. This suggests there is not a distinct statistical distribution to represent the IPI distributions. A cause for this may be due to the limited data set sizes. To overcome this issue, we calculated the AIC, BIC and WAIC values for the pooled data. For the pooled exo 76 wild-type 1 IPR IPI data, all information criteria were the smallest for the Gamma distribution. BIC was the smallest for the Exponential distribution for the pooled wild-type 1 IPR IPI data and AIC and WAIC smallest for the Gamma distribution. If we were to choose a distribution as standard across all data sets, the Exponential distribution would not be suitable because it cannot describe the refractory period often seen in some of the IPI distributions. The benefit of using the Time-Dependent distribution is being able to directly relate the parameters of the distribution to dynamics of the IP_3R. When considering the interpretation of the Gamma parameters in relation to the IPI dynamics, an α value close to 1 implies fast recovery from Ca^{2+} inhibition - the distribution transitions to the

Exponential distribution. An α value greater than 1 indicates the presence of a refractory phase.

2.4.5 Using the Kolmogorov-Smirnov goodness of fit test to compare IPI distributions with model probability distributions

We used the Kolmogorov-Smirnov goodness of fit test to compare the IPI distributions from the exo 76 wild-type 1 IPR, wild-type 1 IPR and E2002D-type 1 IPR IPI distributions with the Exponential, Gamma and Time-Dependent distributions. We rejected the null hypothesis at the 5% level of significance for the Exponential distribution for all exo 76 wild-type 1 IPR IPI distributions, three wild-type 1 IPR IPI distributions and the pooled E2002D-type 1 IPR IPI distribution. This emphasises the Exponential distribution may not produce accurate predictions of the IP_3R behaviour. With the exception of the pooled wild-type 1 IPR IPI distribution, we do not reject the null hypothesis for any IPI data sets for the Gamma and Time-Dependent distributions. Our results demonstrate most IPI distributions present within this chapter come from the Gamma or Time-Dependent distribution. Whilst this is the first time, to our knowledge, such statistical tests have been applied to IPI distributions, it is not the first time for Ca^{2+} modelling. Tilūnaitė et al. (2017) used the Kolmogorov-Smirnov test to determine which probability distribution most accurately describes inter-spike intervals from HEK293T cells. In contrast to our analysis, Tilūnaitė et al. (2017) plotted the empirical and model CDF against each other - an identical distribution is shown by the plot exhibiting a straight line. Their results demonstrated the inhomo-

geneous Gamma distribution plotted against their empirical CDF produced the closest linear fit. They suggest the shape parameter within the inhomogeneous Gamma distribution allows for more flexibility. This is evident within our results for the Gamma and Time-Dependent distributions; α and ξ enable the statistical distributions to fit IPI distributions with fast and slow rates. Taking into consideration the qualitative and quantitative analysis conducted within the chapter, we conclude that the Gamma distribution best represents the IPI distributions in each data set.

The wild-type 1 IPR and E2002D-type 1 IPR data analysed within this chapter was obtained from experimentalists who are the first to substitute the 2002 glutamic acid residue with aspartic acid (Arige et al., 2022). Mathematical models of the Ca^{2+} signalling system parameterised using the data presented in this chapter may be able to help us understand what biological changes within the IP_3R cause the different dynamics. For example, the analysis of the single channel data will later be used to parameterise a Markov model. Comparison of the open probability curves generated by the model and the parameter estimates will allow us to understand which mechanisms within the IP_3R are influenced by the change in the amino acid chain. Additionally, mathematical models constructed from experimental data have the benefit of displaying IP_3R and Ca^{2+} dynamics over a longer duration than can be observed under experimental conditions. By analysing the experimental data statistically, we can compare key Ca^{2+} puff metrics with our model results to ensure agreement.

This chapter aimed to firstly, analyse stationary single channel and Ca^{2+} puff data from exo 76 wild-type 1 IPR, wild-type 1 IPR and E2002D-type

1 IPR. Secondly, we compared the fitting of three statistical distributions to IPI data both qualitatively and quantitatively. Our results, like those by Yao et al. (1995); Fraiman et al. (2006); Thurley et al. (2011); Cao et al. (2013), demonstrate there is often large variability within Ca^{2+} puff statistics from the same IP_3R type. Whilst some IPI distributions were exponentially distributed, showing fast recovery from Ca^{2+} inhibition, others were non-exponentially distributed, evidencing a refractory period. Thurley et al. (2012), who found variability within their analysis of IPIs from HEK-293 and SH-SY5Y cells, note that heterogeneity does not impact Ca^{2+} signals from transmitting information. Therefore, by comparing multiple data sets from the same IP_3R we can gain a broader overview of the IP_3R dynamics and pooling the data enables us to understand the workings of the IP_3R on a larger scale.

3 Mathematical modelling of Ca^{2+} puffs

3.1 Background

Nobel prize winners in physiology and medicine, Hodgkin and Huxley, produced a series of papers, concluding with Hodgkin and Huxley (1952), describing mathematical models for the flow of electrical current through the surface membrane of giant nerve fibre of the squid giant axon (Hodgkin and Huxley, 1952; Brady, 1972; Rameh et al., 2020). Their model comprises of four ordinary differential equations (ODEs), one to describe the flow of electrical current and the remaining to describe the ionic conductance of various ions, namely sodium and potassium. The methods described by Hodgkin and Huxley (1952) have helped to develop models of the behaviour of different ion channel dynamics (Li and Rinzel, 1994; Dangerfield et al., 2012; Dupont et al., 2016; Bressloff and Maclaurin, 2018). A perhaps controversial review by Meunier and Segev (2002) questions how useful the Hodgkin-Huxley model is in comparison to other methods. They state researchers rarely use the Hodgkin-Huxley equations on their own, instead opting for Hodgkin-Huxley-like equations. However, Meunier and Segev (2002) conclude the Hodgkin - Huxley equations have helped advance many applications. The methodology by Hodgkin and Huxley has helped support the development

of models that simulate the opening and closing of the IP_3R and thus, the Ca^{2+} signalling system (Ullah et al., 2012a; Cao et al., 2013). Cao et al. (2013) used the Hodgkin-Huxley-like equations to integrate data by Mak et al. (2007) into the Siekmann model (Siekmann et al., 2012) and succeeded in simulating realistic puff and dwell time distributions. The introduction of Hodgkin-Huxley-like equations into the Siekmann model increases the number of ODES to forty. This high number of ODEs is due to the model simulating a cluster of ten ion channels, where for each ion channel there are four gating variables.

Attempts have been made to condense the four ODEs by Hodgkin and Huxley (1952) into integrodifferential equations and a single delay differential equation (Brady, 1972; Rameh et al., 2020). Brady (1972) shows a single integrodifferential equation can produce the same solution as the ODEs used to calculate the gating variables in the Hodgkin-Huxley model. Although, Brady (1972) state that their method does not simplify the model, it could be advantageous when dealing with a model with a high number of differential equations, such as the model by Cao et al. (2013). Rameh et al. (2020) proposed models based on a single delayed differential equation (DDE) that can produce action potentials similar to those from the original Hodgkin-Huxley and FitzHugh-Nagumo models. Like Brady (1972), Rameh et al. (2020) firstly write a system of ODEs as a single integrodifferential equation. They then turn their integrodifferential equation into a DDE. Their integrodifferential equation was an exact match to the FitzHugh-Nagumo model, however, their DDE produced some differences such as a shorter hyperpolarization. Qualitatively, their DDE and integrodifferential models produced

similar results to the original Hodgkin-Huxley model.

3.1.1 Time delays within experimental data

Biological phenomena often have time delays, for example, the stages of the life cycle, the time between the start of a cell infection and the production of a new virus to the dynamics of several interacting species and the intracellular Ca^{2+} release by IP_3R is no different (Cushing, 1977; Rihan, 2021).

Payne et al. (1990) compared the effect three temperatures (8°C, 14°C and 20°C) and injections of IP_3 and Ca^{2+} into limulus ventral photoreceptors have on the concentration of intracellular Ca^{2+} ions. Their results show the elevation of Ca^{2+} before an injection of IP_3 temporarily inhibits the ability of IP_3R to release Ca^{2+} and the recovery from this inhibition is slowed by a lower temperature. Payne et al. (1990) suggest that feedback inhibition plays a role in producing the intracellular concentration of Ca^{2+} ions. This demonstrates the possibility of a link between the binding of IP_3 to an inhibitory site and the delay in the channel releasing Ca^{2+} and opening.

Carter and Ogden (1992) investigated the intracellular Ca^{2+} ion channel release by IP_3 in vascular endothelial cells using the patch-clamp method. Through their experiment, they found the delay in Ca^{2+} fluorescence response was changed under different concentrations of IP_3. For low concentrations of IP_3, the delay averaged at 300 ms, whereas for high concentrations of IP_3, the delay time was much shorter (>20ms). These results were noted to be consistent with a direct binding and gating action of IP_3 on the Ca^{2+} channel of the cellular store and suggested there is a direct coupling between IP_3 binding and an increase in the open probability of the Ca^{2+} release channels.

Using a new patch clamp configuration, Mak et al. (2007) analysed the kinetic responses of single IP_3R channels in native ER membrane when ligand concentrations were abruptly changed. Mak et al. (2007) define the activation and deactivation latency as:

"Activation latency is the duration between the solution switch time and the first observed channel opening event in response to the solution switch. Deactivation latency is the duration between solution switch time and the last observed channel closing."

Therefore, we can define latency as the time it takes for the channel to first open or first close. When keeping the Ca^{2+} concentration constant, Mak et al. (2007) saw large latency when IP_3 was switched from 0 to 10 µM and 0 to 100µM. They note that this suggests IP_3 binding and subsequent conformational changes required for the channel opening both contribute to the total activation latency. Furthermore, Mak et al. (2007) analysed the latency when the IP_3 concentration was constant and there was a step change in Ca^{2+} concentration. They saw a latency an order of magnitude higher than that of the IP_3 activation latency when the Ca^{2+} concentration was increased from <0.01µM to 2µM. A short latency was seen when the Ca^{2+} concentration jumped from 2µM to 300µM. This again, showed Ca^{2+} binding and subsequent conformation changes contribute to the Ca^{2+} activation latency. The activation and deactivation latency distributions often showed a deficit in small latencies. Cao et al. (2013); Ullah et al. (2012a); Bicknell and Goodhill (2016) compare their latency distributions from their Markov models to the experimental data by Mak et al. (2007).

In this chapter, we build a hybrid stochastic system based on integrodif-

ferential equations that produce Ca^{2+} puffs comparable with those simulated by more complex Ca^{2+} signalling models (Siekmann et al., 2012; Cao et al., 2013, 2014). The introduction of integral terms within the transition rates of our Markov model gives the advantage of being able to directly relate the latent behaviour of the IP_3R to parameters within our model. Furthermore, using a finite integral enables us to investigate how the Ca^{2+} signalling dynamics change depending on how much "knowledge" of past Ca^{2+} concentrations the IP_3R has.

The aims of this chapter are:

3.1.2 Chapter Aims

- **Adapt the Siekmann model to create a hybrid stochastic system with integral terms**

  ODEs modelling the gating variables in the Siekmann model (Siekmann et al., 2012; Cao et al., 2013) are replaced with integral terms. Quasi-steady state approximation is used to reduce the number of states from six to two. See Methods 3.2.1.

- **Compare puff statistics for each hybrid stochastic model**

  For each adaptation of the Siekmann model, we simulate Ca^{2+} puffs using a cluster of ten IP_3R and produce the subsequent IPI, puff amplitude and puff duration distributions. The IPI distributions are parameterised using the Time-Dependent distribution and compared to the results by Cao et al. (2013). Through this, we demonstrate a two-state model with integrodifferential equations produces results that are similar to more complex models. See Results 3.3.

- **Analyse the effect changing the delay length and basal level of $\lambda_{h_{42}}$ have on the model**

  Analysis of how changes to the length of the delay within our model affect the Ca^{2+} dynamics provides information on how Ca^{2+} ions and the IP_3R interact. By changing this parameter, we can determine how much "knowledge" of past Ca^{2+} concentrations are required by the IP_3R for it to produce the required Ca^{2+} puffs. Changes to the basal level of $\lambda_{h_{42}}$ change how quickly the IP_3R responds to changes in Ca^{2+} concentrations. We vary this parameter to demonstrate our model produces results that are similar to previous studies (Cao et al., 2013). See Results 3.3.2

3.2 Methods

3.2.1 Hybrid Stochastic Systems

Hybrid stochastic systems, also known as piece-wise deterministic Markov processes, involve the coupling of Markov models to a deterministic differential equation. This method can be used to simulate the behaviour of the Ca^{2+} signalling system. The stochastic behaviour of the IP_3R can be modelled using a Markov model, where the states of the Markov model represent the open and closed state of the channel. The next active state is dependent only on the current active state and the tendency of the channel changing states is indicated by the speed of the transition rates (Tveito and Lines, 2016; Siekmann et al., 2019).

The six-state IP_3R model

The Siekmann model, presented in Fig 1.5, is a six-state Markov model with two modes. The first mode consists of four states (three closed and one open) and the second mode of two states (one closed and one open). These modes describe the open probability of the ion channel. When the channel is in the four-state mode, known as the active mode, it has an open probability of ≈ 0.7, whereas when the channel is in the two-state mode, known as the inactive mode, it has an open probability of ≈ 0. All the transition rates between the states are constant with the exception of q_{24} and q_{42} which are both Ca^{2+} and IP_3 dependent.

The differential equations describing the transitions between states can be represented in matrix form. The matrix of the transition rates and vector of the states is known as the Q matrix. The Q matrix for the six-state Siekmann model is presented in Eq 3.1.

$$\begin{Bmatrix} \frac{dC_1}{dt} \\ \frac{dC_2}{dt} \\ \frac{dC_3}{dt} \\ \frac{dC_4}{dt} \\ \frac{dO_5}{dt} \\ \frac{dO_6}{dt} \end{Bmatrix} = \begin{Bmatrix} -q_{12} & q_{12} & 0 & 0 & 0 & 0 \\ q_{21} & -(q_{21}+q_{23}+q_{24}+q_{26}) & q_{23} & q_{24} & 0 & q_{26} \\ 0 & q_{32} & -q_{32} & 0 & 0 & 0 \\ 0 & q_{42} & 0 & -(q_{42}+q_{45}) & q_{45} & 0 \\ 0 & 0 & 0 & q_{54} & -q_{54} & 0 \\ 0 & q_{62} & 0 & 0 & 0 & -q_{62} \end{Bmatrix} \begin{Bmatrix} C_1 \\ C_2 \\ C_3 \\ C_4 \\ O_5 \\ O_6 \end{Bmatrix} \tag{3.1}$$

The rates q_{24} and q_{42} are calculated using two Ca^{2+}-dependent gating variables each, m_{24}, m_{42}, h_{24}, h_{42} as shown in Eq 3.2 and Eq 3.3. The parameters a_{24}, a_{42}, V_{24} and V_{42} are constant.

$$q_{24} = a_{24} + V_{24}(1 - m_{24}h_{24}) \tag{3.2}$$

$$q_{42} = a_{42} + V_{42}m_{42}h_{42} \tag{3.3}$$

By replacing m_{24}, m_{42}, h_{24}, h_{42} with the Ca^{2+} dependency $m_{24\infty}$, $m_{42\infty}$, $h_{24\infty}$, $h_{42\infty}$ are defined as:

$$m_{24\infty} = \frac{c^{n_{24}}}{c^{n_{24}} + k_{24}^{n_{24}}} \tag{3.4}$$

$$h_{24\infty} = \frac{k_{-24}^{n_{-24}}}{c^{n_{-24}} + k_{-24}^{n_{-24}}} \tag{3.5}$$

$$m_{42\infty} = \frac{c^{n_{42}}}{c^{n_{42}} + k_{42}^{n_{42}}} \tag{3.6}$$

$$h_{42\infty} = \frac{k_{-42}^{n_{-42}}}{c^{n_{-42}} + k_{-42}^{n_{-42}}} \tag{3.7}$$

The steady state rates $q_{24\infty}$ and $q_{42\infty}$ fit the Ca^{2+}-dependency of the gating variables inferred by Siekmann et al. (2012) from the data by Wagner and Yule (2012). $q_{24\infty}$ and $q_{42\infty}$ are defined as:

$$q_{24\infty} = a_{24} + V_{24}(1 - m_{24\infty}h_{24\infty}) \tag{3.8}$$

$$q_{42\infty} = a_{42} + V_{42}m_{42\infty}h_{42\infty} \tag{3.9}$$

The Cao et al. model Cao et al. (2013) observed that the model $Q(c)$ (Eq 3.1) with Ca^{2+}-dependent rates q_{24} and q_{42}, Eq 3.8 and Eq 3.9, parameterised by Eq 3.4-3.7 failed to produce realistic puffs. They introduced a delayed response to changes in the Ca^{2+} concentration by representing m_{24}, m_{42}, h_{24}, h_{42} as Hodgkin-Huxley-like gating variables (Hodgkin and Huxley, 1952).

The gating variables m_{24}, m_{42}, h_{24} and h_{42} are assumed to obey the ordinary differential equation (ODE):

$$\frac{dG}{dt} = \lambda_G(G_\infty - G) \quad (G = m_{24}, m_{42}, h_{24}, h_{42}) \tag{3.10}$$

Where G=m_{24}, m_{42}, h_{24} and h_{42}, $G_\infty = m_{24\infty}$, $m_{42\infty}$, $h_{24\infty}$, $h_{42\infty}$. In the Siekmann model (Siekmann et al., 2012) the gating variables, G, were set immediately to their steady state, G_∞, when there was a change in Ca^{2+} concentration. Rather than instantaneously attaining G_∞, when modelling G as gating variables Cao et al. (2013) introduce the rate λ_G which represents how quickly G approaches G_∞ from its current value.

The rates at which m_{24}, h_{24} and m_{42} reach their equilibrium are constant (Cao et al., 2013). However, h_{42} gating variable has a more complex dynamic and its rate was modelled heuristically by Cao et al. (2013) as:

$$\lambda_{h_{42}} = a_{h_{42}} + \frac{V_{h_{42}}c^7}{c^7 + 20^7} \tag{3.11}$$

Where $a_{h_{42}}$ and $V_{h_{42}}$ are constants. When the Ca^{2+} concentration is low, the rate $\lambda_{h_{42}}$ will be low. Similarly, when the Ca^{2+} concentration is high, $\lambda_{h_{42}}$ will be high. The parameters of the gating variable equations were chosen so that the resulting model showed a delayed response consistent with the data by Mak et al. (2007).

Introducing integral terms into the Cao et al. model We aim to adapt the delayed response in the Cao et al. model to create a model that detects changes in the Ca^{2+} concentration $c(t)$ over a period of time. Therefore, rather than "sensing" $c(t)$ at the current time t, the IP_3R "observes" the Ca^{2+} concentrations over a time interval $It = [t - \tau, t]$ that reaches a certain length of time in the past.

We introduce an integral over the Ca^{2+} concentration $c(t)$ over the time interval $\mathcal{I}(t)$:

$$\bar{c}(t) = \frac{1}{\tau} \int_{t-\tau}^{t} f(c(s))ds \tag{3.12}$$

with $f : \mathbb{R}^+ \to \mathbb{R}^+$ and $\tau > 0$. For $\tau = 0$ we set $\bar{c}(t) = c(t)$. Choosing $f = \text{id}$ i.e. $\bar{c}(t) = \frac{1}{\tau} \int_{\tau-t}^{t} c(s)ds$. Eq 3.12 is a temporal average of $c(t)$ over the interval $\mathcal{I}(t)$. For general positive f, Eq 3.12 can be interpreted as a weighted temporal average of $c(t)$ over $\mathcal{I}(t)$.

Models such as the Siekmann et al. (2012) model are formulated as Ca^{2+}-dependent infinitesimal generators $Q(c)$; by allowing for time-dependent $c(t)$ we obtain the time-dependent infinitesimal generator $Q(c(t))$. To account for the delayed response to changes in Ca^{2+} concentrations (Mak et al., 2007) we replace the substitution of the current Ca^{2+} concentration $c(t)$ at time t into $Q(c)$, see Eq 3.1, with the weighted temporal average $\bar{c}(t)$ defined by Eq

3.12. The time-dependent infinitesimal generator of our new model is $Q(\bar{c}(t))$. Moreover, because for $\tau = 0$, we have $Q(\bar{c}(t)) = Q(c(t))$, using the temporal average $\bar{c}(t)$ defined by Eq 3.12 is a natural extension of defining the time-dependent infinitesimal generator using the current Ca^{2+} concentration $c(t)$.

This shows that for a given infinitesimal generator which has been parametrised using data obtained at constant Ca^{2+} concentrations such as Wagner and Yule (2012), a model that appropriately responds to changes in Ca^{2+} concentration can be found by determining the time τ and the function f to obtain $\bar{c}(t)$ Eq 3.12. Rather than searching for suitable functions f, we take advantage of the fact that our new model can be shown to be mathematically equivalent to the model by Cao et al. (2013) if we choose $\tau = \infty$. Following an approach demonstrated by Brady (1972) for the Hodgkin-Huxley model, it is possible to represent the gating variables used by Cao et al. (2013) as integrals by explicitly solving the four linear differential equations for the gating variables. Thus, by incorporating these integrals into the infinitesimal generator $Q(c)$ we obtain a system of integrodifferential equations with infinitesimal generator $Q(\bar{c}(t))$ which is equivalent to the model by Cao et al. (2013) if we choose $\tau = \infty$.

The Brady model We now introduce the integrodifferential equations by Brady (1972) into our model. Brady (1972) transforms Eq 3.13 into Eq 3.14. The advantage of using this approach is that it allows us to create a model equivalent to the one presented by Cao et al. (2013), enabling direct comparison of results. An in-depth proof of the theory can be found in Brady (1970, 1972).

$$\frac{dJ}{dt} = (\alpha_J \circ f)(1 - J) - (\beta_J \circ f)J \tag{3.13}$$

$$\Phi_J(t, f) = J(0)exp\left[-\int_0^t (\alpha_J \circ f + \beta_J \circ f)(x)dx\right] - exp\left[-\int_0^t (\alpha_J \circ f + \beta_J \circ f)(x)dx\right] \int_0^t (-\alpha_J \circ f)(s) \times \quad exp\left[\int_0^s (\alpha_J \circ c + \beta_J \circ f)(x)dx\right] ds \tag{3.14}$$

where J and f represent the gating variables within the Hodgkin-Huxley model and functions with the domain $[0, \infty)$ that are analytical on $(0, \infty]$, respectively.

If we write Eq 3.10 in the form of Eq 3.13 we get the following equation:

$$\frac{dG}{dt} = (\alpha_G \circ c)(1 - G) - (\beta_G \circ c)G \tag{3.15}$$

where G represents the gating variables, $m_{24}, h_{24}, m_{42}, h_{42}$ and c represents the Ca^{2+} concentration. The initial values are: t_0=0, c(t_0)=0.1 µM, G(t_0)=$\frac{\alpha_G(0)}{\alpha_G(0)+\beta_G(0)}$.

To derive α and β we begin by expanding the right hand side (RHS) of Eq 3.10:

$$\frac{dG}{dt} = \lambda_G G_\infty - \lambda_G G \tag{3.16}$$

Next, we add and subtract $\lambda_G G_\infty$ from the RHS of Eq 3.16:

$$\frac{dG}{dt} = \lambda_G G_\infty - \lambda_G G - \lambda_G G_\infty G + \lambda_G G_\infty G \tag{3.17}$$

Factorising Eq 3.17 gives:

$$\frac{dG}{dt} = \lambda_G G_\infty (1 - G) - (\lambda_G - \lambda_G G_\infty) G \tag{3.18}$$

α_G and β_G are thus:

$$\alpha_G = \lambda_G G_\infty \tag{3.19}$$

$$\beta_G = \lambda_G - \lambda_G G_\infty \tag{3.20}$$

Substituting Eq 3.19 and 3.20 into Eq 3.14 gives:

$$\Phi_G(t,c) = G(0) exp\left[-\int_0^t (\alpha_G \circ c + \beta_G \circ c)(x)dx\right] - exp\left[-\int_0^t (\alpha_G \circ c + \beta_G \circ c)(x)dx\right] \int_0^t (-\alpha_G \circ c)(s) \times \quad exp\left[\int_0^s (\alpha_G \circ c + \beta_G \circ c)(x)dx\right] ds \tag{3.21}$$

The addition of α_{G} and β_{G} reduces to λ_{G}, therefore, Eq 3.21 can be simplified to:

$$\Phi_G(t,c) = G(0) exp\left[-\int_0^t (\lambda_G \circ c)(x)dx\right] - exp\left[-\int_0^t (\lambda_G \circ c)(x)dx\right] \int_0^t (-\alpha_G \circ c)(s) \times \quad exp\left[\int_0^s (\lambda_G \circ c)(x)dx\right] ds \tag{3.22}$$

We aim to build a model that exhibits a delayed response to changes in the Ca^{2+} concentration, as observed by Mak et al. (2007), which is essential

for producing realistic Ca^{2+} puffs. We interpret the integrals in Eq 3.22 as the IP_3R averaging over past Ca^{2+} concentrations. The transformation to integrodifferential equations introduces an infinite delay i.e. the integrals replacing the gating variables extend over the time interval $(-\infty, t]$. This not only makes the numerical solution of the model equations computationally infeasible but implies that the IP_3R has an "infinite" memory which appears unrealistic. For this reason, we consider integrals with finite delays, τ (see Eq 3.23). τ can be interpreted as how far into the past the ion channel's memory spans.

$$\Phi_G(t,c) = G(0)exp\left[-\int_{t-\tau}^{t}(\lambda_G \circ c)(x)dx\right] - exp\left[-\int_{t-\tau}^{t}(\lambda_G \circ c)(x)dx\right] \int_{t-\tau}^{t}(-\alpha_G \circ c)(s) \times \quad exp\left[\int_{s-\tau}^{s}(\lambda_G \circ c)(x)dx\right] ds \tag{3.23}$$

In our model, we replace the ODEs in the Siekmann model (Eq 3.10) with the integrodifferential equation described in Eq 3.23. Parameters, detailed in Table 3.1, can be substituted into Eq 3.19 to calculate the correct α_G value for each gating variable. λ_G and α_G are substituted into Eq 3.22.

The reduced six-state IP_3R model

Quasi-steady-state approximation replaces the ODEs for fast variables and therefore reduces the number of equations in the system down so only a system for slow variables exists (Vejchodský et al., 2014). Cao et al. (2013); Sneyd et al. (2017) state the rate at which the gating variables m_{24}, h_{24} and m_{42} reach equilibrium is so quick, that they can be set equal to their steady

Table 3.1: Model parameters. IP_3-dependent parameters are evaluated at a concentration of 0.1 µM as indicated by subscripts. Full model details are given in Cao et al. (2013).

Symbol	Description	Value	Units
	Gating kinetics		
a_{24}	Basal level of q_{24}	$29.85_{p=0\,1\mu M}$	s^{-1}
V_{24}	Gating-dependent part of q_{24}	$312.85_{p=0\,1\mu M}$	s^{-1}
a_{42}	Basal level of q_{42}	$0.05_{p=0\,1\mu M}$	s^{-1}
V_{42}	Gating-dependent part of q_{42}	100	s^{-1}
$\lambda_{h_{24}}$	Rate of approach to steady state of h_{24}	40	s^{-1}
n_{-24}	Hill coefficient for Ca^{2+} dependency of $h_{24\infty}$	$0.04_{p=0\,1\mu M}$	
k_{-24}	Half-saturation constant for Ca^{2+} dependency of $h_{24\infty}$	$97.00_{p=0\,1\mu M}$	
$h_{24\infty}$	Steady state of h_{24}	$\frac{k_{-24}^{n_{-24}}}{c^{n_{-24}}+k_{-24}^{n_{-24}}}$	
$a_{h_{42}}$	Basal level of $\lambda_{h_{42}}$ (tuning parameter)	0.5	s^{-1}
$V_{h_{42}}$	Ca^{2+}-dependent part of $\lambda_{h_{42}}$	100	s^{-1}
$K_{h_{42}}$	Half-saturation constant for Ca^{2+}-dependency of $\lambda_{h_{42}}$	20	µM
$\lambda_{h_{42}}$	Rate of approach to steady state of h_{42}	$a_{h_{42}}+\frac{V_{h_{42}}c^7}{c^7+K_{h_{42}}^7}$	s^{-1}
n_{-42}	Hill coefficient for Ca^{2+} dependency of $h_{42\infty}$	$3.23_{p=0\,1\mu M}$	
k_{-42}	Half-saturation constant for Ca^{2+} dependency of $h_{42\infty}$	$0.17_{p=0\,1\mu M}$	
$h_{42\infty}$	Steady state of h_{42}	$\frac{k_{-42}^{n_{-42}}}{c^{n_{-42}}+k_{-42}^{n_{-42}}}$	
$\lambda_{m_{24}}$	Rate of approach to steady state of m_{24}	100	s^{-1}
n_{24}	Hill coefficient for Ca^{2+} dependency of $m_{24\infty}$	$6.31_{p=0\,1\mu M}$	
k_{24}	Half-saturation constant for Ca^{2+} dependency of $m_{24\infty}$	$0.549_{p=0\,1\mu M}$	
$m_{24\infty}$	Steady state of m_{24}	$\frac{c^{n_{24}}}{c^{n_{24}}+k_{24}^{n_{24}}}$	
$\lambda_{m_{42}}$	Rate of approach to steady state of m_{42}	100	s^{-1}
n_{42}	Hill coefficient for Ca^{2+} dependency of $m_{42\infty}$	$11.16_{p=0\,1\mu M}$	
k_{42}	Half-saturation constant for Ca^{2+} dependency of $m_{42\infty}$	$0.40_{p=0\,1\mu M}$	
$m_{42\infty}$	Steady state of m_{42}	$\frac{c^{n_{42}}}{c^{n_{42}}+k_{42}^{n_{42}}}$	
	Ca^{2+} balance		
c_h	Elevated Ca^{2+} in vicinity of open IP_3R channel	120	µM
B	Total buffer concentration	20	µM
k_{on}	Binding of fluo4 buffer to Ca^{2+}	150	$\mu M s^{-1}$
k_{off}	Unbinding of fluo4 buffer from Ca^{2+}	300	s^{-1}
J_r	Flux of Ca^{2+} through single channel	200	$\mu M s^{-1}$
J_{leak}	Ca^{2+} influx from cluster environment	33	$\mu M s^{-1}$
V_d	Rate of cytoplasmic Ca^{2+} removal from the cluster	4000	µM s^{-1}
K_d	Half-saturation constant for cytoplasmic Ca^{2+} removal	12	µM

state.

That is:

$$m_{24} = m_{24\infty}, \quad h_{24} = h_{24\infty}, \quad m_{42} = m_{42\infty} \tag{3.24}$$

Therefore the reduced model consists of six ODEs and an integral term, modelling the h_{42} gating variable.

The reduced two-state IP_3R model

Reduction of the six-state IP_3R model simplifies the model, whilst keeping the desired Ca^{2+} dynamics (Cao et al., 2014).

We reduce our six-state model further by using the following steps, previously demonstrated by Cao et al. (2014):

- Set the rates q_{21}, q_{23}, q_{26} and q_{45} to zero. States C_1, C_3 and O_5 have been shown to be rarely visited by the IP_3R or have a short dwell time.
- States C_2 and O_6 are combined to create a partially open state with an open probability of $\frac{q_{26}}{(q_{26}+q_{62})}$
- Due to the combining of states C_2 and O_6, the rate q_{24} is re-scaled by $\frac{q_{62}}{(q_{62}+q_{26})}$.

The reduced two-state Siekmann model, presented in Fig 3.1, ignores the structure of the active and inactive modes seen within the six-state Siekmann model and only the inter-modal transitions have an effect on the IP_3R behaviour (Cao et al., 2013). Constant parameters for rates q_{24} and q_{42} remain the same as those in Eq 3.2 and 3.3.

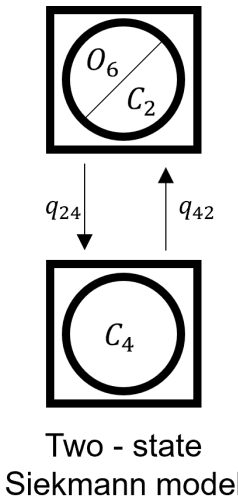

Figure 3.1: The structure of the two-state Siekmann Model (Cao et al., 2013). The active mode consists of the joint states C_2 and O_6; the inactive mode consists of the closed state C_4.

3.2.2 Latency distributions

The time it takes for the IP_3R to first open or close following a step change in ligand concentration, as demonstrated by the experiments conducted by Mak et al. (2007), can be simulated mathematically using our single channel models. We replicate the experimental conditions of Mak et al. (2007) by setting the IP_3 concentration to 10µM and using the same Ca^{2+} concentrations (10nM, 2µM, 300µM) to conduct the rapid changes in ligand concentration. We assume the past Ca^{2+} concentration of length τs is constant at the initial Ca^{2+} concentration used within the experiments. We run 1000 iterations for each model and compare our latency distributions to the results by Mak et al. (2007).

3.2.3 Deterministic calcium dynamics

Using the same system of ODEs as in Cao et al. (2013), we develop a model that accounts for various fluxes that influence the Ca^{2+} concentration, c, in the cytosol as well as the Ca^{2+} dye, b_{fluo4}.

$$\frac{dc}{dt} = J_{\text{increase}} N_{\text{o}} + J_{\text{leak}} - J_{\text{decrease}} - k_{\text{on}}(B_{\text{fluo4}} - b_{\text{fluo4}})c + k_{\text{off}} b_{\text{fluo4}} \tag{3.25}$$

$$\frac{db_{\text{fluo4}}}{dt} = k_{\text{on}}(B_{\text{fluo4}} - b_{\text{fluo4}})c - k_{\text{off}} b_{\text{fluo4}} \tag{3.26}$$

Ca^{2+} fluxes can be modelled deterministically using ODEs if we assume the cell is spatially homogeneous (Dupont et al., 2016; Rahmani et al., 2024). Whilst this is a simplification of the true cellular behaviour, we can still gain insight into the Ca^{2+} signalling system (Dupont et al., 2016). Eq 3.25 and Eq 3.26 describe the Ca^{2+} concentration and the Ca^{2+} dye, respectively. The Ca^{2+} flux is described through the parameters J_{increase}, J_{leak} and J_{decrease}. J_{increase} represents the Ca^{2+} flux through an open IP_3R; N_{o} is the number of open IP_3R in a cluster. The leakage of Ca^{2+} from the ER is described using J_{leak}. J_{decrease} represents the Ca^{2+} flux that returns to the ER (Cao et al., 2013; Siekmann et al., 2019). Eq 3.26 represents the Ca^{2+} dye bound to Ca^{2+} that is detected using a light microscope within experiments (Cao et al., 2013). The changes in the Ca^{2+} signalling can be visualised through the changes in the fluorescence light correlating with changes in Ca^{2+} signalling (Pratt et al., 2020). This process is described in Eq 3.25 - 3.26 using parameters B_{fluo4} and b_{fluo4}, which represent the total dye buffer concentra-

tion and the Ca^{2+}-bound dye buffer concentration, respectively (Siekmann et al., 2019). For the two-state model, all parameters remain the same as those for the six-state model except for $J_{increase}$ which is replaced with $J_{increase} \cdot \frac{q_{26}}{(q_{62}+q_{26})}$ (Cao et al., 2014). Parameter values are detailed in Table 3.1.

3.2.4 Calcium puff statistics

Ca^{2+} puffs are often characterised by taking into consideration three key statistics: the IPI, the puff amplitude and the puff duration. IPIs are defined as being the time between the peak amplitude of Ca^{2+} puffs. We determine the start of a Ca^{2+} puff as being when the Ca^{2+} concentration is 20% of the peak amplitude. Similarly, the end of the puff is calculated the time after the peak where the Ca^{2+} concentration is 20% of the peak amplitude. The difference in the end and start times determines the duration of the Ca^{2+} puff.

We fit our simulated IPI distributions to the Time-Dependent distribution (Thurley et al., 2011), introduced in Chapter 2, by calculating the suitable parameters for it. To recall, the Time-Dependent distribution is:

$$P_{IPI} = \lambda(1 - \exp(-\xi t)) \exp(-\lambda t + \lambda(1 - \exp(-\xi t))/\xi) \tag{3.27}$$

where λ is the puff rate and ξ is the recovery rate. We estimated the mean IPI from the data and set λ as the reciprocal of this value, as previously demonstrated by Cao et al. (2017). When fitting the Time-Dependent distribution to our IPI distributions in Chapter 2, we also estimated λ. Here, to ensure an accurate comparison with the results of Cao et al. (2013, 2017),

we use their methodology. ξ is optimised using the *lsqcurvefit* function in MATLAB. Furthermore, we evaluate the difference between λ being the reciprocal of the mean to if it was optimised using methods outlined in Chapter 2.

3.2.5 Numerical methods

We solve Eq 3.25 - 3.26 using the fourth-order Runge-Kutta method whereas the dynamics of the Markov models representing the IP_3R channels are simulated with a Gillespie algorithm. Due to the rates q_{24} and q_{42} being Ca^{2+} dependent, they are time-dependent. For this reason, the original Gillespie algorithm cannot be used. Adaptive timing, as detailed in Alfonsi et al. (2005); Cao et al. (2013); Rüdiger (2013), is used to make the algorithm more run-time-efficient. A maximum time step size of 10^{-4} s is used for the six and two-state models. Integrals in Eq 3.23 are calculated using the Riemann Sum, using a larger time step (10^{-2} s). As evidenced in Fig 3.12, the increased time-step strongly increases computational efficiency whilst not significantly decreasing the approximation accuracy of the integral. IP_3 is set to 0.1 µM for all simulations. We assume Ca^{2+} concentrations prior to time t_0 are constant and low at 0.1µM. τ and $a_{h_{42}}$ are set to 3s and $0.5s^{-1}$, respectively, unless stated otherwise. All results were gathered using MATLAB (MathWorks, Natick, MA).

3.3 Results

3.3.1 Replacing the ODEs calculating the gating variables in the Siekmann model with integral terms produces equivalent results to Cao et al. (2013)

An example of a Ca^{2+} trace simulated from our six-state hybrid stochastic model with integrodifferential equations can be seen in Fig 3.2A. The trace, qualitatively, is similar to Ca^{2+} traces produced by the model of Cao et al. (2013). To make a more quantitative comparison between the Siekmann model and our model, Ca^{2+} puff statistics were derived. The fitting of simulated IPI distributions to the Time-Dependent distributions produces parameter values ($\lambda = 0.2486s^{-1}$, $\xi = 0.6267s^{-1}$) that are similar to those described by Cao et al. (2013) ($\lambda = 0.2463s^{-1}, \xi = 0.8s^{-1}$). If λ is optimised alongside ξ, parameter values are $1.1546s^{-1}$ and $0.1255s^{-1}$. Replacing the ODEs modelling the gating variables in the Siekmann model (Siekmann et al., 2012; Cao et al., 2013) with integral terms, appears to cause an increased delay in the IP_3R reopening following a Ca^{2+} puff. The average IPI are indistinguishable.

Latency distributions In Fig 3.3 we present the latency distributions produced by our six-state model. The peak maximum activation latency for a step change in Ca^{2+} concentration from 10nM to 2µM is shorter ($\sim$ 0.02 s) in comparison to when there is a step change in Ca^{2+} concentration from 300µM to 2µM ($\sim$ 0.08 s). Additionally, the maximum activation latency for a step change in Ca^{2+} from 300µM to 2µM is larger (0.42 s). The deactivation

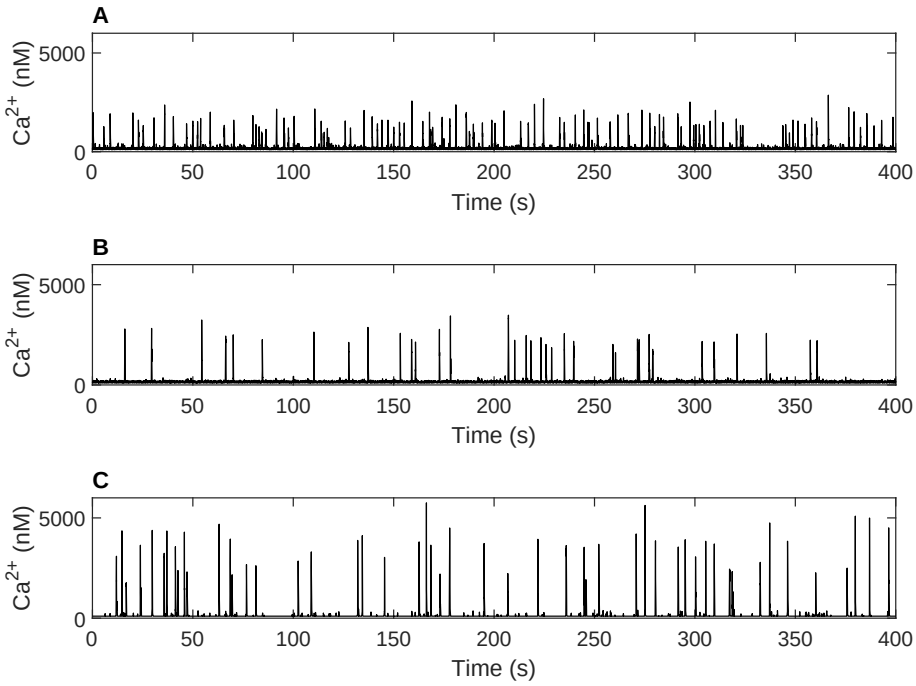

Figure 3.2: Ca^{2+} puff traces produced by hybrid stochastic systems that simulate the gating variables using integrodifferential equations. A: six-state model with four gating variables. B: six-state model with one gating variable. C: two-state model with one gating variable.

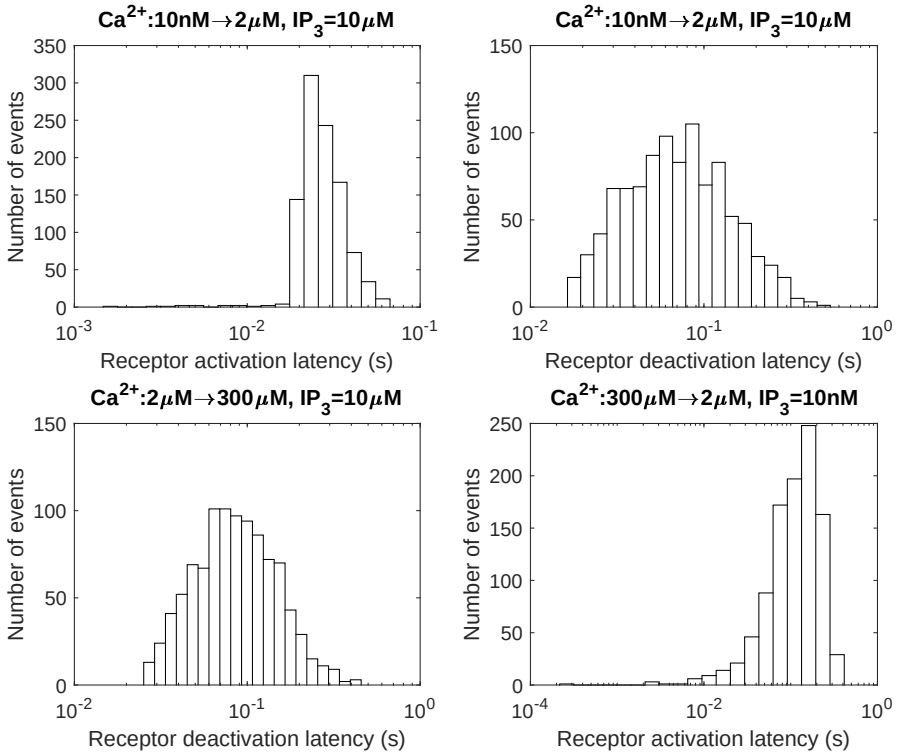

Figure 3.3: Simulated latency distributions, using the six-state IP_3R model, for step changes in Ca^{2+} concentrations as indicated in the subfigure titles. IP_3=10µM

latency distributions are qualitatively similar with maximum peaks ≈0.08s.

3.3.2 Using quasi-steady-state approximation reduces the model whilst maintaining the correct puff dynamics

The reduced six-state model

Quasi-steady-state approximation was used to reduce the number of gating variables in the six-state model, described in Section 3.3.1. The m_{24}, h_{24}

and m_{42} gating variables are set to their steady state resulting in a six-state model with one integral, calculating the h_{42} gating variable. We refer to this simplified model as the "reduced six-state model". An example of a Ca^{2+} trace produced by the reduced six-state model can be seen in Fig 3.2B. A clear qualitative difference between the six-state model and the reduced six-state model Ca^{2+} traces is the frequency of Ca^{2+} puffs. Fig 3.2B shows a Ca^{2+} trace that has larger IPIs and Ca^{2+} puffs with higher amplitudes. The change in frequency of Ca^{2+} puffs is confirmed through comparison of parameter estimations of the Time-Dependent distribution. A smaller λ value of $0.0986s^{-1}$ shows the average IPI is greater than the six-state model, whilst a lower ξ value of $0.1723s^{-1}$ indicates at a slower puff recovery time. λ and ξ optimised together produces values of $0.1055s^{-1}$ and $0.9888s^{-1}$. In Fig 3.4 we compare IPI, puff amplitude and puff duration distributions for the six state models. The IPI distribution for the reduced six-state model shows IPIs that are longer than those of the six-state model. Ca^{2+} puff amplitudes are higher, however the duration of puffs is shorter.

Latency distributions Fig 3.5 shows the activation and deactivation latency distributions produced using our reduced six-state model. All four distributions qualitatively follow a similar shape. The first time to open following a step change in Ca^{2+} concentration from 10nM to 2µM is quicker (maximum peak at 0.01s) in comparison to a step change in Ca^{2+} from 300µM to 2µM (maximum peak at 0.2s). However, there is greater variability in the activation latency distribution for a step change in Ca^{2+} from 10nM to 2µM. The peak maximum deactivation latency is similar for both step changes in Ca^{2+} concentration from 2µM to 10nM and 2µM to 300µM with peak maxi-

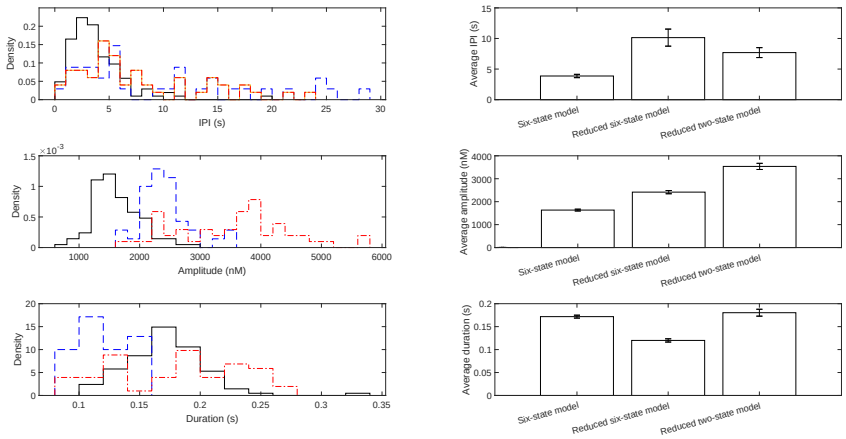

Figure 3.4: Comparison of average Ca^{2+} puff statistics across all three models. Bars depict the mean of each statistic $\pm$ standard error. The six-state model is shown as a solid black line, the reduced six-state model as a blue dashed line and the reduced two-state model as a dot-dashed red line. Simplifying the six-state model using quasi-steady-state approximation leads to a decrease in the frequency of Ca^{2+} puff events. The increase in puff amplitude for these models implies that due to quasi-steady-state approximation a higher number of channels open at the same time, however, the channel requires a longer time to recover from the high Ca^{2+} concentration and reopen.

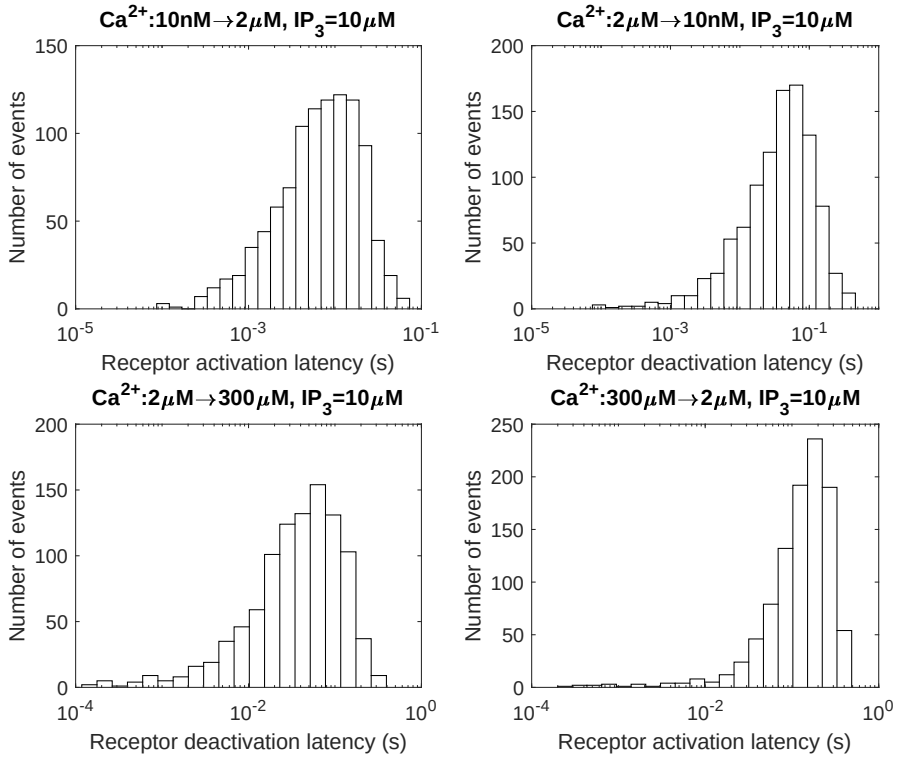

Figure 3.5: Simulated latency distributions, using the reduced six-state IP_3R model, for step changes in Ca^{2+} concentrations as indicated in the subfigure titles. IP_3=10µM

mum values of 0.07 and 0.06s, respectively.

The reduced two-state model

The reduced six-state model can be simplified further by using quasi-steady-state approximation and ignoring low dwell times (Cao et al., 2014). Fig 3.2C shows a Ca^{2+} trace produced by the reduced two-state model. The reduced two-state model produces Ca^{2+} traces that are similar to those produced by more complex six-state models. There are fewer basal level fluctuations in Fig 3.2C due to the reduced two-state model not having a fast-lived open

state (the equivalent to state five in the six-state model). We fit the Time-Dependent distribution to the IPIs from the reduced two-state model and estimate parameters of $\lambda = 0.13\text{s}^{-1}$ and $\xi = 0.3099\text{s}^{-1}$. Ca^{2+} puffs are more frequent and recover quicker when compared to the reduced six-state model. λ and ξ optimised together produces values of 0.4973s^{-1} and 0.0764s^{-1}. In Fig 3.4 we see the IPI distribution for the reduced two-state model is similar to the reduced six-state model. Ca^{2+} puff amplitudes are much higher in comparison to the six-state models, however, puff durations are similar.

A comparison of the puff statistics and averages demonstrates that the reduced two-state model can produce Ca^{2+} dynamics that are a good reflection of more complex models.

Latency distributions In Fig 3.6 we compare the activation and deactivation latency distributions using our reduced two-state model. All distributions are qualitatively similar in shape. The maximum peak activation latencies are 0.01s and 0.19s for the step change in Ca^{2+} concentration from 10nM to 2µM and 300µM to 2µM, respectively. The maximum peak deactivation latencies are similar for both step changes in Ca^{2+} concentration ($\sim$ 0.05s).

The effect of τ on Ca^{2+} dynamics The length of τ can be interpreted as how far into the past the IP_3Rs memory spans. We consider if the IP_3R require "knowledge" of past Ca^{2+} concentrations to function, or is "knowledge" of only the present Ca^{2+} concentrations sufficient. We found 0.1s is the threshold value, where anything smaller than this value is detrimental to the Ca^{2+} dynamics. Fig 3.7 shows that when τ is set to 0.1s or smaller,

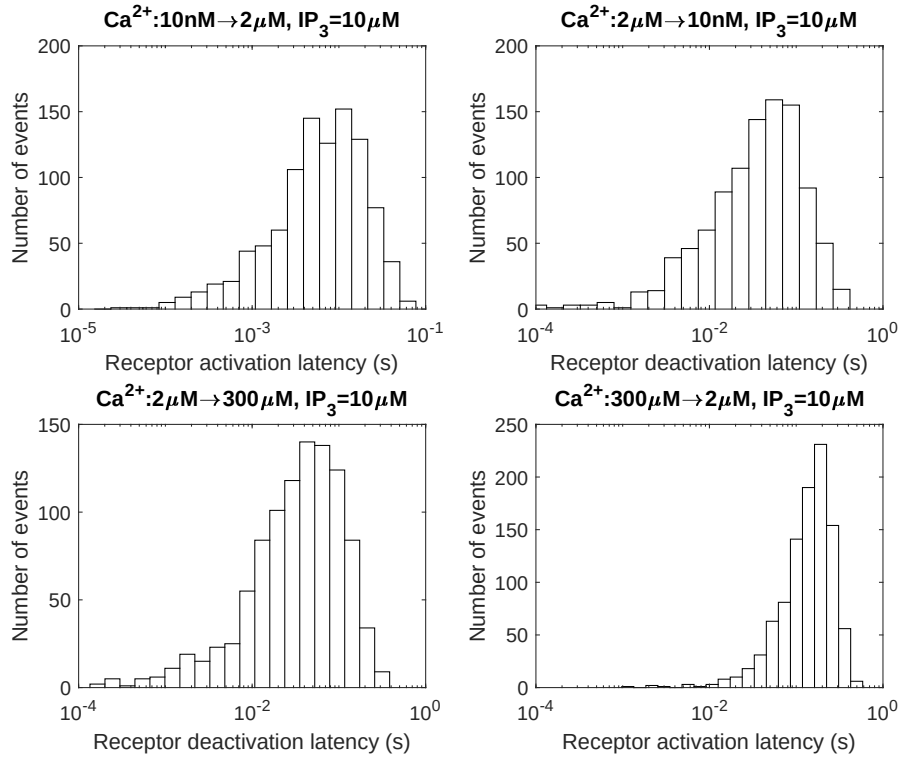

Figure 3.6: Simulated latency distributions, using the reduced two-state IP_3R model, for step changes in Ca^{2+} concentrations as indicated in the subfigure titles. IP_3=$10\mu M$

Ca^{2+} puffs are not produced and the IP_3R stays in a high activity mode. As we increase τ beyond 0.1s, Ca^{2+} puffs are produced. However, when τ =0.2s the Ca^{2+} puffs do not follow the desired shape i.e. a sharp increase in Ca^{2+} concentration with a gradual decent as IP_3R close. Our results show that increasing τ to 3s produces Ca^{2+}puffs of the correct shape. By choosing the length of τ, the correct Ca^{2+} and h_{42} dynamics are simulated, whilst keeping our computational time as low as possible.

h_{42} dynamics within a simplified model The h_{42} gating variable has a complex dynamic within the Ca^{2+} signalling models (Cao et al., 2013). Fig 3.8 shows the effect reducing the six-state model to a two-state model has on the h_{42} dynamics. Fewer fluctuations in the basal level Ca^{2+} concentration cause Eq 3.23 to go to equilibrium if the Ca^{2+} concentration has remained constant for the time length, τ. This behaviour is only seen within the reduced two-state model due to the reduction in basal level fluctuations. In the six-state model, the fast-lived open state, (state five), causes there to be a high frequency of single-channel openings, therefore the h_{42} gating variable never reaches its steady state.

In Fig 3.9 we compare the h_{42} dynamics of the reduced two-state model when τ is 3s and 15s. With a longer length delay, a jump to steady state is less likely to occur due to the average time between Ca^{2+} puffs being shorter than τ. However, computational time increases. Whilst there is a difference between the qualitative behaviour of h_{42}, this does not affect the Ca^{2+} and IP_3R dynamics.

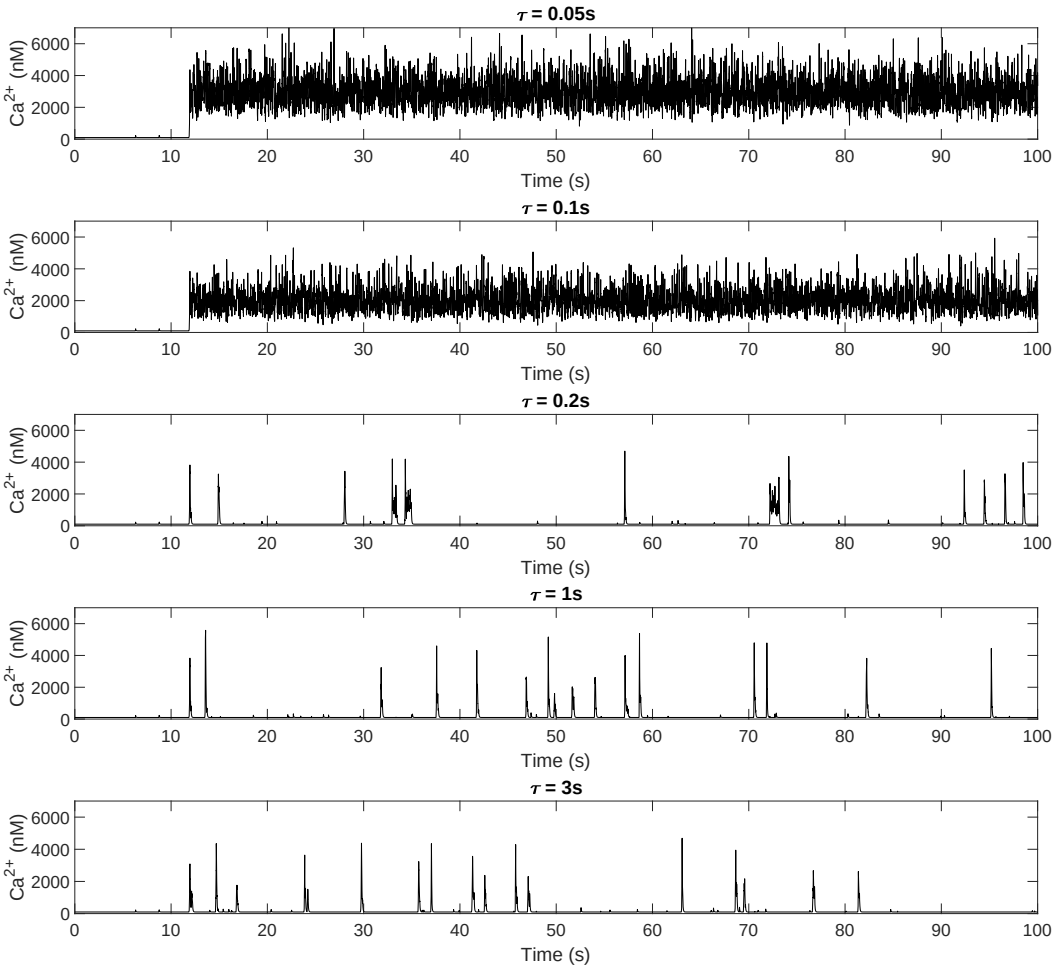

Figure 3.7: Comparison of Ca^{2+} dynamics for τ =0.05s,τ =0.1s,τ =0.2s, τ =1s, and τ =3s.

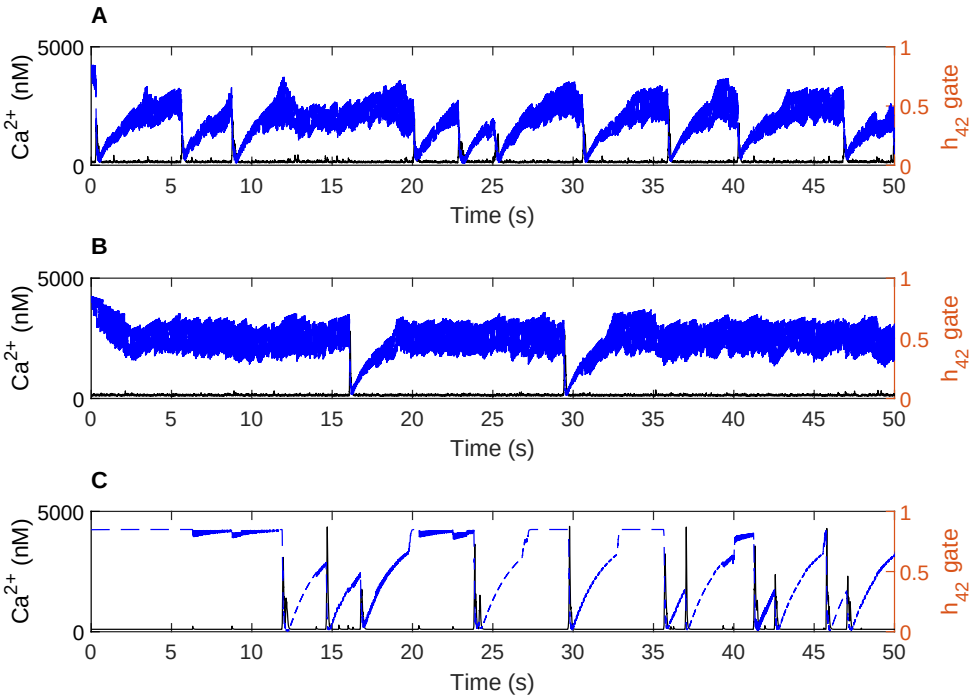

Figure 3.8: Comparison of h_{42} dynamic for all three models. A: six-state model. B: reduced six-state model. C: reduced two-state model.

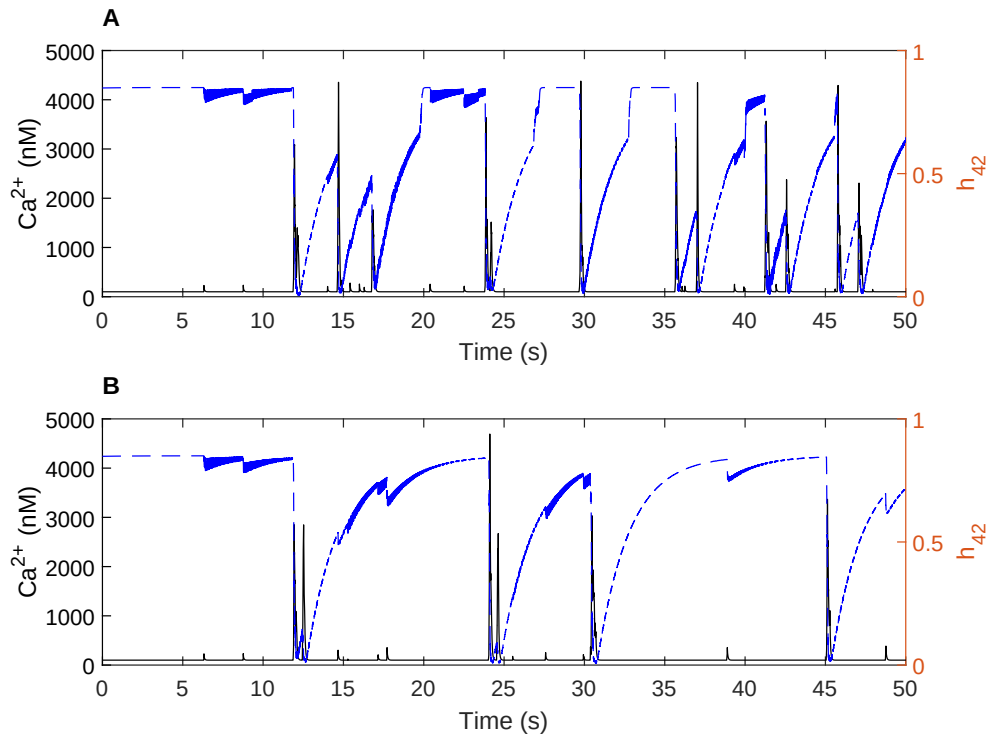

Figure 3.9: Averaged h_{42} gating variable for the two-state model increases quickly to equilibrium if the Ca^{2+} concentration has remained constant for the length of τ. The black full line is the Ca^{2+} concentration, and the blue dashed line is the averaged h_{42} gating variable. The two-state model does not have a fast-lived open state, therefore small fluctuations in the basal Ca^{2+} concentration are limited. Due to this redundancy in a small number of channels open, the Ca^{2+} concentration remains low and constant for longer periods. The integral equation for h_{42} goes to equilibrium if the IP_3R is under these conditions for τs. Therefore, this causes the jump to the h_{42} steady state. If τ is set to a longer length, the sudden increase to equilibrium is not seen. A: $\tau = 3$s. B: $\tau = 15$s

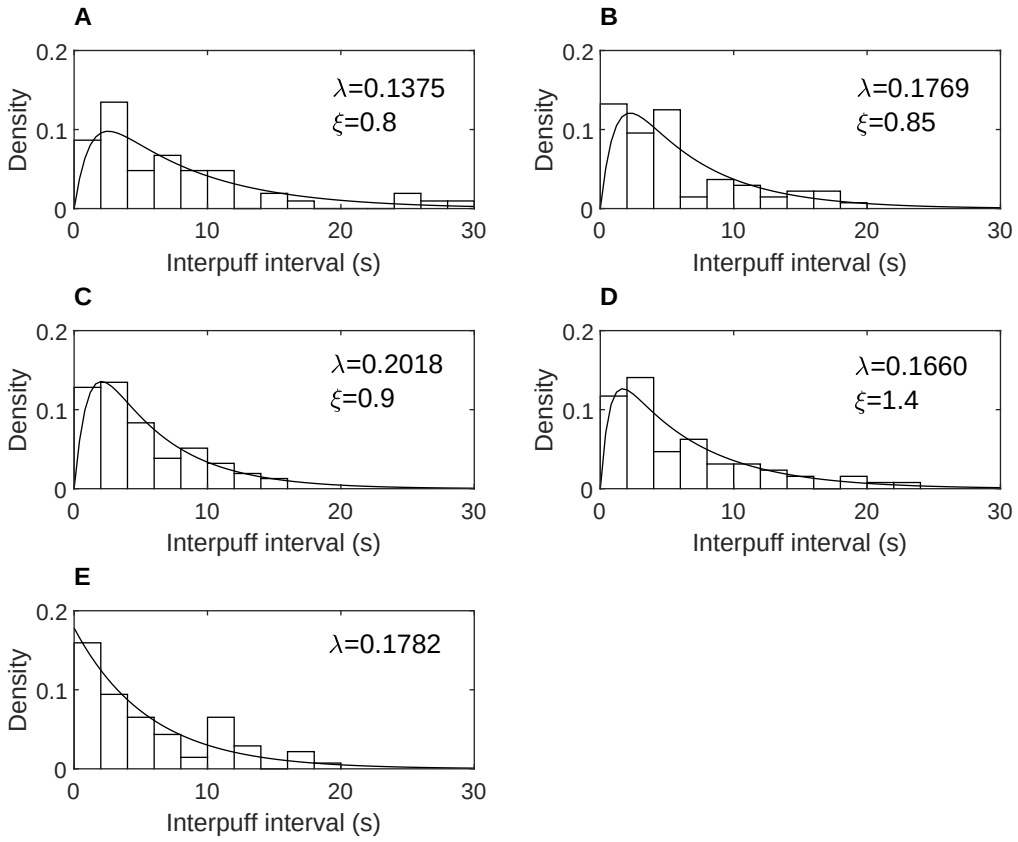

Figure 3.10: Comparison of IPI distributions parameterized using the Time-Dependent distribution for different $a_{h_{42}}$ values. A: $0.1\ \mathrm{s}^{-1}$. B: $0.5\ \mathrm{s}^{-1}$. C: $1\ \mathrm{s}^{-1}$. D: $2\ \mathrm{s}^{-1}$. E: $5\ \mathrm{s}^{-1}$.

Dependence of IPI on a_{h42} Fig 3.10 shows increasing the recovery rate of an IP_3R from Ca^{2+} inhibition, $a_{h_{42}}$, causes the IPI distributions to become exponentially distributed. We fit the IPI distributions to the Time-Dependent distribution. The average IPI is used for the λ value and an appropriate ξ value is used to fit the distribution well. Average IPIs are similar for each distribution, however as $a_{h_{42}}$ increases, the recovery rate from Ca^{2+} inhibition also increases.

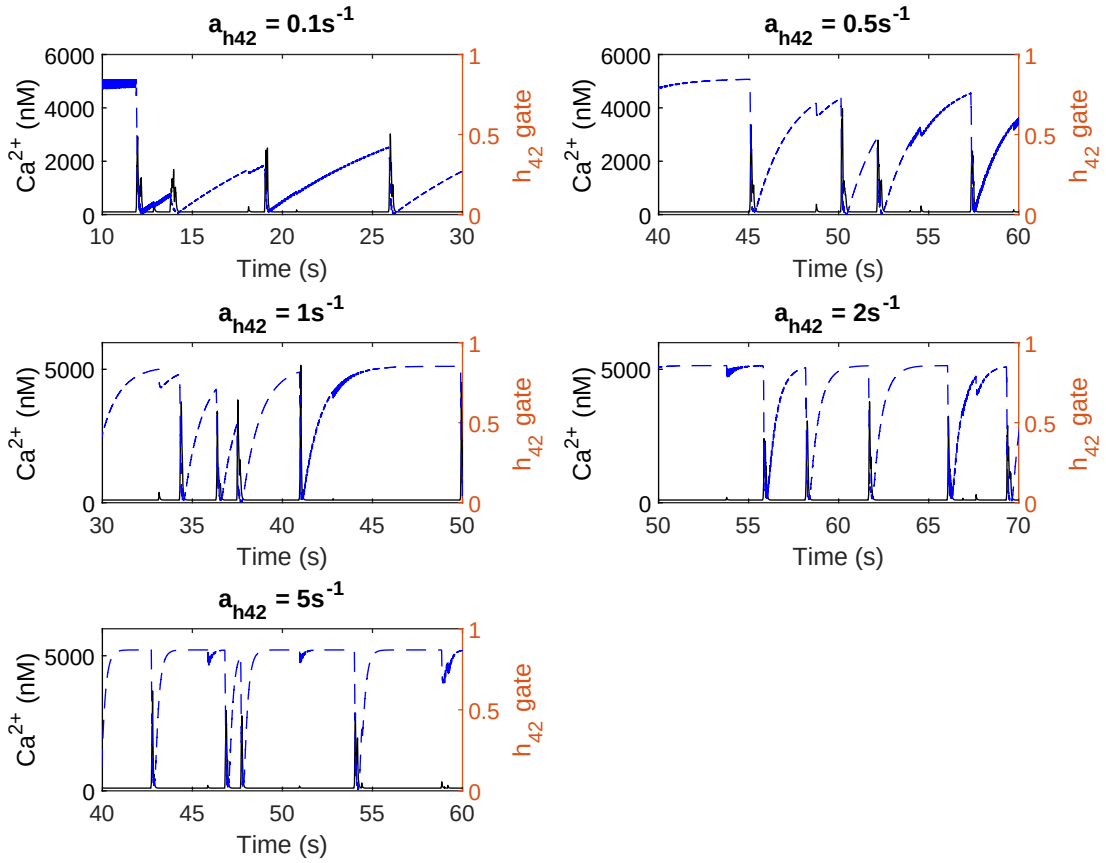

Figure 3.11: Comparison of Ca^{2+} puff and h_{42} traces for different $a_{h_{42}}$ values. Ca^{2+} traces are shown in black and the averaged h_{42} gating variable in blue.

In Fig 3.11 we compare the effect increasing $a_{h_{42}}$ has on the average h_{42} gating variable. As $a_{h_{42}}$ increases, the rate h_{42} reaches a threshold value rises. This is shown by the gradual increase in h_{42} following a Ca^{2+} puff when $a_{h_{42}}$ is $0.1s^{-1}$ compared to the steep increase in h_{42} when $a_{h_{42}}$ is set to $5s^{-1}$.

Time step used to calculate the h_{42} integral term. The computational time for simulating the integral calculating h_{42} can be expensive if the length of τ is long. We have shown that if τ is too short, the Ca^{2+} dynamics fail while

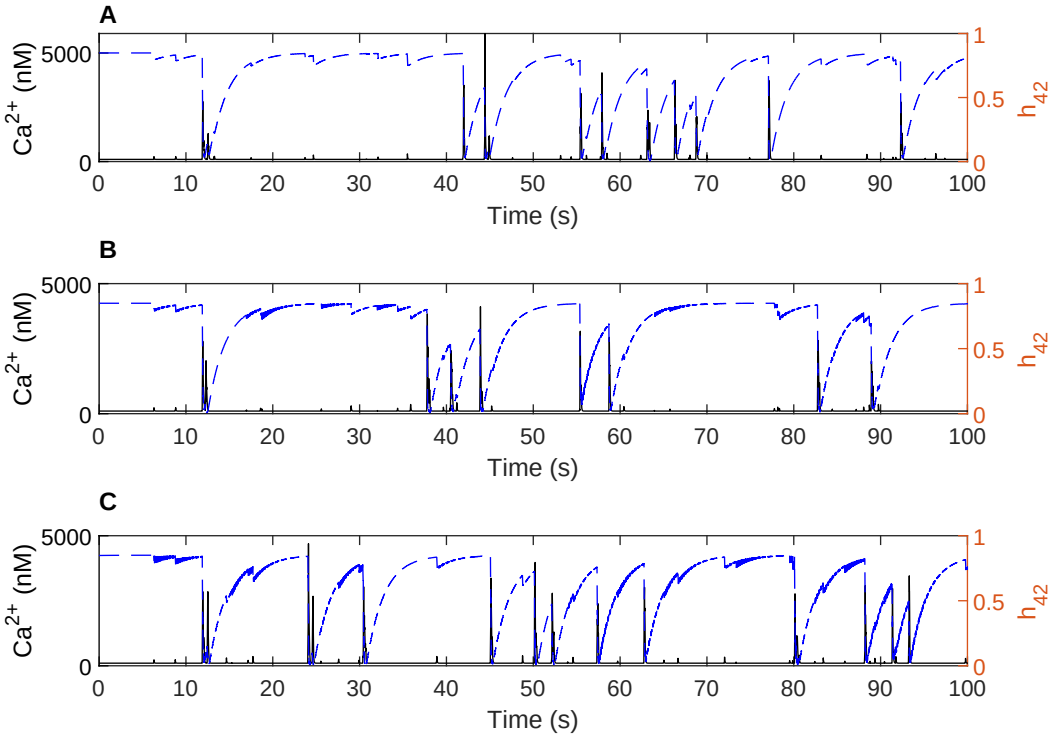

Figure 3.12: Comparison of Ca^{2+} puffs and average h_{42} simulations for different integral time-steps. A: time-step of 10^{-3}s. B: 5×10^{-3}s. C: 10^{-2}s

a longer τ produces the desired Ca^{2+} puffs and h_{42} dynamics. Computational time can be reduced, whilst the Ca^{2+} and h_{42} dynamics are maintained if the time-step used to calculate Eq 3.23 is increased.

Fig 3.12 compares the Ca^{2+} trace and average h_{42} value for time-steps of 10^{-3}s, 5×10^{-3}s and 10^{-2}s. Increasing the time step of the integral improves computational time and retains the required puff dynamics. If the time-step is made too large, the approximation of the integral would become increasingly more inaccurate and the fundamental properties of the Ca^{2+} signalling system would be lost.

3.4 Chapter discussion

Mathematical models simulating the Ca^{2+} signalling system are often complex and require a large number of parameters and equations. This chapter aimed to build a model for the IP_3R that accounts for the delayed response of the channel to changes in Ca^{2+} concentrations observed by Mak et al. (2007). Our model is based on the hypothesis that, rather than only responding to the current Ca^{2+} concentration, the IP_3R depends on the average of Ca^{2+} concentrations reaching τ units of time in the past. Starting with the Siekmann model, which is incapable of generating realistic puffs if coupled directly to the time-dependent Ca^{2+} concentration (Cao et al., 2013), we demonstrated that we can enable the model to produce puffs by replacing the dependency on the current Ca^{2+} concentration with the average Ca^{2+} concentration. This is dependent on the length of the time interval, τ, used for calculating the average Ca^{2+} concentration being sufficiently long. When τ was set to a small value of 0.1s the model failed to generate Ca^{2+} puffs, whereas setting $\tau = 3$s is sufficient for enabling the model to produce puffs for the parameters chosen in Table 3.1. Using the reduced two-state model we showed that the same h_{42} dynamics that are present in the six-state model can be simulated when $\tau = 15$s. However, the Ca^{2+} puffs simulated by this model were similar to those produced when $\tau = 3$s.

Our six-state model successfully produced results that were comparable with those published by Cao et al. (2013). This result was expected for an infinite delay because the integrodifferential method by Brady (1972) and the Hodgkin-Huxley-like equations by Cao et al. (2013) are mathematically equivalent. However, we showed that the results remain similar if the length

of τ is not infinite, but sufficiently long. We then investigated how much the delay could be reduced so that the model would still produce realistic puffs. We chose to use a one-factor-at-a-time approach, focusing only on the parameter τ. This enabled us to accurately compare our model results with those of Cao et al. (2013), as we incorporated the remaining parameters from their study into our own model. Next, we simplified our model by using a quasi-steady-state approximation to reduce the number of gating variables from four to one. This approach has been used previously, for example, see Cao et al. (2014); Dupont et al. (2016) and is made possible due to the rate the gating variables m_{24}, h_{24} and m_{42} reach equilibrium being so quick. The reduction in our model led to longer IPIs, higher puff amplitudes and shorter puff duration's.

Finally, we followed the steps described by Cao et al. (2014); Siekmann et al. (2019) to simplify our model further, reducing it to a two-state model. Our results were comparable with both the reduced six-state model and the results produced by Cao et al. (2014); Siekmann et al. (2019). Such results included longer IPIs and higher puff amplitudes. Siekmann et al. (2019) state that it is not the intramodal structure of the Markov model that determines the behaviour of the ion channel, but the time-dependence of the intramode transitions. This is true for the six and two-state models by Siekmann et al. (2012); Cao et al. (2013, 2014) and is also true for our models. We show that the behaviour and puff statistics between the six and two-state models based on integrodifferential equations are similar. However, one may argue the six-state models are a better representation of the activity within the cell because they simulate the frequent small fluctuations in Ca^{2+} concentration,

which we do not see in the reduced two-state model.

Whilst our models show promising results when compared to those by Cao et al. (2013), it is interesting to note their choice of parameterisation method for the Time-Dependent distribution (Cao et al., 2017). As described within Section 3.2, Thurley et al. (2011); Cao et al. (2017) set λ as the reciprocal of the mean IPI. In this chapter, we adopted this method to conduct a fair comparison between results. We found our estimate of λ, optimised using the *lsqcurvefit* function in MATLAB differed from the reciprocal of the mean IPI, specifically for the six-state and reduced two-state models. Thurley et al. (2011) state setting λ to be the reciprocal of the mean IPI enabled them to obtain excellent fits to their experimental data. Whilst this is also the case in our study, our results suggest that by not estimating λ some information about the true nature of the distribution may be lost.

We calculated activation and deactivation latencies for each model using the same step changed in Ca^{2+} concentration as in the experiments by Mak et al. (2007). Our results were obtained by running the experimental simulation 1000 times. Like the results by Cao et al. (2013), our simulations failed to capture the multi-modal distribution observed in the experimental outcomes (Mak et al., 2007). A key difference between our results from the six-state model and those by Mak et al. (2007) is that the mean activation latency for a switch in Ca^{2+} concentration from 10nM to 2µM is longer within our model. The maximum peaks in the deactivation latency distributions are similar to those in the results by Mak et al. (2007). Unlike the model results by Bicknell and Goodhill (2016), our reduced six-state and two-state models produced latency distributions that have a similar peak probability and

variation to the experimental data.

Previously, Cao et al. (2013) have investigated how the recovery rate from Ca^{2+} inhibition (known as the parameter $a_{h_{42}}$) influences the Ca^{2+} puff statistics. Their results demonstrated that increasing $a_{h_{42}}$ leads to the IPI distribution becoming exponentially distributed. This demonstrates that $a_{h_{42}}$ and thus the h_{42} gating variable are key contributors to the refractory period often seen in IPI distributions. In this thesis, we used our reduced two-state model and varied $a_{h_{42}}$ between $0.1s^{-1}$ and $5s^{-1}$. Our results, presented in Fig 3.10, were similar to those reported by Cao et al. (2013). We compared the effect increasing $a_{h_{42}}$ has on the average h_{42} gating variable in Fig 3.11. We observed that the refractory period is influenced by h_{42}. More specifically, we found that increasing the $a_{h_{42}}$ value causes h_{42} to reach a threshold value quicker. This leads to Ca^{2+} puffs being triggered sooner and a higher occurrence of Ca^{2+} puffs.

Our IP_3R model is based on the assumption that ion channels require information of past Ca^{2+} concentrations. The idea that ion channels have "memory" of past ligand concentrations is still somewhat uncommon, for example, Villalba-Galea and Chiem (2020) state that the activity of the ligand-gated receptor depends only on the current Ca^{2+} concentration of the agonist ligand. Interestingly, this statement is made in an article in which Villalba-Galea and Chiem (2020) review evidence of memory in voltage-gated ion channels. However, the experiments by Mak et al. (2007) demonstrate the dynamics of the IP_3R not only depend on the current concentration of its ligands, Ca^{2+} and IP_3, but also on the concentrations of Ca^{2+} and IP_3 that the channel is exposed to in the past.

We consider two possible explanations for the memory effect found in the data by Mak et al. (2007) and represented in the architecture of our model of the IP_3R. Firstly, the memory of the IP_3R might have emerged due to physiological necessity– the IP_3R is only capable of responding appropriately to variations in Ca^{2+} concentrations if the channel "observes" Ca^{2+} over the recent past. This view is supported by the dynamics of h_{42}, see Fig. 3.9. As long as no major increase in the Ca^{2+} concentration occurs, the gating variables h_{42} of all IP_3R s in the cluster continuously increase which makes the cluster of IP_3Rs increasingly excitable—once h_{42} has increased above a certain level, a small increase in the Ca^{2+} concentration causes a large proportion of channels to open and release Ca^{2+}, triggering a puff. In response, the gate h_{42} nearly instantaneously decreases to a value close to zero but starts to gradually increase again after the puff terminates and the Ca^{2+} concentration has returned to the resting level.

A second explanation for the memory effect is based on the biophysical basis of "sensing" the Ca^{2+} concentration in the channel's environment. Berg and Purcell (1977) suggest the cell infers the ligand concentration by, firstly, monitoring the time the ligand binds and unbinds to the receptor and secondly, by estimating the average occupancy over time, T (ten Wolde et al., 2016). When applying this to an IP_3R we suggest that rather than being able to directly "measure" the Ca^{2+} concentration, the IP_3R has to infer the ligand concentration in its environment from the interactions of the ligand with its binding sites. Thus, rather than responding to the current Ca^{2+} concentration, it is more reasonable to assume a model where the channel kinetics depends on an average Ca^{2+} concentration which can be related to

the average time that Ca^{2+} has been bound to the various binding sites of the channel for a time interval τ. Berg and Purcell (1977); ten Wolde et al. (2016) state time integration has to be performed by the signalling network downstream of the receptor proteins. This occurs when the receptor changes conformation to an active form upon sensing the specific ligands (Klipp and Liebermeister, 2006).

This chapter aimed to firstly, build a hybrid stochastic model based on integrodifferential equations. By comparing Ca^{2+} puff statistics and gating variable dynamics, we have shown our model is mathematically equivalent to the Siekmann model (Siekmann et al., 2012; Cao et al., 2013, 2014). Our model produces qualitatively and quantitatively similar results to more complex models (Cao et al., 2013, 2014). Secondly, we investigated the effect of changing the length of the delay, τ, has on the Ca^{2+} puff dynamics. Our model demonstrates the IP_3R requires "knowledge" of past ligand concentrations to produce Ca^{2+} puffs. This result is in agreement with the experimental results by Mak et al. (2007).

4 Parameterisation of mathematical model

4.1 Background

In Chapter 2 we analysed stationary single-channel data from wild-type 1 IPR and E2002D-type 1 IPR and Ca^{2+} puff data from exo 76 wild-type 1 IPR, wild-type 1 IPR and E2002D-type 1 IPR. We reviewed the different statistical distributions used to describe Ca^{2+} puff statistics and parameterised the three most commonly used statistical distributions used for describing the IPI distribution. By comparing qualitative and quantitative results, we concluded, statistically, that the Gamma distribution best describes the IPI distributions. In Chapter 3 we presented a Ca^{2+} puff model based on integrodifferential equations. Whilst our model is mathematically equivalent to previous Ca^{2+} puff models (Cao et al., 2013), it has the advantage of enabling us to investigate the effect changing the length of the delay in the IP_3R *recognising* a change in Ca^{2+} concentration has on Ca^{2+} puff dynamics. In this chapter, we bring together Chapters 2 - 3 and present two Ca^{2+} puff models that have been parameterised using the experimental data by Arige et al. (2022). We use the stationary single-channel data to parameterise our single IP_3R model, build an IP_3R cluster model to simulate Ca^{2+} puff traces and compare our results with the Ca^{2+} puff results from Arige et al. (2022). This

chapter aims to firstly, parameterise our model to simulate Ca^{2+} traces that are an accurate representation of the experimental data. Secondly, we aim to provide insight into the underlying Ca^{2+} signalling system by comparing model results for a wild-type 1 IPR and a wild-type 1 IPR in which the 2002 glutamic acid residue has been substituted with aspartate.

4.1.1 Parameterising IP_3R models using experimental data

Stationary single-channel data

Siekmann et al. (2019) state that incorporating ligand-dependent open probabilities, stationary single-channel data, modal gating and latency data into mathematical IP_3R models leads to a more accurate biological representation; models not parameterised through fitting experimental data are unable to reproduce the statistical properties of IP_3R kinetics (Siekmann et al., 2012). Furthermore, studies have shown that models need to be built specific to the dynamics of the IP_3R, and simply fitting experimental data to any IP_3R model does not always yield the desired results (Sneyd et al., 2004; Hituri and Linne, 2013). Sneyd et al. (2004) parameterised three IP_3R models using the same stationary single-channel data. When comparing their results, Sneyd et al. (2004) found parameters for two models were not well defined by the data - steady-state curves were shaped differently to the experimental data and step increases in Ca^{2+} were too quick (Siekmann et al., 2019). A similar result was present in a model simulation by Gin et al. (2009), who used a four-state IP_3R model based on stationary single-channel measurements. Their model could not simulate the long recovery latency time described by

Mak et al. (2007). Siekmann et al. (2012) incorporated stationary single-channel data by Wagner and Yule (2012) into their six-state Markov model. Whilst their model was able to accurately describe switching between fast and slow activity of the IP_3R, it could not be used to produce Ca^{2+} puffs.

Relying solely on stationary single-channel data has proven to be insufficient in providing an accurate depiction of the IP_3R dynamics. The introduction of kinetic single-channel data by Mak et al. (2007) into IP_3R models improved results, producing both accurate IP_3R dynamics and Ca^{2+} puffs (Cao et al., 2013). Ullah et al. (2012a) use stationary single-channel data from Sf9 insect cells and latency data from Mak et al. (2007) to model IP_3R behaviour. Similarly, the incorporation of kinetic single-channel data by Mak et al. (2007) enabled Cao et al. (2013) to improve the Siekmann model (Siekmann et al., 2012) to account for the latency in the IP_3R opening. Hituri and Linne (2013) state the development of new IP_3R models require both stationary and kinetic experimental data. Results by Ullah et al. (2012a); Cao et al. (2013) show this is the case.

Ca^{2+} puff data

Whilst single-channel data strengthens IP_3R models, insight into how key parameters affect the Ca^{2+} dynamics is important to successfully simulate Ca^{2+} puffs. Prior studies have analysed how the occurrence of Ca^{2+} puffs changes depending on factors such as IP_3 concentration, IP_3R cluster size, resting Ca^{2+} concentration and the recovery rate from Ca^{2+} inhibition (Shuai et al., 2006; Dickinson et al., 2012; Ullah et al., 2012b; Qi et al., 2014; Rückl et al., 2015; Cao et al., 2017).

Shuai et al. (2006) investigated the effect of changing the number of open channels, the diameter of the cluster, Ca^{2+} current and properties of fluorescent dye on the Ca^{2+} blips and puffs simulated using their deterministic spatial model. They spaced their IP_3R on a square plane of length, L. Their research aimed to model experimental data of Xenopus Oocytes. By varying both the number of open channels during a puff and L, the width of the square plane, Shuai et al. (2006) attempted to match their simulated results to the experimental data. They found that when the number of open IP_3R was 25 and L was 520nM their simulations matched the experimental data. Shuai et al. (2006) study focuses on the number of open ion channels during a Ca^{2+} puff and not the total number in a cluster, therefore the number of IP_3R in a cluster could be much larger.

Similarly, Dickinson et al. (2012) investigated how ion channel cluster size affects Ca^{2+} puff kinetics when modelling Ca^{2+} puffs using experimental data from SH-SY5Y cells. The ion channel cluster size was estimated using the largest Ca^{2+} puff. The number of channels open during a Ca^{2+} puff is calculated by dividing the peak fluorescence amplitude by that of a single Ca^{2+} blip. Dickinson et al. (2012) note this approach to estimating the cluster size may cause inaccuracies, such as the largest Ca^{2+} puff being missed due to the sample size. The mean IPI and reciprocal of the cluster size are shown to follow a linearly increasing relationship.

Using a four-state single channel model, Ullah et al. (2012b) investigated the dynamics of Ca^{2+} blips and puffs. Like Dickinson et al. (2012), Ullah et al. (2012b) assume that the maximum amplitude observed at a given puff site represents the number of IP_3R in a cluster. Ullah et al. (2012b) state their

model suggests Ca^{2+} puffs terminate because of self-inhibition. Increasing the mean transition time from an open state to an inactive state reduces the probability of the IP_3R becoming inhibited and thus delays Ca^{2+} puff termination.

Qi et al. (2014) used a modified De-Young Keizer model to study how the IP_3 concentration, IP_3R cluster size and resting Ca^{2+} concentration affect the Ca^{2+} blip and puff frequency. When the IP_3 concentration was small (0.01µM) their model simulated a higher frequency of Ca^{2+} blips compared to the number of Ca^{2+} puffs. This result was unanimous for all IP_3R cluster sizes. However, for a larger IP_3 concentration (2 µM) and a large cluster size, the puff frequency increased more than the blip frequency. The cause for this is that more channels can bind to IP_3 when the concentration is higher, therefore more channels are subsequently able to open. For the second part of their study, Qi et al. (2014) kept the IP_3 concentration constant and analysed the effect increasing the resting Ca^{2+} concentration has on Ca^{2+} blip and puff frequency. As the resting Ca^{2+} concentration increases, the frequency of blips and puffs increases due to there being more Ca^{2+} able to bind to the activating sites of the IP_3R. Rückl et al. (2015) found a similar result when investigating how different IP_3 concentrations affect Ca^{2+} puff dynamics using their hybrid stochastic system. Their results showed that as the IP_3 concentration increased, the Ca^{2+} puff amplitudes and durations increased.

Similarly, Cao et al. (2017) studied how changing the IP_3 concentration affects Ca^{2+} puff statistics, focusing specifically on the IPI and amplitude distributions. They also explored changes to the basal level of an inhibitory

gating variable. Their study found a high IP_3 concentration and low basal level simulated Ca^{2+} puff traces with a lower amplitude compared to simulations when the IP_3 concentration was low and basal level was high. In Chapter 3 of this thesis, we showed the IP_3R does not produce Ca^{2+} puffs when the length of the delay, τ, is short and the basal level of the inhibitory gating variable effects the frequency of Ca^{2+} puffs.

Prior studies have shown single channel models successfully produce the correct IP_3R dynamics when parameterised using stationary and kinetic experimental data (Ullah et al., 2012a; Cao et al., 2013, 2014). In this chapter, we parameterise our hybrid stochastic system using stationary single-channel and Ca^{2+} puff data by Arige et al. (2022). This research has the aim of providing a mathematical insight into the complexity of the Ca^{2+} signalling system. Abnormal IP_3R have been shown to have devastating consequences on individuals, therefore by understanding the change in mechanisms that may cause these mutations mathematically, one may be able to gain better insight into the biological interactions.

4.1.2 Chapter Aims

- **Build two two-state Markov models based on patch clamp data from wild-type 1 IPR and E2002D-type 1 IPR**

  Using stationary single channel data (Arige et al., 2022), we build a two-state IP_3R model for wild type and mutated IP_3R. Average open and closed dwell times and open probabilities are used to parameterise the rates of the two-state models. Latency distributions will be compared to the results by Mak et al. (2007).

- **Build an IP_3R cluster model that produces comparable results to the experimental data**

  Using the single-channel models, we build an IP_3R cluster model. To ensure agreement between model simulations and the experimental data presented in Chapter 2, we compare Ca^{2+} puff statistics.

- **Compare differences between the wild-type 1 IPR and E2002D-type 1 IPR models**

  We discuss how the parameter changes to the wild type IP_3R model lead to a model that simulates Ca^{2+} dynamics similar to those produced by E2002D-type 1 IPR.

4.2 Methods

4.2.1 Mathematical model

IP_3R model

We use a two-state Markov model, shown in Fig 4.1, to simulate the single channel and Ca^{2+} dynamics. Transition rates are Ca^{2+} / IP_3 dependent and include a delay term, τ. Our model does not account for mode changes in the IP_3R activity. The rate parameters $q_{oc}(\bar{c}(t))$ and $q_{co}(\bar{c}(t))$, shown in Eq 4.1-4.2, are calculated using two gating variables each, m_{oc}, h_{oc}, m_{co}, h_{co}, and parameterised using stationary single-channel data.

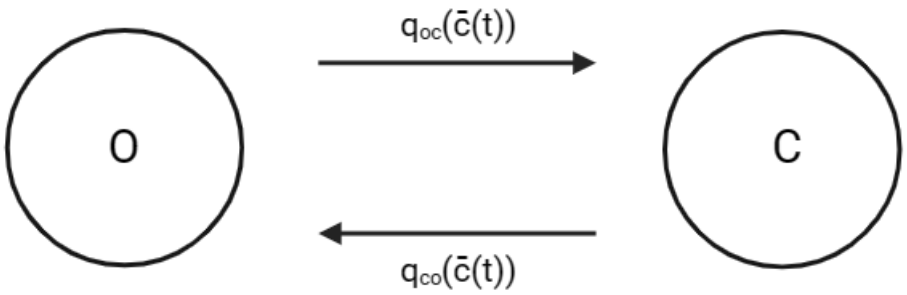

Figure 4.1: Two-state Markov model

$$q_{oc(\bar{c}(t))} = a_{oc} + V_{oc}(1 - m_{oc}h_{oc}) \tag{4.1}$$

$$q_{co(\bar{c}(t))} = a_{co} + V_{co}m_{co}h_{co} \tag{4.2}$$

The parameters a_{oc}, a_{co}, V_{oc} and V_{co} are constant. The rates m_{oc}, h_{oc} and m_{co} are assumed to reach equilibrium immediately.

That is:

$$m_{oc} = m_{oc\infty} = \frac{c^{n_{oc}}}{c^{n_{oc}} + k_{oc}^{n_{oc}}} \tag{4.3}$$

$$h_{co} = h_{oc\infty} = \frac{k_{-oc}^{n_{-oc}}}{c^{n_{-oc}} + k_{-oc}^{n_{-oc}}} \tag{4.4}$$

$$m_{co} = m_{co\infty} = \frac{c^{n_{co}}}{c^{n_{co}} + k_{co}^{n_{co}}} \tag{4.5}$$

h_{co} follows a different dynamic to the other gating variables and reaches equilibrium on a slower timescale (Cao et al., 2013). Chapter 3 showed h_{co} can be written as an integral term, which is interpreted as an average over past Ca^{2+} concentrations of length τ. This integral term is described in Eq 4.6 (Hodgkin and Huxley, 1952; Brady, 1970; Cao et al., 2013; Hawker et al., 2024).

$$\Phi_{h_{co}}(t, c) = h_{co\infty} \exp\left[-\int_{t-\tau}^{t} (\lambda_{h_{co}} \circ c)(x)dx\right] - \exp\left[-\int_{t-\tau}^{t} (\lambda_{h_{co}} \circ c)(x)dx\right] \int_{t-\tau}^{t} (-\alpha_{h_{co}} \circ c)(s) \quad \exp\left[\int_{s-\tau}^{s} (\lambda_{h_{co}} \circ c)(x)dx\right] ds \tag{4.6}$$

Where c represents the Ca^{2+} concentration.

The initial values are: $t_0 = 0$, $c(t_0) = 0.1$ µM. $h_{co\infty}$, h_{co} at equilibrium, and $\lambda_{h_{co}}$, the rate at which equilibrium is reached, are calculated as follows:

$$h_{co\infty} = \frac{k_{-co}^{n_{-co}}}{c^{n_{-co}} + k_{-co}^{n_{-co}}} \tag{4.7}$$

$$\lambda_{h_{co}} = a_{h_{co}} + \frac{V_{h_{co}} c^7}{c^7 + 20^7} \tag{4.8}$$

Where $a_{h_{co}}$ and $V_{h_{co}}$ are constants.

$\alpha_{h_{co}}$ is calculated as follows:

$$\alpha_{h_{co}} = \lambda_{h_{co}} h_{co\infty} \tag{4.9}$$

Steady state transition rates for $q_{oc}(\bar{c}(t))$ and $q_{co}(\bar{c}(t))$ are thus:

$$q_{oc\infty} = a_{oc} + V_{oc}(1 - m_{oc\infty} h_{oc\infty}) \tag{4.10}$$

$$q_{co\infty} = a_{co} + V_{co} m_{co\infty} h_{co\infty} \tag{4.11}$$

$q_{oc\infty}$ and $q_{co\infty}$ are parameterised using stationary single-channel data by Arige et al. (2022). This is achieved by calculating the mean open ($\bar{o_d}$) and closed ($\bar{c_d}$) dwell times of a single IP_3R at different constant Ca^{2+} concentrations and fitting $q_{oc\infty}$ and $q_{co\infty}$ to the inverse of these results. That is, $q_{oc\infty} = \frac{1}{\bar{o_d}}$ and $q_{co\infty} = \frac{1}{\bar{c_d}}$. We use MATLAB's *lsqnonlin* function to fit $q_{oc\infty}$ and $q_{co\infty}$ to the mean dwell times. Lower boundaries were set to ensure parameters estimated were positive and greater than 0. The open probability (P_o) is calculated as $\frac{q_{co\infty}}{q_{co\infty}+q_{oc\infty}}$. P_o is gathered from the experimental data by calculating the ratio of open to closed events. The transition rates and P_o at differing Ca^{2+} concentrations for both models are presented in Table 4.1

Latency distributions

We simulate activation and deactivation latencies using our two-state model described in Section 4.2.1. We replicate the experimental conditions by Mak et al. (2007) and compare our results for the wild-type 1 IPR and E2002D-type 1 IPR. Simulations are repeated 1000 times.

Table 4.1: Transition rates and P_o for the wild-type 1 IPR and E2002D-type 1 IPR models

Ca^{2+} (nM)	Wild-type 1 IPR			E2002D-type 1 IPR		
	$q_{oc\infty}(s^{-1})$	$q_{co\infty}(s^{-1})$	P_o	$q_{oc\infty}$	$q_{co\infty}$	P_o
10	-	-	0	-	-	0
50	2.009	0.3933	0.1627	0.8527	0.1313	0.1305
200	0.9749	4.4678	0.8208	1.0773	1.0655	0.4948
1000	1.7389	5.6471	0.7645	1.0155	0.9006	0.4638
3000	1.5654	0.6536	0.2937	1.0903	0.3319	0.2259
100 000	-	-	0	-	-	0

Deterministic calcium dynamics

We use the same system of ODES presented in Chapter 3 (Cao et al., 2013), to simulate the fluxes that influence the Ca^{2+} concentration, c, in the cytosol as well as the Ca^{2+} dye, b_{fluo4}.

$$\frac{dc}{dt} = J_{\text{increase}}N_o + J_{\text{leak}} - J_{\text{decrease}} - k_{\text{on}}(B_{\text{fluo4}} - b_{\text{fluo4}})c + k_{\text{off}}b_{\text{fluo4}} \tag{4.12}$$

$$\frac{db_{\text{fluo4}}}{dt} = k_{\text{on}}(B_{\text{fluo4}} - b_{\text{fluo4}})c - k_{\text{off}}b_{\text{fluo4}} \tag{4.13}$$

Parameter values for each model are detailed in Table 4.2.

Calcium puff statistics

We compare the Ca^{2+} puff statistics gathered from our Ca^{2+} trace with those from the experimental data (see Chapter 2 for details). Due to the stochastic nature of the biological process, there will be differences between the data sets. However, a comparison of key statistical metrics enables us to determine how well our model compares to the experimental data. Short

Table 4.2: Wild-type 1 IPR and E2002D-type 1 IPR model parameters. IP_3-dependent parameters are evaluated at a concentration of 1 µM as indicated by subscripts. Full model details are given in Cao et al. (2013).

Symbol	Description	Wild-type 1 IPR	E2002D-type 1 IPR	Units
	Gating kinetics			
a_{oc}	Basal level of q_{oc}	$1.21_{p=1\mu M}$	$0.11_{\ p=1\mu M}$	s^{-1}
V_{oc}	Gating-dependent part of q_{oc}	$55.29_{p=1\mu M}$	$37.99_{\ p=1\mu M}$	s^{-1}
a_{co}	Basal level of q_{co}	$0.02_{p=1\mu M}$	$0.0024_{p=1\mu M}$	s^{-1}
V_{co}	Gating-dependent part of q_{co}	12.5	62.14	s^{-1}
n_{-oc}	Hill coefficient for Ca^{2+} dependency of $h_{oc\infty}$	0.35	1	
k_{-oc}	Half-saturation constant for Ca^{2+} dependency of $h_{oc\infty}$	$0.952_{p=1\mu M}$	$0.009_{p=1\mu M}$	
$h_{oc\infty}$	Steady state of h_{oc}	$\frac{k_{-oc}^{n_{-oc}}}{c^{n_{-oc}}+k_{-oc}^{n_{-oc}}}$	$\frac{k_{-oc}^{n_{-oc}}}{c^{n_{-oc}}+k_{-oc}^{n_{-oc}}}$	
$a_{h_{co}}$	Basal level of $\lambda_{h_{co}}$ (tuning parameter)	0.5	0.5	s^{-1}
$V_{h_{co}}$	Ca^{2+}-dependent part of $\lambda_{h_{co}}$	100	100	s^{-1}
$K_{h_{co}}$	Half-saturation constant for Ca^{2+}-dependency of $\lambda_{h_{co}}$	20	20	µM
$\lambda_{h_{co}}$	Rate of approach to steady state of h_{co}	$a_{h_{co}}+\frac{V_{h_{co}}c^7}{c^7+K_{h_{co}}^7}$	$a_{h_{co}}+\frac{V_{h_{co}}c^7}{c^7+K_{h_{co}}^7}$	s^{-1}
n_{-co}	Hill coefficient for Ca^{2+} dependency of $h_{co\infty}$	3	3	
k_{-co}	Half-saturation constant for Ca^{2+} dependency of $h_{co\infty}$	$0.17_{p=1\mu M}$	$0.17_{p=1\mu M}$	
$h_{co\infty}$	Steady state of h_{co}	$\frac{k_{-co}^{n_{-co}}}{c^{n_{-co}}+k_{-co}^{n_{-co}}}$	$\frac{k_{-co}^{n_{-co}}}{c^{n_{-co}}+k_{-co}^{n_{-co}}}$	
n_{oc}	Hill coefficient for Ca^{2+} dependency of $m_{oc\infty}$	10	10	
k_{oc}	Half-saturation constant for Ca^{2+} dependency of $m_{oc\infty}$	$0.11_{p=1\mu M}$	$0.012_{p=1\mu M}$	
$m_{oc\infty}$	Steady state of m_{oc}	$\frac{c^{n_{oc}}}{c^{n_{oc}}+k_{oc}^{n_{oc}}}$	$\frac{c^{n_{oc}}}{c^{n_{oc}}+k_{oc}^{n_{oc}}}$	
n_{co}	Hill coefficient for Ca^{2+} dependency of $m_{co\infty}$	2	2	
k_{co}	Half-saturation constant for Ca^{2+} dependency of $m_{co\infty}$	$0.718_{p=1\mu M}$	$4.128_{p=1\mu M}$	
$m_{co\infty}$	Steady state of m_{co}	$\frac{c^{n_{co}}}{c^{n_{co}}+k_{co}^{n_{co}}}$	$\frac{c^{n_{co}}}{c^{n_{co}}+k_{co}^{n_{co}}}$	
	Ca^{2+} balance			
c_h	Elevated Ca^{2+} in vicinity of open IP_3R channel	120	120	µM
B	Total buffer concentration	20	20	µM
k_{on}	Binding of fluo4 buffer to Ca^{2+}	150	150	$\mu M s^{-1}$
k_{off}	Unbinding of fluo4 buffer from Ca^{2+}	300	300	s^{-1}
J_r	Flux of Ca^{2+} through single channel	200	200	$\mu M s^{-1}$
J_{leak}	Ca^{2+} influx from cluster environment	33	33	$\mu M s^{-1}$
V_d	Rate of cytoplasmic Ca^{2+} removal from the cluster	4000	4000	µM s^{-1}
K_d	Half-saturation constant for cytoplasmic Ca^{2+} removal	12	12	µM

experimental study time and inactive IP_3R can lead to a limited data set. To overcome this, one can pool the experimental data. We compare our IPI distributions and those from the pooled experimental results by analysing key statistical metrics, histograms and parameter values from the Gamma distribution. Violin plots are used to compare the spread of the data and the density of the distributions. We compare the experimental data with multiple simulations of the same length. This enables us to ensure agreement between the mathematically modelled Ca^{2+} puff data and the experimental data.

Numerical methods

We solve Eq (4.12), (4.13) using the fourth-order Runge-Kutta method. A hybrid Gillespie algorithm is used to simulate the Markov models representing the IP_3R channels (Alfonsi et al., 2005; Cao et al., 2013; Rüdiger, 2013). A maximum time step size of 10^{-4}s is used. Integrals in Eq (4.6) are calculated using the Riemann Sum, using a larger time step (10^{-2}s). Alternative methods of numerical integration, such as adaptive quadrature, Simpson's rule and the trapezoidal rule, were tested when computing the integrals in our model. However, the Riemann Sum method produced similar results under a small time-step of 10^{-2}s and was less computationally challenging. IP_3 is set to 1µM for all simulations, replicating the experimental conditions by Arige et al. (2022). We assume Ca^{2+} concentrations prior to time t_0 are constant and low at 0.1µM. τ is set to 3s. Ca^{2+} traces are run for a simulation time of 400s. All results were gathered using MATLAB (MathWorks, Natick, MA).

4.3 Results

4.3.1 Single channel

Fig 4.2 shows the steady state transition rates and P_o curves fit to the wild-type 1 IPR and E2002D-type 1 IPR experimental data by Arige et al. (2022). Due to the IP_3R being consistently closed when the Ca^{2+} concentration was 10nM and 100µM transition rates could not be calculated. The fit of our curves suggests these rates are high for $q_{oc\infty}$ and low for $q_{co\infty}$. Steady-state transition rates for wild-type 1 IPR are faster than the E2002D-type 1 IPR. Whilst the wild-type 1 IPR appears to respond to different Ca^{2+} concentrations, shown by the decrease in $q_{oc\infty}$ when the Ca^{2+} concentration is 200nM, the E2002D-type 1 IPR does not. This suggests that the E2002D mutation causes the IP_3R to be less responsive to Ca^{2+} concentrations between 200nM and 3µM. For both the wild-type 1 IPR and E2002D-type 1 IPR, $q_{co\infty}$ follows a bell shaped curve, peaking between 200nM and 1µM. However, $q_{co\infty}$ for the E2002D IP_3R are slower. The slower transition rates for both $q_{oc\infty}$ and $q_{co\infty}$ along with the lack of Ca^{2+} sensitivity will lead to the E2002D-type 1 IPR being less responsive. Whilst $q_{co\infty}$ fits well to the experimental data, it is evident in Fig 4.2 that $q_{oc\infty}$ does not. $q_{oc\infty}$ cannot model the decrease in the transition rate observed in the E2002D-type 1 IPR data and only fits well to two data points in the wild-type 1 IPR data.

The E2002D-type 1 IPR has a smaller P_o than the wild-type 1 IPR, consistent with experimental data. The maximum P_o reached by the E2002D curve is 0.56 compared with 0.83 for the wild-type 1 IPR curve when IP_3 is held constant at 10µM. The E2002D-type 1 IPR appears to be most greatly

effected for Ca^{2+} concentrations between 200nM and 3µM. By basing our IP_3R model on the work of Cao et al. (2013), our transition rates include an IP_3 dependency. This allows us to simulate P_o for different IP_3 concentrations. In Fig 4.2, we present P_o for the wild-type 1 IPR and E2002D-type 1 IPR models when the IP_3 concentration is 1µM. A maximum P_o reached by the wild-type 1 IPR curve is 0.017 and 0.002 by the E2002D-type 1 IPR curve.

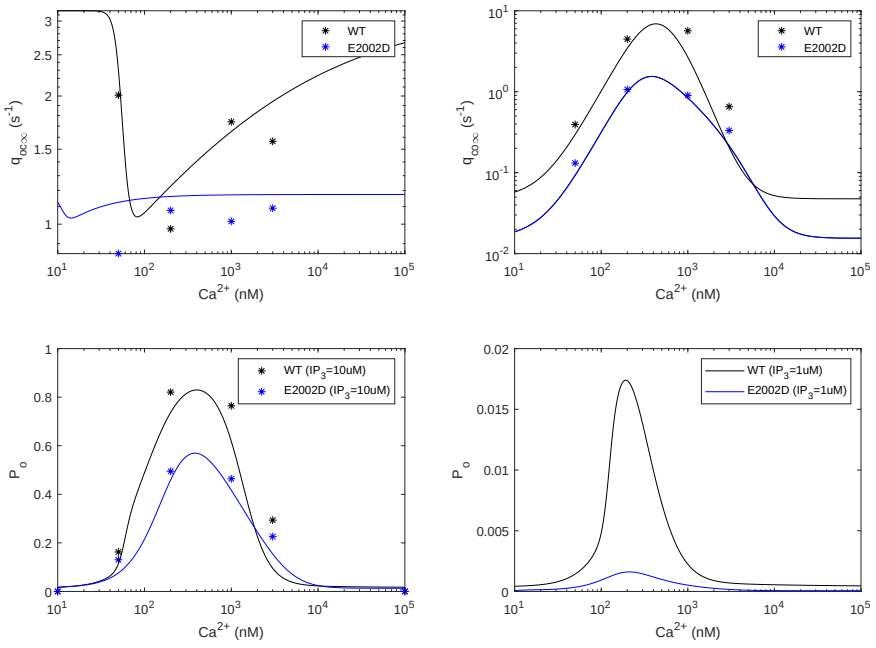

Figure 4.2: Transition rate and open probability curves for the wild-type 1 IPR and E2002D-type 1 IPR (Arige et al., 2022). Curves are fit using Eq 4.1-4.2 at their steady state using parameters from Table 4.2.

4.3.2 Latency distributions

The latency distributions for the wild-type 1 IPR, E2002D-type 1 IPR and Mak et al. (2007) data can be observed in Fig 4.3. We replicate the ex-

perimental study by Mak et al. (2007) by switching the Ca^{2+} concentration between low (10nM), intermediate (2µM) and high (300µM). Our latency distributions are log-transformed and compared to the results by Mak et al. (2007), presented on the right in Fig 4.3. The maximum peak activation latency for the wild-type 1 IPR is 0.19s when responding to a step change in Ca^{2+} concentration from 10nM to 2µM in comparison to the faster response of the E2002D (0.008s). The maximum peak activation latency for a step change from 300µM to 2µM was the same for both IP_3R types (3s). When responding to a step change in Ca^{2+} concentration from 2µM to 10nM and 2µM maximum peak deactivation latencies from the E2002D-type 1 IPR were longer than those from the wild-type 1 IPR at 0.75s and 0.57s in comparison to 0.21s and 0.33s, respectively.

4.3.3 Ca^{2+} puffs

Fig 4.4 presents the Ca^{2+} trace using our parameterised IP_3R cluster models. Our models produce Ca^{2+} puffs of the desired shape i.e. the high increase in Ca^{2+} concentration, from the opening of several IP_3R, followed by a staggered decrease in the Ca^{2+} concentration as the IP_3Rs close. The wild-type 1 IPR is more active than the E2002D-type 1 IPR evidenced by the continual fluctuations in Ca^{2+} concentration. The E2002D-type 1 IPR has longer intervals and spends more time at the resting Ca^{2+} concentration. Alongside the more frequent openings of the wild-type 1 IPR, more channels open during Ca^{2+} events, with a maximum of 5 IP_3R opening during a Ca^{2+} puff in comparison to 3 from the E2002D-type 1 IPR model.

In Fig 4.5 we compare the behaviour of the gating variables for the wild-

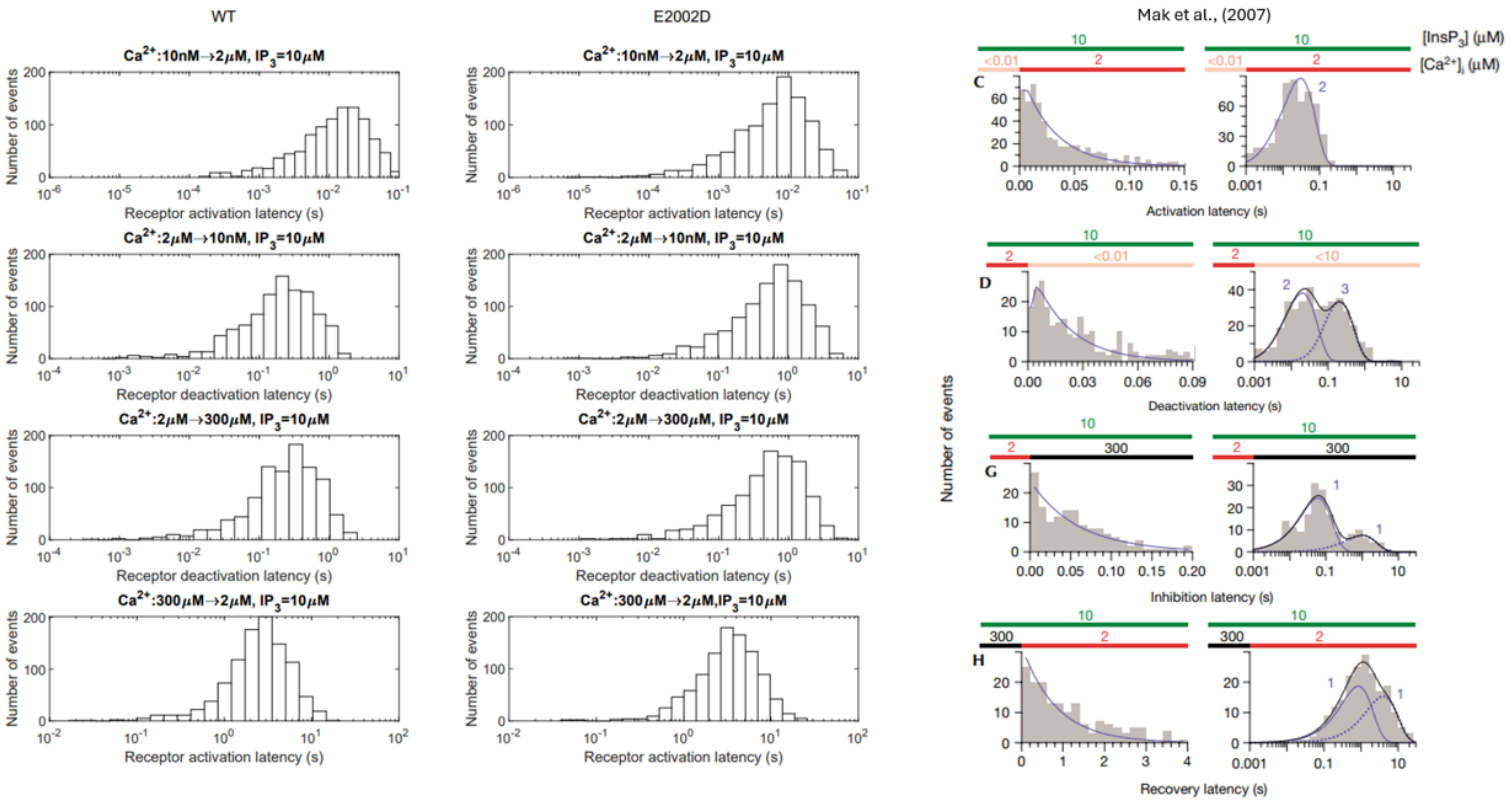

Figure 4.3: Simulated latency distributions for the wild-type 1 IPR and E2002D-type 1 IPR models compared to the experimental results by Mak et al. (2007). IP_3=10μM. Permission to reproduce the image by Mak et al. (2007) has been granted by Professor Kevin Foskett, University of Pennsylvania, and is covered under a License Agreement between the author and Copyright Clearance Center, Inc. on behalf of the Rightsholder (Springer Nature BV).

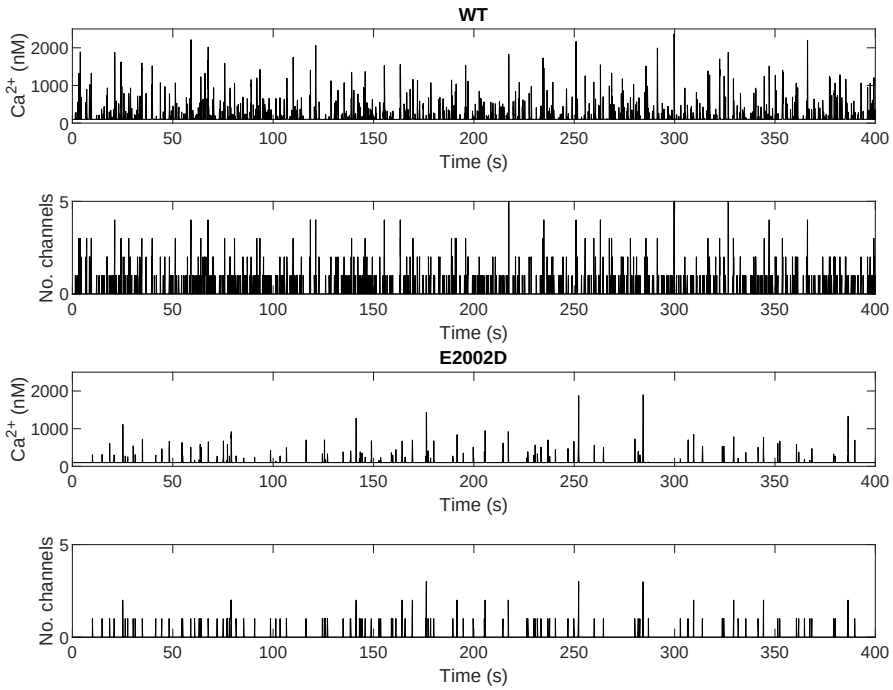

Figure 4.4: Example of Ca^{2+} trace produced by the wild-type 1 IPR and E2002D-type 1 IPR models.

type 1 IPR and E2002D-type 1 IPR models. We use the average of the gating variable values over the entire IP_3R cluster. Due to us making a quasi-steady-state approximation, m_{oc}, h_{oc} and m_{co} go immediately to steady state, whereas h_{co} relies on past Ca^{2+} concentrations. A key difference between the gating variable dynamics for the wild-type 1 IPR and E2002D-type 1 IPR models is that m_{oc} and h_{oc} do not respond as significantly to changes in Ca^{2+} concentrations for the E2002D-type 1 IPR. Furthermore, whilst m_{co} does respond to a change in Ca^{2+} concentration for the E2002D-type 1 IPR it is not as great as the wild-type 1 IPR. m_{co} can be interpreted as controlling the opening of IP_3R, therefore this lack of response from the m_{co} E2002D-type 1 IPR gating variable will cause fewer IP_3R to open. h_{co} can be seen to fluctuate for both the wild-type 1 IPR and E2002D-type 1 IPR models. This is because h_{co} depends on Ca^{2+} concentrations from the previous 3s, and we compute the average of h_{co} across the entire cluster.

In Fig 4.6 we compare Ca^{2+} puff statistics from our models with the pooled experimental data. The IPI distribution for the experimental and simulated data of wild-type 1 IPR are in good agreement. Both distributions appear to be exponentially distributed. In contrast the IPI distributions for the E2002D-type 1 IPR experimental and simulated data are dissimilar. The experimental IPI distribution is exponentially distributed whereas the simulated IPI data fits to a Gamma distribution. A possible reason for discrepancies between the E2002D-type 1 IPR experimental and simulated IPI data could be the difference in their data point counts. Our wild-type 1 IPR simulated amplitudes are in good agreement with the experimental data. Both data sets show a high proportion of short Ca^{2+} puffs. Our

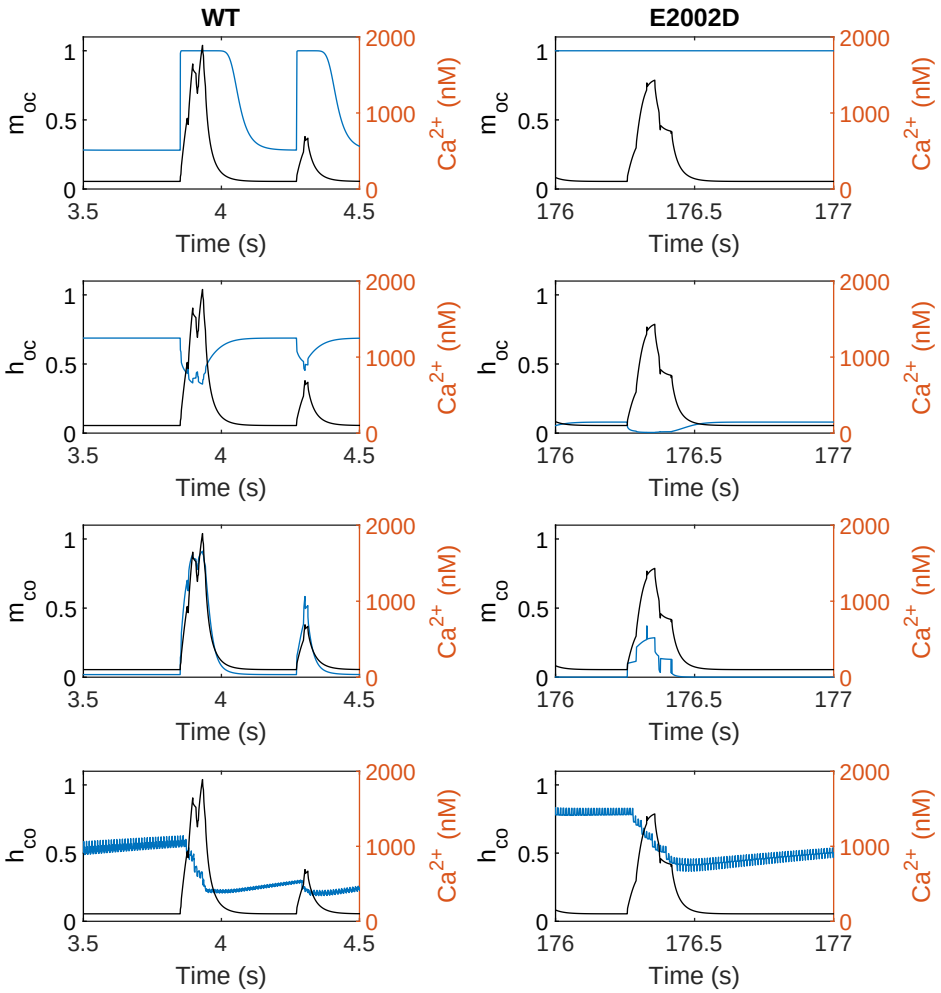

Figure 4.5: Comparison of gating variable behaviour in response to Ca^{2+} puffs produced by the wild-type 1 IPR and E2002D-type 1 IPR Ca^{2+} puff models. The average gating variable value is shown in blue and the Ca^{2+} concentration is shown in black.

model did not simulate the larger Ca^{2+} puffs seen within the experimental data. Our E2002D-type 1 IPR model simulated Ca^{2+} puffs that have a similar variance to the experimental data. However, whilst our Ca^{2+} puff amplitude distribution has a very distinct peak, the experimental data does not. The wild-type 1 IPR experimental and simulated duration distributions are skewed to the right. The duration distribution from the experimental data shows a very dominant peak in density. Durations simulated using our wild-type 1 IPR model show a peak in a similar region with a lower density. This result is also seen in the E2002D-type 1 IPR duration data. The experimental duration distribution has a peak at ≈ 0.075s and a small variation. Whilst our E2002D-type 1 IPR duration distribution peaks in a similar area as the experimental data, the variability of the data is much larger. Full summary statistics for the Ca^{2+} puff statistics are presented in Table 4.3.

The simulated and experimental wild-type 1 IPR IPI distributions are exponentially distributed, evidencing at the high frequency of Ca^{2+} puff events. The wild-type 1 IPR data has a higher IPI mean (1.25s) compared to the simulated IPIs (0.72s). Median IPIs are closer in comparison. The maximum IPI from the wild-type 1 IPR experimental data is over two times greater than the maximum IPI simulated from our model. When considering the IPI distribution for the E2002D-type 1 IPR experimental data we see two groups of data. However, the cause for this may be the small data set. The mean IPI from the E2002D-type 1 IPR model is higher than that from the experimental data (3.65s compared to 1.93s). This value will be skewed by the higher IPIs in our model. Although the time between Ca^{2+} puffs is often

longer in our model, if the experiments were conducted for longer periods we would expect longer IPIs. Whilst the IPI distribution for the E2002D-type 1 IPR experimental data is exponentially distributed, the results from our simulation are not.

The wild-type 1 IPR and E2002D-type 1 IPR produce Ca^{2+} puffs of a low amplitude. The median Ca^{2+} puff amplitude for our wild-type 1 IPR model (437.53nM) is larger than the experimental data (348.69nM). However, the mean Ca^{2+} puff amplitude is smaller (583.41nM) compared to the experimental data (740.89nM). The maximum Ca^{2+} puff amplitude for the experimental data is greater than the simulated results (10 668.58nM compared to 2370.27nM). Ca^{2+} puff amplitudes produced by the E2002D-type 1 IPR model fall within a similar range to the experimental data. Whilst the median and mean Ca^{2+} puff amplitude is smaller for the model results compared to the experimental data (467.78nM and 527.93nM compared to 624.42nM and 655.58nM, respectively), the maximum Ca^{2+} puff amplitude is similar (1899.66nM compared to 1908.57nM).

Ca^{2+} puff durations are often very short with the wild-type 1 IPR and E2002D-type 1 IPR experimental data having a mean of 0.09s and 0.07s, respectively. Our models are able to produce similar Ca^{2+} puff duration's, with means of 0.12s and 0.11s. Furthermore, the wild-type 1 IPR experimental data has longer Ca^{2+} puff durations with a maximum of 0.48s. Our wild-type 1 IPR model produces a maximum duration of 0.4s. The maximum Ca^{2+} puff duration from the E2002D-type 1 IPR data is shorter than that produced by our E2002D-type 1 IPR model, 0.16s compared to 0.31s.

In Fig 4.7 we present violin plots used to compare the distribution shape

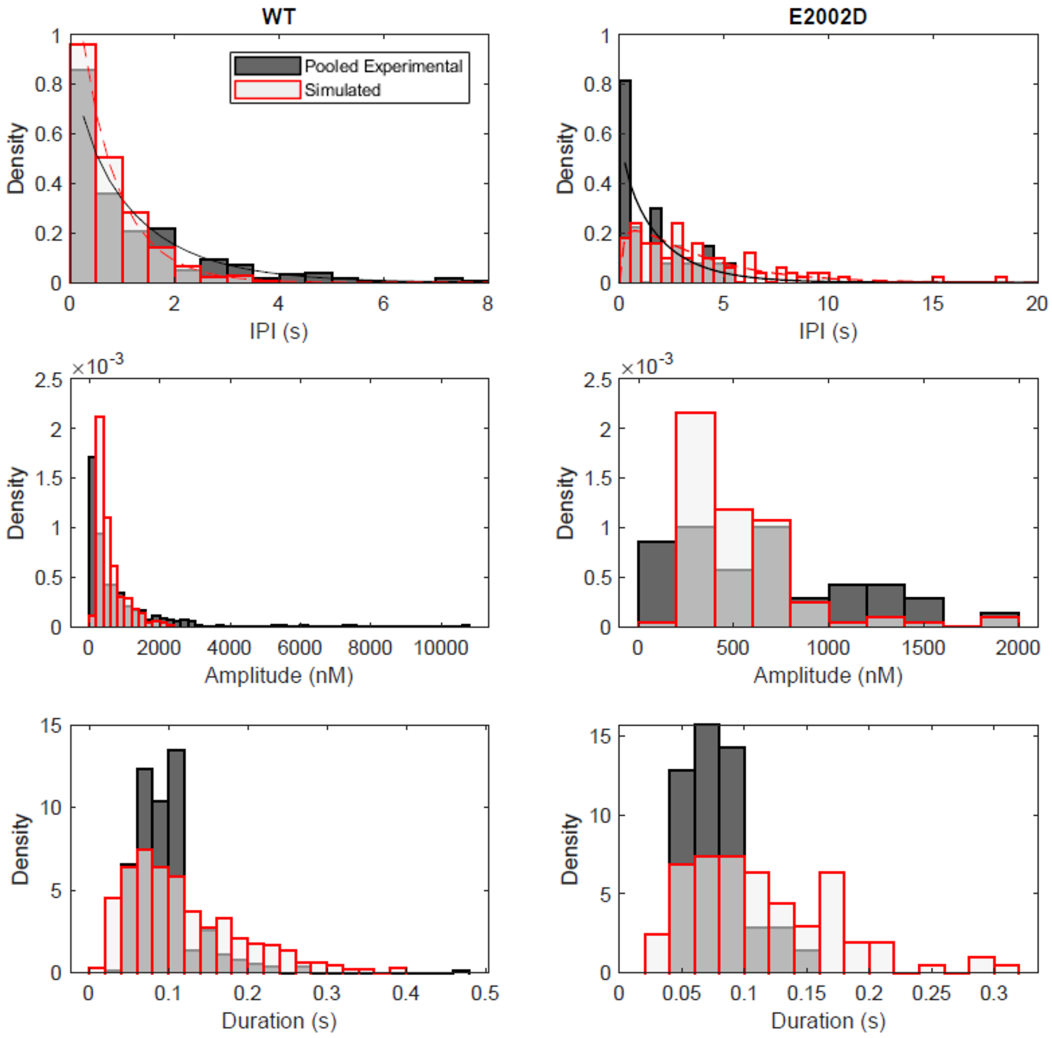

Figure 4.6: Comparison of simulated Ca^{2+} puff statistics and pooled experimental data by Arige et al. (2022).

Table 4.3: Comparison of Ca^{2+} puff summary statistics gathered from the wild-type 1 IPR and E2002D-type 1 IPR models and experimental data

IP_3R	Statistical metric	Simulated			Pooled Experimental		
		IPI (s)	Amplitude (nM)	Duration (s)	IPI (s)	Amplitude (nM)	Duration (s)
Wild-type 1 IPR	Min	< 0.001	193.29	0.02	0.02	14.77	0.02
	Q1	0.22	284.69	0.06	0.32	157.64	0.06
	Median	0.54	437.53	0.1	0.68	348.69	0.08
	Mean	0.72	583.41	0.12	1.25	740.89	0.09
	Q3	1.07	710.20	0.16	1.64	938.54	0.1
	Max	3.91	2370.27	0.40	10.06	10668.58	0.48
E2002D-type 1 IPR	Min	0.04	197.62	0.02	0.02	61.69	0.04
	Q1	1.17	302.60	0.06	0.41	248.99	0.05
	Median	2.96	467.78	0.10	1.8	624.42	0.06
	Mean	3.65	527.93	0.11	1.93	655.58	0.07
	Q3	4.79	669.93	0.15	3.24	987.55	0.08
	Max	18.34	1899.66	0.31	5.44	1908.57	0.16

Table 4.4: Comparison of parameters for the Gamma distribution

IP_3R	Simulated		Experimental	
	α	β	α	β
Wild-type 1 IPR	0.9595	1.3287	0.8728	2.3288
E2002D-type 1 IPR	1.2492	0.3427	0.8931	0.4639

of the Ca^{2+} puff statistics. The white symbol in each violin plot displays median values. The white line on the violin plots depicts the mean of each data set. Violin plots of the wild-type 1 IPR IPIs from both simulated and experimental data show a concentrated distribution around the mean and median values. The experimental data has longer IPIs compared to the simulated data. In comparison to the wild-type 1 IPR IPI data, the E2002D-type 1 IPR IPI data has a broader shape but maintains the uni-modal distribution. Our E2002D-type 1 IPR model simulated longer IPIs than those seen within the experimental data. The large difference between the frequency of Ca^{2+} puffs in the wild-type 1 IPR and E2002D-type 1 IPR data can be seen in the violin plots. This is shown by the data points displayed in the plot which highlight a higher density within the wild-type 1 IPR data.

Except for some higher Ca^{2+} puff amplitudes in the wild-type 1 IPR

experimental data, the shape of the violin plots for the simulated and experimental wild-type 1 IPR amplitude data are similar. These results are also consistent with the E2002D-type 1 IPR data. The violin plots for the wild-type 1 IPR duration data have a similar density and variability. As shown in Fig 4.6, our wild-type 1 IPR model produces Ca^{2+} puff durations that are longer than those seen in the experimental data. This result is also evident in the E2002D-type 1 IPR data set.

We have shown our Ca^{2+} puff model produces IPI, puff amplitude and puff duration that are in good agreement with the pooled experimental data. To analyse this further, we randomly select a 60 second sub-interval from our Ca^{2+} traces and compare our puff statistics to those from an experimental data set. We choose 60 seconds as this is the same time frame used in the experiments by Arige et al. (2022) and sample 10 times from our simulated data to compare with each of the experimental wild-type 1 IPR data sets. The frequency of Ca^{2+} events produced by an E2002D-type 1 IPR is so small these results are not suitable to be compared using histograms, therefore we compare the data using a point-by-point comparison of our model statistics with the experimental data. We repeated the sampling from our E2002D-type 1 IPR model 5 times, in line with the number of experimental groups used to produce the pooled E2002D-type 1 IPR statistical distributions described in Chapter 2. An example of our results, presented in Fig 4.8, shows for a time period equivalent to that used in the experimental studies, our wild-type 1 IPR model produces a similar IPI distribution, has an amplitude distribution of a similar variation and duration distribution with a similar mode. However, the duration distribution from the wild-type 1 IPR model

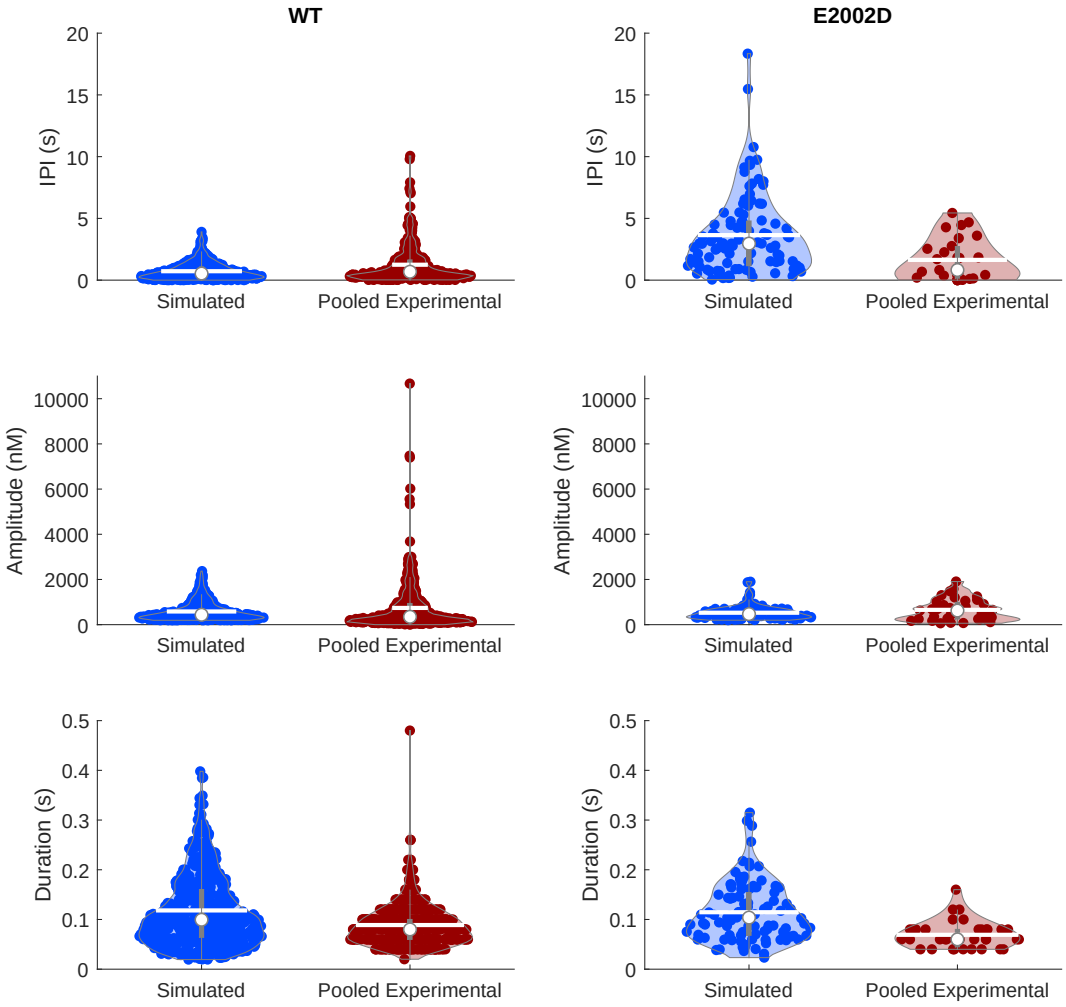

Figure 4.7: Violin plots comparing the Ca^{2+} puff statistics for the wild-type 1 IPR and E2002D-type 1 IPR models and experimental data results.

has a larger variation. Comparison of our 60s subsets with each wild-type 1 IPR experimental data group is presented in Fig A.4-A.5. Results from our E2002D-type 1 IPR model are comparable with the experimental results. Comparisons of each E2002D-type 1 data set is shown in Fig A.6.

Our results show we can successfully simulate similar IPI distributions, Ca^{2+} puff amplitudes and Ca^{2+} puff durations to the experimental data. From our results, we have shown that our model can accurately produce the same Ca^{2+} puff results as the wild-type 1 IPR data (Arige et al., 2022). This suggests that our model could be used to understand the IP_3R behaviour for longer periods that are not feasible within experimental studies.

4.4 Chapter discussion

Mathematical models can support understanding the effect of molecular changes on the IP_3R. Through parameterising models for both wild-type 1 IPR and E2002D-type 1 IPR, one can identify the differences between the models and relate this to the biological changes made to the IP_3R. The primary aim of this chapter was to parameterise two hybrid stochastic systems, based on the model presented in Chapter 3, that can simulate Ca^{2+} puffs representative of experimental data (Arige et al., 2022).

The stochastic behaviour of the IP_3R is influenced by the positive and negative feedback effects of Ca^{2+} (Berridge, 1997). Arige et al. (2022) state the negative charge on the side chain residue at the 2002 position in hIP_3R1 is critical for binding to Ca^{2+}. Whilst it is evident within the analysis of the experimental data (see Chapter 2) that the substitution at the 2002 glutamic acid residue with aspartate causes a decrease in P_o of the IP_3R and

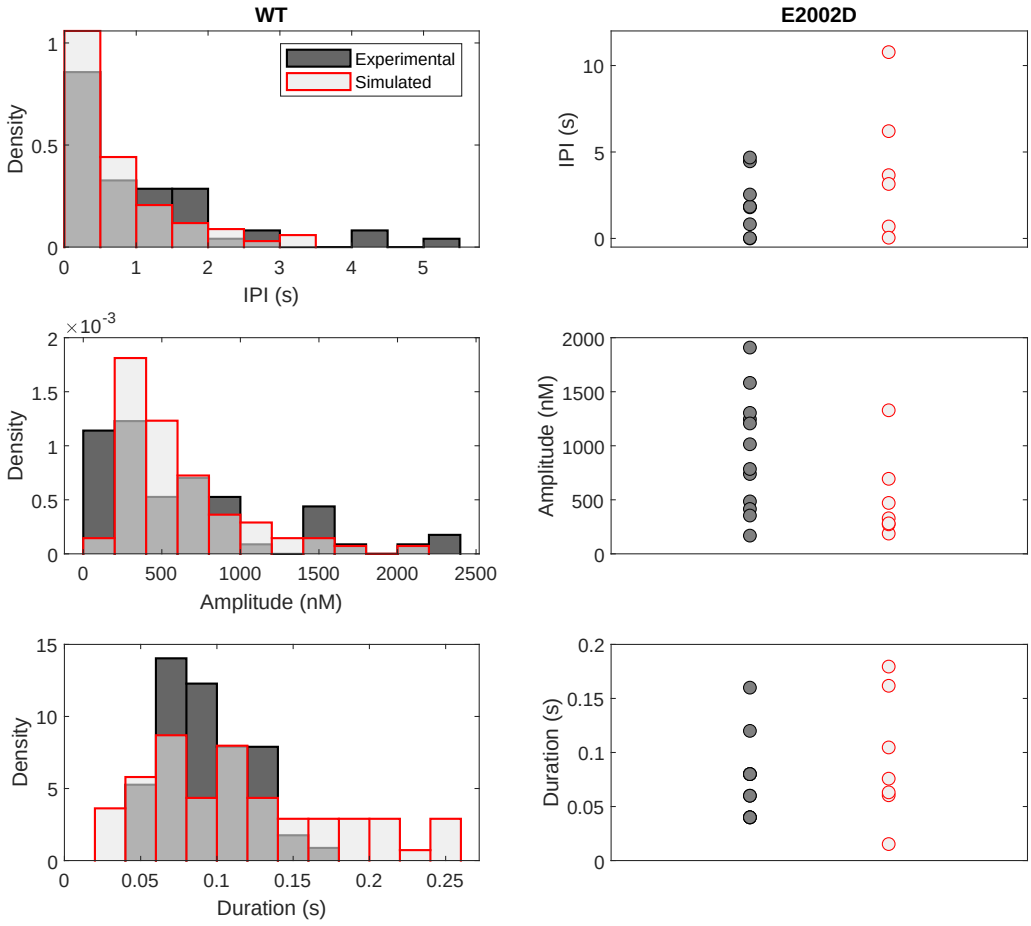

Figure 4.8: Comparison of Ca^{2+} puff statistics from a 60 second subset of our simulated Ca^{2+} trace with data from one experimental group.

thus, a decrease in Ca^{2+} puff activity, here we want to understand mathematically, why this is and how can we relate the changes that occur within our mathematical model to the biological processes.

Hierarchical mechanistic models which begin with building a single channel model and develop into an IP_3R cluster model allow us to understand how single IP_3R dynamics influence Ca^{2+} puffs (Islam, 2020). A single IP_3R with a high P_o is more likely to respond to Ca^{2+} and trigger a response from neighbouring IP_3R . However, if P_o is decreased the IP_3R becomes less likely to open. This can reduce the frequency of Ca^{2+} puff events and lead to longer IPIs and shorter Ca^{2+} puff amplitudes. The positive and negative feedback of an IP_3R to Ca^{2+} influences Ca^{2+} puff amplitude (Berridge, 1997). Therefore, a change to the feedback of a single IP_3R can impact the amplitude of Ca^{2+} puffs.

We compared the steady-state transition rates for the wild-type 1 IPR and E2002D-type 1 IPR models. Due to the IP_3R being in a consistent closed state when the Ca^{2+} concentration was 10nM and 100µM, we were unable to calculate the transition rates. As described in the Results section, the fit of our curve shows $q_{oc\infty}$ is high and $q_{co\infty}$ is low at these concentrations. These results are similar to the transition curves of Siekmann et al. (2012); Cao et al. (2014). Our results show that although $q_{co\infty}$ is lower for the E2002D-type 1 IPR, the transition rate for both models is largest when the Ca^{2+} concentration is between 200nM and 1µM. In comparison, for the wild-type 1 IPR model, $q_{oc\infty}$ decreases between 200nM and 1µM. This behaviour is akin to previous IP_3R models (Siekmann et al., 2012; Cao et al., 2013, 2014). Interestingly, for the E2002D-type 1 IPR, $q_{oc\infty}$ is similar for Ca^{2+}

concentrations between 50nM and 1µM. This difference in the $q_{oc\infty}$ transition rate for the wild-type 1 IPR and E2002D-type 1 IPR suggests the substitution at the 2002 glutamic acid residue causes a loss of Ca^{2+} sensitivity as the transition rate $q_{oc\infty}$ is not affected by changes in Ca^{2+} concentration. The fit of $q_{oc\infty}$ to the experimental data could be considered poor, more specifically for the E2002D-type 1 IPR. Our model is not able to fit the lower transition rate seen at 10nM. This may suggest that the equations for $q_{oc\infty}$ do not correctly represent the behaviour of the E2002D-type 1 IPR. However, we see a good fit to $q_{co\infty}$ and P_o. Due to this, one could argue that the transition from the closed to open state is the main driver behind IP_3R behaviour.

The difference between the transition rates for the wild-type 1 IPR and E2002D-type 1 IPR models was investigated further through a comparison of the gating variables. The m_{oc}, h_{oc}, m_{co} and h_{co} gating variables can be considered activation and inhibition variables controlling the transition rates q_{oc} and q_{co} (Cao et al., 2013). m_{co} and h_{co} control the activation and termination of Ca^{2+} puffs (Cao et al., 2013). In the wild-type 1 IPR model, m_{co} replicated a similar shape to the Ca^{2+} puff whereas in the E2002D-type 1 IPR model, m_{co} did not respond as greatly (see Fig 4.5). Similarly, gating variables associated with q_{oc}, m_{oc} and h_{oc}, were not sensitive to changes in Ca^{2+} concentration in the E2002D-type 1 IPR model. m_{oc} remained high and h_{oc} remained low, thus effecting q_{oc}. The subsequent effect of the E2002D-type 1 IPR not responding to Ca^{2+} concentrations that would otherwise stimulate a healthy IP_3R is that fewer IP_3R open, therefore leading to infrequent Ca^{2+} puff events and smaller Ca^{2+} puff amplitudes.

A difficulty within parameterising our models lies in firstly, the large

number of parameters required to model the gating variable dynamics and secondly, having access to patch clamp data from one IP_3 concentration. Maximal P_o vary upon cell type, with Swaminathan et al. (2009) reporting values between <0.01 and 0.5 for IP_3 concentrations of 2µM. Wagner and Yule (2012) state a P_o value of 0.27 for rh$IP_3$1 at an IP_3 concentration of 1µM. Our maximal P_o for the wild-type 1 IPR model at IP_3=1µM was 0.017, therefore conforms with prior results. The maximal P_o for the E2002D-type 1 IPR is greatly affected, reducing to 0.0016.

Both of our IP_3R cluster models were able to produce attributes of the Ca^{2+} puffs seen within the experimental data. Our wild-type 1 IPR model can capture the exponential decay evidenced in the experimental IPI distribution as well as having Ca^{2+} puffs that are of similar amplitude and duration. Whilst our model did not produce Ca^{2+} puffs of a high amplitude during our simulation, the number of IP_3R in a cluster within our model could enable this to happen. Longer simulations would be required to determine if this is the case. 60 second subsets of our simulated wild-type 1 IPR Ca^{2+} trace produced comparable Ca^{2+} puff statistics to different experimental groups.

A notable difference when comparing the experimental and simulated IPI distributions from the pooled E2002D-type 1 IPR data is that the experimental data is exponentially distributed whereas the simulated data is gamma distributed. The result from our model suggests the E2002D-type 1 IPR does have a refractory period. An advantage of our model is that we can simulate longer Ca^{2+} traces than capable under experimental conditions, therefore we can capture more data and a possible refractory period that is missed in experiments. Furthermore, the maximum IPI from the simulated data is over

three times greater than the experimental result. Again, the longer simulation time from our mathematical model will pick up the longer IPIs that would be missed in experimental studies that are 60 seconds long. Comparison of the spread and density of the IPI, Ca^{2+} puff amplitude and Ca^{2+} puff duration distributions indicated simulated results are similar to the experimental data. Due to the infrequency of Ca^{2+} events in the E2002D-type 1 IPR simulated and experimental data, comparison of Ca^{2+} puff statistics using histograms was not possible. Instead, we opted for comparing the data by point-by-point comparison, ensuring our model produced Ca^{2+} statistics within the same range as the experimental data. Our E2002D-type 1 IPR model produced Ca^{2+} puff amplitudes of a similar range to the experimental data, however IPIs were often longer.

Latency distributions can provide valuable insights into how a single IP_3R responds to changes in ligand concentration. Previous studies have shown that the successful modelling of Ca^{2+} puffs relies on stationary single channel and latency data (Ullah et al., 2012a; Cao et al., 2013, 2014). To parameterise their Markov models, researchers such as Ullah et al. (2012a) and Cao et al. (2013), use the experimental results by Mak et al. (2007). Our models have two states therefore they cannot generate the multi-modal distribution observed in the experimental results presented by Mak et al. (2007). However, the activation and deactivation latency's maximum peak of the wild-type 1 IPR appears to be similar to the results obtained in the experiments by Mak et al. (2007) and the simulations by Cao et al. (2013). The average deactivation latencies were longer for the E2002D-type 1 IPR. These results suggest the E2002D-type 1 IPR takes longer to recover from activating Ca^{2+}

concentrations.

In this chapter, we have demonstrated that a simple two-state Markov model can be used to simulate the behaviour of wild-type 1 IPR and E2002D-type 1 IPR and show that using this model we can produce Ca^{2+} puffs characteristic of the experimental data. We achieve this by, firstly, parameterising a two-state continuous time Markov model using patch clamp data (Arige et al., 2022). Stationary transition rates were calculated using the inverse of the mean open and closed time of the IP_3R. To account for the delay in the IP_3R opening (Mak et al., 2007) our model uses integral terms that can be interpreted as the IP_3R averaging over past Ca^{2+} concentrations (see Chapter 3 for details). The latency distributions for the two models were simulated and compared.

Using our parameterised single channel models, we built IP_3R cluster models and simulated Ca^{2+} traces for 400s. To determine the accuracy of our model at simulating Ca^{2+} puffs that have the same characteristics as the experimental data we compared the IPIs, Ca^{2+} puff amplitudes and Ca^{2+} puff duration's qualitatively and quantitatively. Our Ca^{2+} puffs followed the same characteristics as the experimental data, exhibiting a rapid rise in Ca^{2+} concentration followed by a slower decrease (Berridge, 1997). We compared Ca^{2+} puff statistics with pooled experimental data. With the aim of direct comparison between the simulated and experimental data, we took random 60 second subsets from our longer Ca^{2+} trace and compared the Ca^{2+} puff statistics with individual experimental groups.

A key aspect within IP_3R modelling is modal gating (Siekmann et al., 2016). Whilst we chose to focus on the Ca^{2+} dynamics within our research,

future investigations could include building upon our two-state models to create IP_3R models that can simulate modal gating behaviour seen within the experimental data (Arige et al., 2022).

5 Discussion

5.1 Discussion

Ca^{2+} plays a crucial role in supporting the regulation of cellular processes within the human body (Berridge et al., 2000). The control of Ca^{2+} ions by ion channels causes cellular physiological changes that allow humans to function (Islam, 2020). For example, the contraction of muscles, firing of neurons, release of insulin from the pancreas and secretion of fluid from salivary glands all rely on a healthy Ca^{2+} signalling system (Capener et al., 2002; Bezprozvanny, 2009; Rückl et al., 2015; Han et al., 2017). However, an abnormal Ca^{2+} signalling system has been linked with a vast array of human diseases, such as heart failure, neurological conditions, diabetes and cancers (Etcheberrigaray et al., 1998; Berridge, 2003; Pchitskaya et al., 2018; Tong et al., 2018; Islam, 2020; Grady and Morgan, 2021; Klocke et al., 2023). Experimentalists have investigated the effect of mutation on the IP_3R activity. Mutations can affect IP_3R binding, decrease channel activity and cause a lack of Ca^{2+} release (Terry et al., 2020; Arige et al., 2022). This change in the IP_3R activity can be detrimental to individual health, having been linked to diseases such as ataxia, Gillespie syndrome, and generalized anhidrosis (Terry et al., 2020).

Mathematical models of the Ca^{2+} signalling are often complex, requiring a high number of parameters to be able to account for both IP_3R and Ca^{2+} dynamics. However, when parameterised using experimental data, they can provide insights into the Ca^{2+} signalling system that may be difficult to uncover under experimental conditions.

In this thesis, we presented a hybrid stochastic system based on integrodifferential equations. Using our model we were able to accurately simulate the IP_3R and Ca^{2+} dynamics seen within experimental data and previous Ca^{2+} puff models (Cao et al., 2013, 2014). By incorporating integrodifferential equations into our IP_3R model, we had the advantage of being able to investigate the idea of IP_3R *memory*. We then parameterised our model using stationary single channel and Ca^{2+} puff data from Arige et al. (2022), creating two Ca^{2+} puff models.

In Chapter 2 we analysed data from three IP_3R and compared the Ca^{2+} puff statistics from the different data sets. Our results demonstrated that exo 76 wild-type 1 IPR produces longer IPIs compared to wild-type 1 IPR and E2002D-type 1 IPR. Furthermore, we found that the substitution at the 2002 glutamic acid residue with aspartic acid led to infrequent Ca^{2+} puffs of a shorter amplitude. We then parameterised the exponential, gamma and time-dependent (Thurley and Falcke, 2011) distributions using the IPI data from each experimental data set. Results showed the wild-type 1 IPR and E2002D-type 1 IPR recover quickly from Ca^{2+} inhibition in comparison to exo 76 wild-type 1 IPR. We compared the statistical distributions by calculating information criteria. We determined that statistically the gamma distribution provided the best representation of all IPI data sets because it

can capture the presence of latent and non-latent behaviour of the IP_3R . This is the first time, to our knowledge, that information criteria have been used to compare statistical distributions for IPI distributions.

In Chapter 3 we built a hybrid stochastic system based on integrodifferential equations. Beginning with the Cao et al. (2013) model, which uses gating variables to simulate the delay in the IP_3R responding to change in Ca^{2+} concentration, we turned the ODEs representing the gating variables into integral terms using the method by Brady (1972). This gave us the advantage of being able to directly compare our model results to those by Siekmann et al. (2012); Cao et al. (2013) and investigate IP_3R *memory*. We simplified our six-state model, creating a reduced six-state and two-state Markov model that produces comparable results to more complex models.

Our model results show the IP_3R requires "knowledge" of past Ca^{2+} concentrations to produce Ca^{2+} puffs, however infinite integrals, that would represent an "infinite memory" are computationally unfeasible and in our opinion, not biologically realistic. By introducing the integrals as finite terms, our model has the advantage of analysing how changes to the delay term, τ, impact IP_3R and Ca^{2+} dynamics. We find that the IP_3R does not require an infinite *memory*, however, one that is sufficiently long. Our model uses a delay length of 3s. Experimental results by Mak et al. (2007) have shown the IP_3R does not respond immediately to step changes in ligand concentrations. Our model, through incorporating the integral terms, was able to account for this latent behaviour. Results showed that Ca^{2+} puffs were not produced when the length of the delay term, τ, was short and only took into account the current Ca^{2+} concentration. This, along with results by

Mak et al. (2007), contrast the view of Villalba-Galea and Chiem (2020) who stated ligand-gated ion channels are unaffected by previous exposures of the receptor to the ligand.

We replicated the experimental conditions by Mak et al. (2007) for each model. Activation latencies simulated by the six-state model from a step change in Ca^{2+} concentration 10nM to 2µM were longer than those produced by Mak et al. (2007). However, activation latencies simulated by the reduced six-state and two-state models are comparable with those produced by Mak et al. (2007). This indicates IP_3R activation only requires "knowledge" of the recent or small portion of the past calcium concentration.

In the final chapter of this thesis, Chapter 4, we used stationary single channel data from wild-type 1 IPR and E2002D-type 1 IPR (Arige et al., 2022) to parameterise a two-state Markov model and built an IP_3R cluster model to simulate Ca^{2+} puffs. We compared our simulated results with the experimental results and considered how the models differ to understand the biological differences between the two IP_3R. Results showed our hybrid stochastic systems could simulate the same Ca^{2+} puff dynamics seen within experimental conditions. Arige et al. (2022) state the negative charge on the side chain residue at the 2002 position in hIP_3R1 is critical for Ca^{2+} binding. This is shown by the substitution at the 2002 glutamic acid residue with aspartic acid leading to inactivity in the hIP_3R1. Using our model, we showed that this mutation causes the gating variables to be less responsive to change in Ca^{2+} concentrations. This leads to longer IPIs and shorter Ca^{2+} puff amplitudes. To accurately compare the experimental and simulated data, we took a random 60 second subset of our model results and compared this with

data from an experimental group. Results were comparable, indicating our mathematical model can be used to provide details that would be provided from longer experimental conditions.

5.2 Future work

The analysis of stochastic models is often a considerable computational challenge. Understanding stochastic dynamics generally requires time-consuming simulations which then need to be analysed statistically. However, for hybrid stochastic systems, time-dependent probability densities for the states of the Markov model depending on the continuous variables of the ODE system coupled to the Markov model can be calculated from a system of deterministic partial differential equations (PDEs). Future research could explore how the open and closed time distributions depend on Ca^{2+} and the fluorescent buffer. Similar to the open and closed time distributions for models of single ion channels, the open and closed time densities are very useful for gaining general insights into the model behaviour. An interesting question to consider would be how the probability density functions differ depending on how healthy the ion channel is, as demonstrated by Tveito and Lines (2016). This approach has already been applied in both cellular biology and predator-prey models (Tveito and Lines, 2016; Bressloff and Maclaurin, 2018; Hawker and Siekmann, 2023). Furthermore, we suggest there could be development of the models produced within this thesis. Firstly, an attempt could be made to simplify the integrodifferential equation proposed within our model. If successful, this would result in a kernel integrated into our ODE model. The kernel could thus be parameterised easily with single-channel data, such as

that by Mak et al. (2007). A second development could include incorporating modal gating into the IP_3R model. Whilst complex, these detailed models would provide even more distinguishable differences between the wild-type 1 IPR and E2002D-type 1 IPR. For example, we could answer questions such as how many modes do the IP_3R have and do the number of states within the models differ? This would provide interesting insight into the IP_3R structure.

Appendices

A

Appendix

A.1 IPI distributions parameterised using statistical distributions

In Fig A.1, we present the IPI distributions from the pooled experimental data with the parameterised Exponential, Gamma and Time-Dependent distributions. Whilst the exo 76 wild-type 1 IPR and wild-type 1 IPR pooled data appear to have a refractory period, shown by the gradual increase in IPIs, the E2002D-type 1 IPR display an Exponential distribution. Parameter estimations for each statistical distribution are presented in Chapter 2. The Gamma and Time-Dependent distribution qualitatively fit the pooled exo 76 wild-type 1 IPR IPI distribution best as they describe the shorter IPIs. Whilst the wild-type 1 IPR IPI distribution hints at a possible refractory period, all three statistical distributions do not describe this behaviour. The E2002D-type 1 IPR IPI distribution appears to be exponentially distributed, with a higher frequency of short IPIs. All statistical distributions model this exponential decay, however, it is difficult to determine if this is the true nature of the E2002D-type 1 IPR due to the small number of data points available.

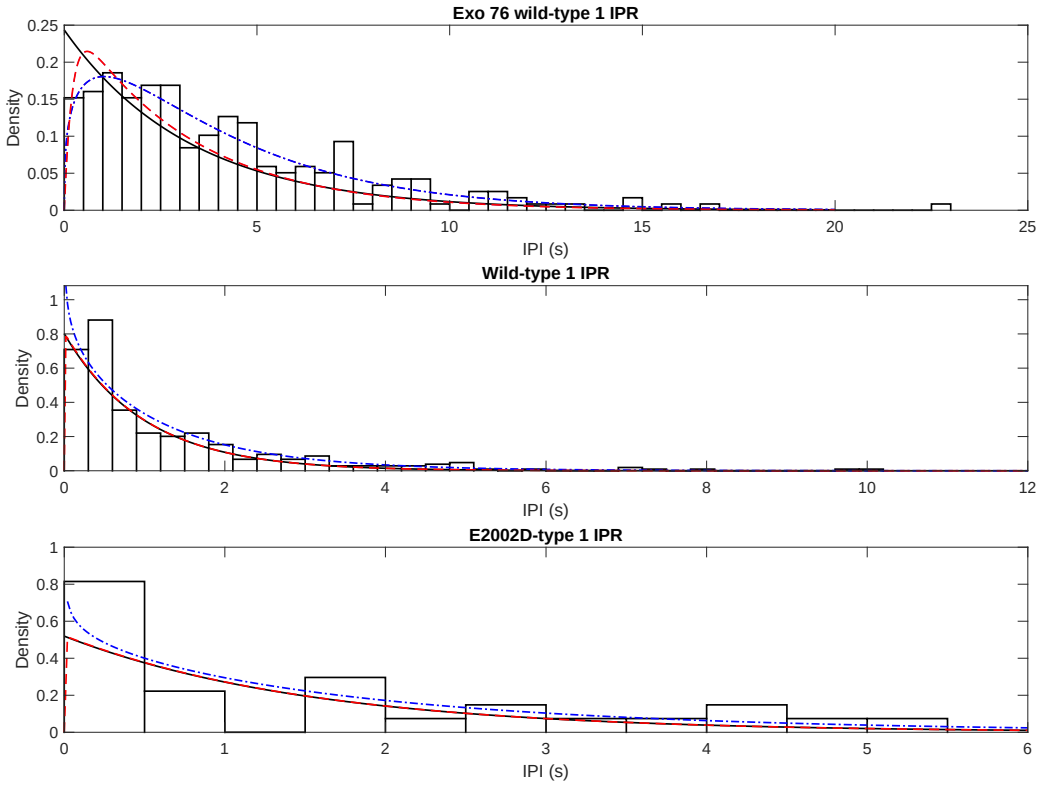

Figure A.1: Comparison of pooled IPI distributions for the exo 76 wild-type 1 IPR, wild-type 1 IPR and E2002D-type 1 IPR. All IPI distributions are fit with the Exponential (black line), Gamma (blue dot-dashed line) and Time-Dependent (red dashed line) distributions.

A.2 Kolmogorov Smirnov test for the pooled exo 76 wild-type 1 IPR and wild-type 1 IPR IPI distributions

Fig A.2 shows the empirical and model CDF for the exo 76 pooled wild-type 1 IPR IPI distributions. The Exponential CDF does not fit well with the empirical CDF. We reject H_o at the 5% significance level for the Exponential distribution. P-values and test statistics can be found in Table 2.5.

In Fig A.3 we present the empirical and model CDF for the pooled wild-type 1 IPR IPI distributions. Our test statistics, presented in Table 2.3.2, demonstrate the Exponential distribution has the largest difference from the empirical CDF. This can be seen within Fig A.3; the Gamma and Time-Dependent distributions have a much closer fit to the pooled experimental data.

A.3 Comparison of simulated and experimental Ca^{2+}puff statistics for wild-type 1 IPR and E2002D-type 1 IPR

In Fig A.4-A.5 we compare the Ca^{2+} puff statistics taken from 60s subsets of our simulated wild-type 1 IPR model, presented in Chapter 4, with each group of experimental wild-type 1 IPR data. Our results demonstrate that when considering 60s subsets of our wild-type 1 IPR model, we can produce similar IPI distributions to the experimental data. Ca^{2+} puff amplitude

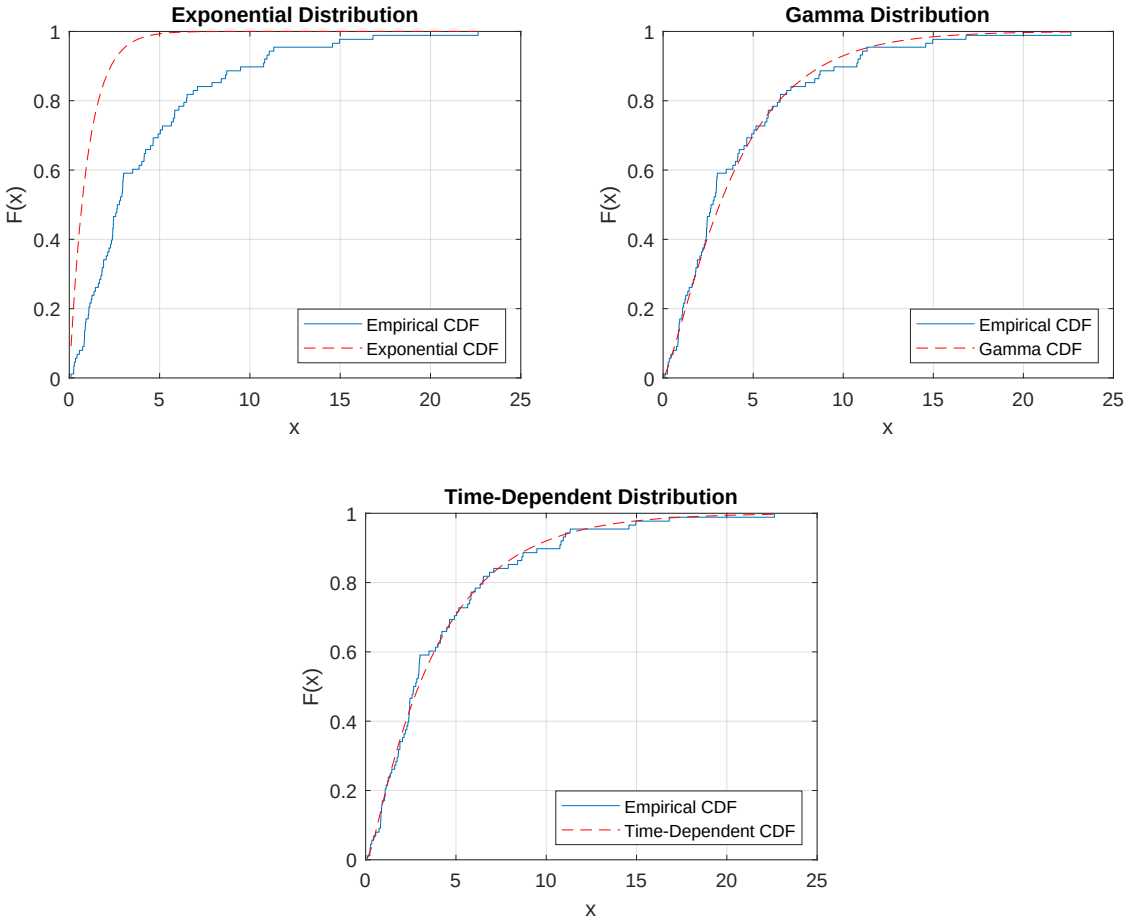

Figure A.2: Comparison of the Exponential, Gamma and Time-Dependent cumulative density function with the empirical cumulative distribution function from the pooled exo 76 wild-type 1 IPR IPI data.

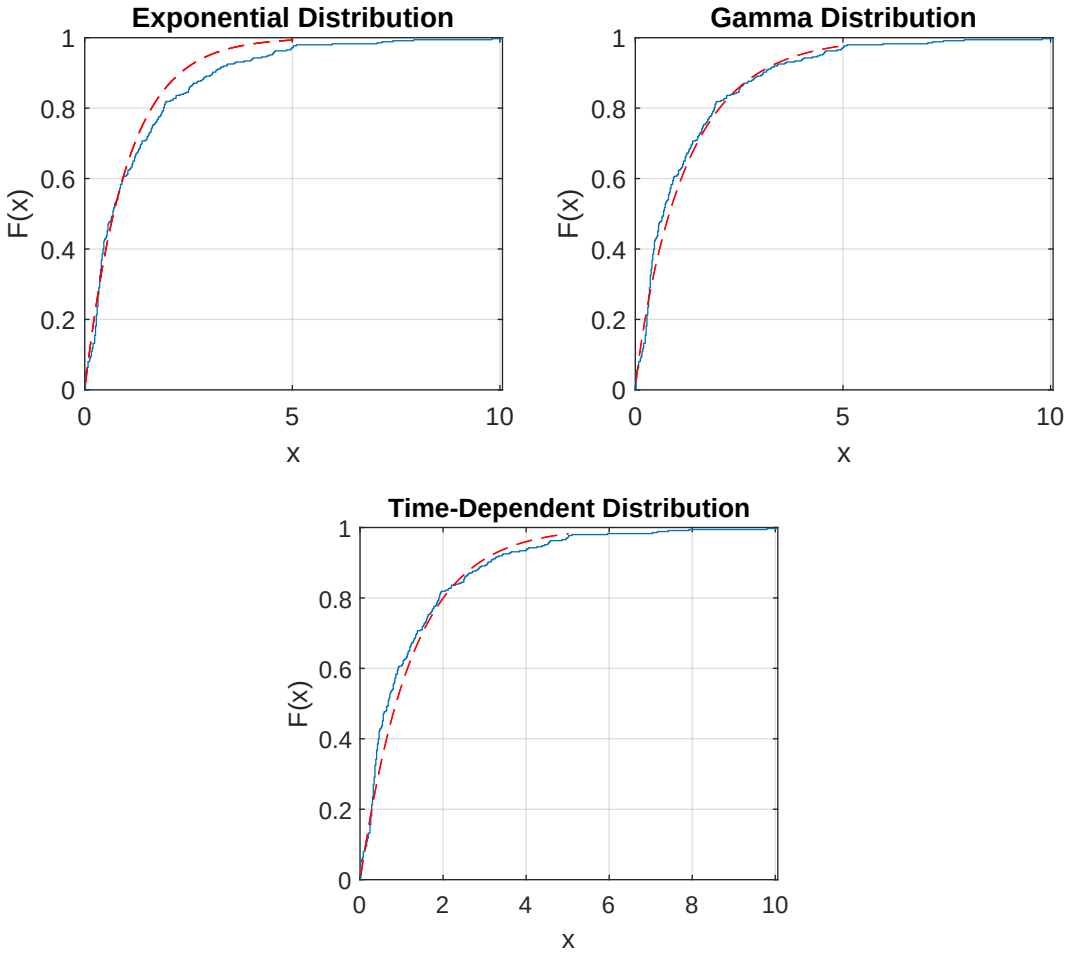

Figure A.3: Comparison of the Exponential, Gamma and Time-Dependent cumulative density function with the empirical cumulative distribution function from the pooled wild-type 1 IPR IPI data.

distributions were similar for 6 of our data sets, however, the experimental data often have a longer tail. Whilst our Ca^{2+} puff duration distributions have a similar mode to the experimental data, they were more variable.

In Fig A.6 we compare the Ca^{2+} puff statistics taken from random 60s subsets of our simulated E2002D-type 1 IPR model, presented in Chapter 4, with each group of experimental E2002D-type 1 IPR data. Due to the sample size of the experimental data sets, we cannot compare our results using histograms and instead opt for a point-by-point comparison. Our results demonstrate our model simulates longer IPIs and Ca^{2+} puff durations compared to the experimental data. The range of Ca^{2+} puff amplitudes is similar across the simulated and experimental groups. One experimental group has very short Ca^{2+} puff amplitudes - this is not replicated in the random subsets selected from our model.

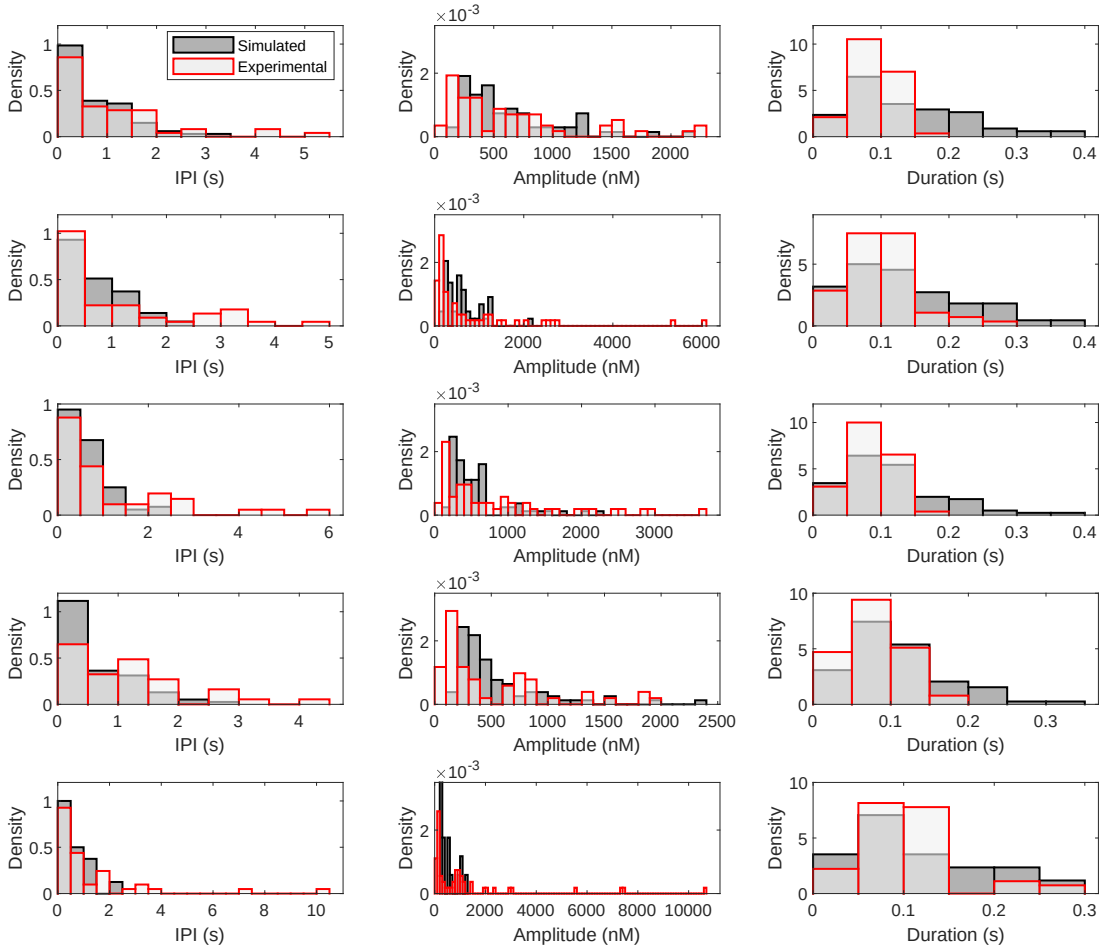

Figure A.4: Comparison of Ca^{2+}puff statistics taken from $60s$ subsets of our simulated wild-type 1 IPR model with experimental data sets 1-5 from Chapter 2.

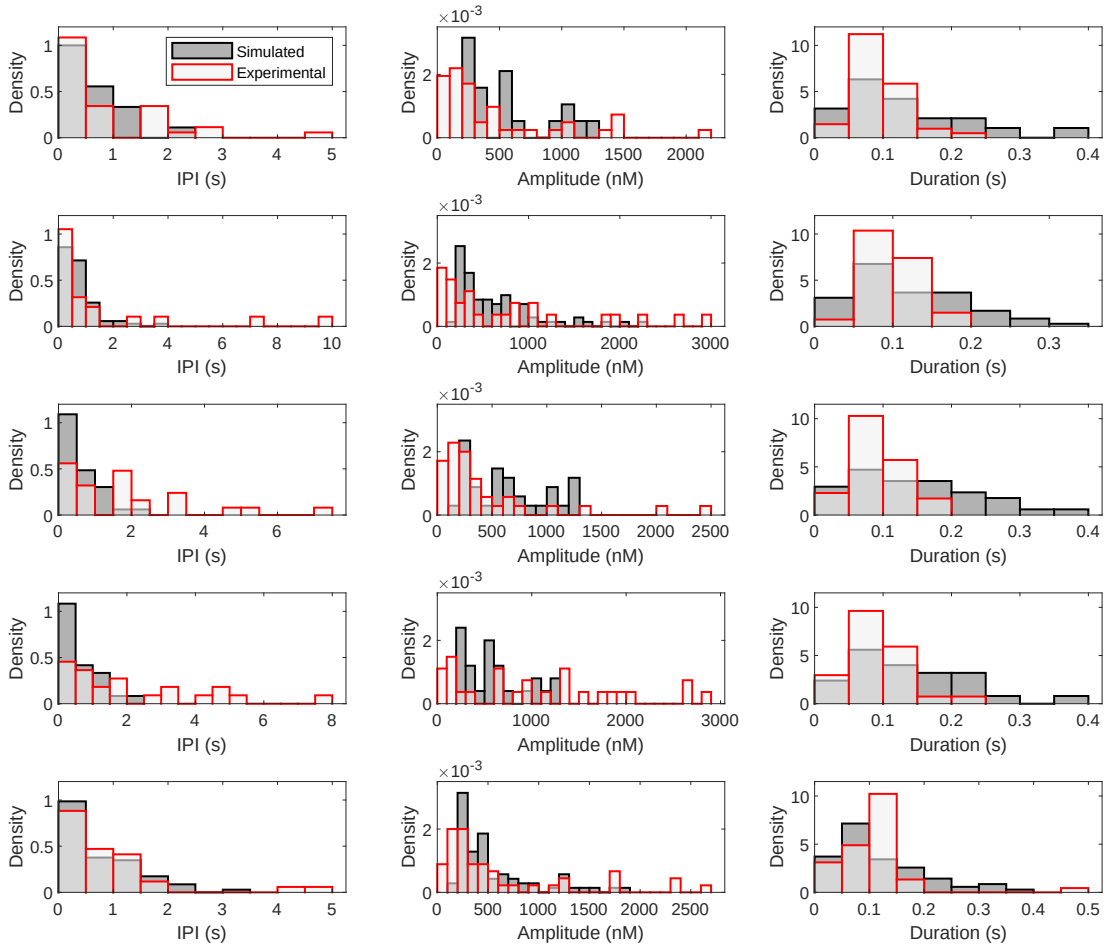

Figure A.5: Comparison of Ca^{2+}puff statistics taken from $60s$ subsets of our simulated wild-type 1 IPR model with experimental data sets 6-10 from Chapter 2.

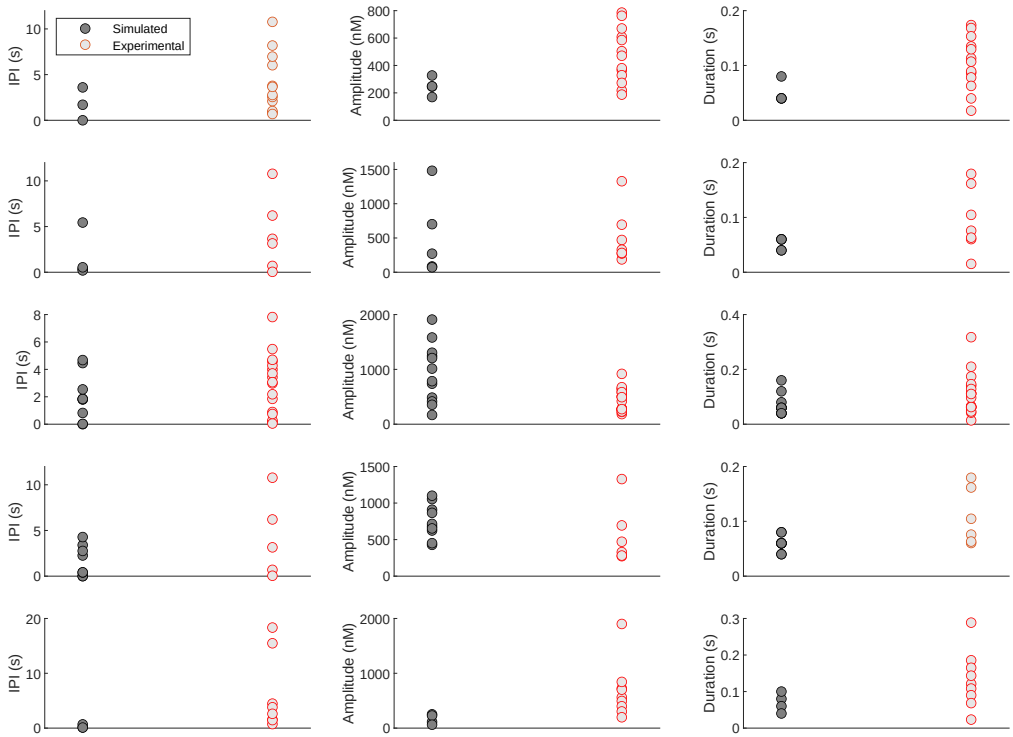

Figure A.6: Comparison of Ca^{2+}puff statistics taken from $60s$ subsets of our simulated E2002D-type 1 IPR model with experimental data sets from Chapter 2.

References

Aurelien Alfonsi, Eric Cances, Gabriel Turinici, Barbara Di Ventura, and Wilhelm Huisinga. Adaptive simulation of hybrid stochastic and deterministic models for biochemcial systems. *ESAIM: PROCEEDINGS*, 14: 1–13, 2005. doi: 10.1051/proc;2005001.

Indu Ambudkar. Calcium signaling defects underlying salivary gland dysfunction. *Biochimica et Biophysica Acta - Molecular Cell Research*, 1865: 1771–1777, 11 2018. ISSN 18792596. doi: 10.1016/j.bbamcr.2018.07.002.

Jeffrey Annis, Brent J. Miller, and Thomas J. Palmeri. Bayesian inference with stan: A tutorial on adding custom distributions. *Behavior Research Methods*, 49:863–886, 6 2017. ISSN 15543528. doi: 10.3758/s13428-016-0746-9.

Vikas Arige, Lara E. Terry, Larry E. Wagner, Mariah R. Baker, Guizhen Fan, Irina I. Serysheva, and David I. Yule. Functional determination of calcium binding sites required for the activation of inositol 1,4,5-trisphosphate receptors. *BioRviv*, 2022.

Mariah R. Baker, Guizhen Fan, Vikas Arige, David I. Yule, and Irina I. Serysheva. Understanding ip3r channels: From structural underpinnings to ligand-dependent conformational landscape. *Cell Calcium*, 114, 9 2023. ISSN 15321991. doi: 10.1016/j.ceca.2023.102770.

H. C. Berg and E. M. Purcell. Physics of chemoreception. *Biophysical Journal*, 20:193–219, 1977. ISSN 00063495. doi: 10.1016/S0006-3495(77)85544-6.

M J Berridge. Calcium oscillations. *Journal of Biological Chemistry*, 265(17):9583–9586, 1990. ISSN 0021-9258. doi: https://doi.org/10.1016/S0021-9258(19)38704-6. URL `https://www.sciencedirect.com/science/article/pii/S0021925819387046`.

References

M. J. Berridge. Cardiac calcium signalling. *Biochemical Society Transactions*, 31:930–933, 2003. ISSN 03005127. doi: 10.1042/bst0310930.

Michael J Berridge. Elementary and global aspects of calcium signalling. *The Journal of physiology*, 499:291–306, 1997. doi: https://doi.org/10.1113/jphysiol.1997.sp02192.

M.J. Berridge, P. Lipp, and M.D. Bootman. The versatility and universality of calcium signalling. *Nature Reviews Molecular Cell Biology*, 1:11–21, 2000. doi: 10.1038/35036035.

Ilya Bezprozvanny. Calcium signaling and neurodegenerative diseases. *Trends in Molecular Medicine*, 15:89–100, 3 2009. ISSN 14714914. doi: 10.1016/j.molmed.2009.01.001.

Ilya Bezprozvanny and Mark P. Mattson. Neuronal calcium mishandling and the pathogenesis of alzheimer's disease. *Trends in Neurosciences*, 31:454–463, 9 2008. ISSN 01662236. doi: 10.1016/j.tins.2008.06.005.

Brendan A. Bicknell and Geoffrey J. Goodhill. Emergence of ion channel modal gating from independent subunit kinetics. *Proceedings of the National Academy of Sciences of the United States of America*, 113:E5288–E5297, 9 2016. ISSN 10916490. doi: 10.1073/pnas.1604090113.

Martin D. Bootman. Calcium signaling. *Cold Spring Harbor Perspectives in Biology*, 4:1–3, 7 2012. ISSN 19430264. doi: 10.1101/cshperspect.a011171.

Martin D Bootman, Michael J Berridge, and Peter Lipp. Cooking with calcium: The recipes for composing global signals from elementary events. *Cell*, 91:367–373, 10 1997. ISSN 00928674. doi: 10.1016/S0092-8674(00)80420-1.

Stephen W. Brady. Boundedness theorems and other mathematical studies of a hodgkin- huxley type system of differential equations : Numerical treatment of thresholds and stationary values. *Mathematical Biosciences*, 6, 1970. doi: 10.1016/0025-5564(70)90067-2.

Stephen W. Brady. The integro-differential equation form of a hodgkin-huxley type system of differential equations. *Mathematical Biosciences*, 13:229–234, 1972.

Paul C Bressloff and James N Maclaurin. Stochastic hybrid systems in cellular neuroscience. *Journal of Mathematical Neuroscience*, 8, 2018. doi: 10.1186/s13408-018-0067-7. URL `http://dx.doi.org/10.1186/s13408-018-0067-7`.

Clark A. Briggs, Shreaya Chakroborty, and Grace E. Stutzmann. Emerging pathways driving early synaptic pathology in alzheimer's disease. *Biochemical and Biophysical Research Communications*, 483:988–997, 2 2017. ISSN 10902104. doi: 10.1016/j.bbrc.2016.09.088.

Marisa Brini, Tito Calì, Denis Ottolini, and Ernesto Carafoli. Neuronal calcium signaling: Function and dysfunction. *Cellular and Molecular Life Sciences*, 71:2787–2814, 2014. ISSN 14209071. doi: 10.1007/s00018-013-1550-7.

Jonny Brooks-Bartlett. Probability concepts explained: Maximum likelihood estimation, 2018. URL `https://towardsdatascience.com/probability-concepts-explained-maximum-likelihood-estimation-c7b4342fdbb1`.

Jason I.E. Bruce and Andrew D. James. Targeting the calcium signalling machinery in cancer. *Cancers*, 12:1–34, 9 2020. ISSN 20726694. doi: 10.3390/cancers12092351.

Kenneth P. Burnham and David R. Anderson. Multimodel inference: Understanding aic and bic in model selection. *Sociological Methods and Research*, 33:261–304, 11 2004. ISSN 00491241. doi: 10.1177/0049124104268644.

Maria Calvo-Rodriguez and Brian J. Bacskai. Mitochondria and calcium in alzheimer's disease: From cell signaling to neuronal cell death. *Trends in Neurosciences*, 44:136–151, 2 2021. ISSN 1878108X. doi: 10.1016/j.tins.2020.10.004.

Pengxing Cao, Graham Donovan, Martin Falcke, and James Sneyd. A stochastic model of calcium puffs based on single-channel data. *Biophysical Journal*, 105:1133–1142, 2013. ISSN 0006-3495. doi: 10.1016/j.bpj.2013.07.034. URL `http://dx.doi.org/10.1016/j.bpj.2013.07.034`.

Pengxing Cao, Xiahui Tan, Graham Donovan, Michael J Sanderson, and James Sneyd. A deterministic model predicts the properties of stochastic calcium oscillations in airway smooth muscle cells. *PLoS Computational Biology*, 10, 2014. doi: 10.1371/journal.pcbi.1003783.

Pengxing Cao, Martin Falcke, and James Sneyd. Mapping interpuff interval distribution to the properties of inositol trisphosphate receptors. *Biophysical Journal*, 112:2138–2146, 2017. ISSN 0006-3495. doi: 10.1016/j.bpj.2017.03.019. URL `http://dx.doi.org/10.1016/j.bpj.2017.03.019`.

Charlotte E. Capener, Hyun Ji Kim, Yalini Arinaminpathy, and Mark S.P. Sansom. Ion channels: Structural bioinformatics and modelling. *Human*

References

Molecular Genetics, 11:2425–2433, 2002. ISSN 09646906. doi: 10.1093/hmg/11.20.2425.

Thomas D Carter and David Ogden. Kinetics of intracellular calcium release by inositol 1 , 4 , 5-trisphosphate and extracellular atp in porcine cultured aortic endothelial cells published by : Royal society stable url : https://www.jstor.org/stable/49546 references linked references are. *Proceedings: Biological Sciences*, 250:235–241, 1992.

Caroline Van Cauwenberghe, Christine Van Broeckhoven, and Kristel Sleegers. The genetic landscape of alzheimer disease: clinical implications and perspectives. *Genetics in medicine*, 2016.

D. Colquhoun and A. G. Hawkes. Relaxation and fluctuations of membrane currents that flow through drug-operated channels. *Proceedings of the Royal Society of London - Biological Sciences*, 199:231–262, 1977. ISSN 09628452. doi: 10.1098/rspb.1977.0137.

David Colquhoun and Alan Geoffrey Hawkes. On the stochastic properties of single ion channels. *Proceedings of the Royal Society of London*, pages 205–235, 1981. doi: 10.1098/rspb.1981.0003.

Jim M. Cushing. *Integrodifferential Equations and Delay Models in Population Dynamics*. Springer Berlin Heidelberg, 1st edition, 1977. ISBN 978-3-540-08449-5. doi: 10.1007/978-3-642-93073-7.

Motuma Yigezu Daba, Zhijie Fan, Qinyu Li, Xianglin Yuan, and Bo Liu. The role of calcium channels in prostate cancer progression and potential as a druggable target for prostate cancer treatment. *Critical Reviews in Oncology/Hematology*, 186:104014, 2023. ISSN 1040-8428. doi: https://doi.org/10.1016/j.critrevonc.2023.104014. URL `https://www.sciencedirect.com/science/article/pii/S1040842823001026`.

C E Dangerfield, D Kay, and K Burrage. Stochastic models and simulation of ion channel dynamics. *Procedia Computer Science*, 1:1587–1596, 2012. ISSN 1877-0509. doi: 10.1016/j.procs.2010.04.178. URL `http://dx.doi.org/10.1016/j.procs.2010.04.178`.

George D Dickinson, Divya Swaminathan, and Ian Parker. The probability of triggering calcium puffs is linearly related to the number of inositol trisphosphate receptors in a cluster. *Biophysical Journal*, 102:1826–1836, 2012. ISSN 0006-3495. doi: 10.1016/j.bpj.2012.03.029. URL `http://dx.doi.org/10.1016/j.bpj.2012.03.029`.

Jian Ding and Michiki Kasai. Analysis of multiple conductance states observed in ca2+ release channel of sarcoplasmic reticulum. *CELL STRUCTURE AND FUNCTION*, 21:7–15, 1996.

Ulrich Dobramysl, Sten Rüdiger, and Radek Erban. Particle-based multiscale modeling of calcium puff dynamics. *Society for Industrial and Applied Mathematics*, 14:997–1016, 2016.

W. W. Douglas and R. P. Rubin. The role of calcium in the secretory response of the adrenal medulla to acetylcholine. *The Journal of Physiology*, 159: 40–57, 11 1961. ISSN 0022-3751. doi: 10.1113/jphysiol.1961.sp006791.

Geneviève Dupont and James Sneyd. Recent developments in models of calcium signalling. *Systems Biology*, 3:15–22, 2017. ISSN 2452-3100. doi: 10.1016/j.coisb.2017.03.002. URL `http://dx.doi.org/10.1016/j.coisb.2017.03.002`.

Geneviève Dupont, Martin Falcke, Vivien Kirk, and James Sneyd. *Models of Calcium Signalling*. Springer Cham, 2016. ISBN 9783319296456. doi: https://doi.org/10.1007/978-3-319-29647-0.

Kyle L Ellefsen, Brett Settle, Ian Parker, and Ian F Smith. Cell calcium an algorithm for automated detection , localization and measurement of local calcium signals from camera-based imaging. *Cell Calcium*, 56:147–156, 2014. ISSN 0143-4160. doi: 10.1016/j.ceca.2014.06.003. URL `http://dx.doi.org/10.1016/j.ceca.2014.06.003`.

Kyle L Ellefsen, Jeffrey T Lock, Brett Settle, Carley A Karsten, and Ian Parker. Applications of flika, a python-based image processing and analysis platform, for studying local events of cellular calcium signaling. *Biochimica et Biophysica Acta (BBA) - Molecular Cell Research*, 1866:1171–1179, 2019. doi: 10.1016/j.bbamcr.2018.11.012.

Scott M. Emrich, Ryan E. Yoast, Ping Xin, Vikas Arige, Larry E. Wagner, Nadine Hempel, Donald L. Gill, James Sneyd, David I. Yule, and Mohamed Trebak. Omnitemporal choreographies of all five stim/orai and ip3rs underlie the complexity of mammalian ca2+ signaling. *Cell Reports*, 34, 3 2021. ISSN 22111247. doi: 10.1016/j.celrep.2021.108760.

René Etcheberrigaray, Naohide Hirashima, Linda Nee, José Prince, Stefano Govoni, Marco Racchi, Rudolph E Tanzi, and Daniel L Alkon. Calcium responses in fibroblasts from asymptomatic members of alzheimer's disease families. *Neurobiology of Disease*, 5:37–45, 1998. ISSN 09699961. doi: 10.1006/nbdi.1998.0176.

References

Guizhen Fan, Matthew L. Baker, Zhao Wang, Mariah R. Baker, Pavel A. Sinyagovskiy, Wah Chiu, Steven J. Ludtke, and Irina I. Serysheva. Gating machinery of insp3r channels revealed by electron cryomicroscopy. *Nature*, 527:336–341, 11 2015. ISSN 14764687. doi: 10.1038/nature15249.

Guizhen Fan, Mariah R Baker, Lara E Terry, Vikas Arige, Muyuan Chen, B Alexander, Matthew L Baker, Steven J Ludtke, David I Yule, and Irina I Serysheva. Structural dynamics underlying gating and regulation in ip3r channel. *Nature Communications*, 2022a. doi: 10.1038/s41467-022-34574-1.

Guizhen Fan, Mariah R. Baker, Lara E. Terry, Vikas Arige, Muyuan Chen, Alexander B. Seryshev, Matthew L. Baker, Steven J. Ludtke, David I. Yule, and Irina I. Serysheva. Conformational motions and ligand-binding underlying gating and regulation in ip3r channel. *Nature Communications*, 13, 12 2022b. ISSN 20411723. doi: 10.1038/s41467-022-34574-1.

Claire J. Fearnley, H. Llewelyn Roderick, and Martin D. Bootman. Calcium signaling in cardiac myocytes. *Cold Spring Harbor Perspectives in Biology*, 3:1–20, 2011. ISSN 19430264. doi: 10.1101/cshperspect.a004242.

Mingye Feng, Desma M. Grice, Helen M. Faddy, Nguyen Nguyen, Sharon Leitch, Yingyu Wang, Sabina Muend, Paraic A. Kenny, Saraswati Sukumar, Sarah J. Roberts-Thomson, Gregory R. Monteith, and Rajini Rao. Store-independent activation of orai1 by spca2 in mammary tumors. *Cell*, 143:84–98, 2010. ISSN 00928674. doi: 10.1016/j.cell.2010.08.040.

J. Kevin Foskett, Carl White, King Ho Cheung, and Don On Daniel Mak. Inositol trisphosphate receptor ca2+ release channels. *Physiological Reviews*, 87:593–658, 4 2007. ISSN 00319333. doi: 10.1152/physrev.00035.2006.

Daniel Fraiman, Bernardo Pando, Sheila Dargan, Ian Parker, and Silvina Ponce Dawson. Analysis of puff dynamics in oocytes : Interdependence of puff amplitude and interpuff interval. *Biophysical Journal*, 90: 3897–3907, 2006. ISSN 0006-3495. doi: 10.1529/biophysj.105.075911. URL `http://dx.doi.org/10.1529/biophysj.105.075911`.

M. Iveth Garcia and Darren Boehning. Cardiac inositol 1,4,5-trisphosphate receptors. *Biochimica et Biophysica Acta - Molecular Cell Research*, 1864: 907–914, 6 2017. ISSN 18792596. doi: 10.1016/j.bbamcr.2016.11.017.

Andrew Gelman, Jessica Hwang, and Aki Vehtari. Understanding predictive information criteria for bayesian models. *Statistics and Computing*, 24, 2013. doi: https://doi.org/10.1007/s11222-013-9416-2.

Andrew Gelman, John B. Carlin, Hal S. Stern, David B. Dunson, Aki Vehtari, and Donald B. Rubin. *Bayesian Data Analysis*. Taylor 'I&' Francis Group, LLC, 3rd edition, 2014. ISBN 978-1-4398-4095-5.

Elan Gin, Martin Falcke, Larry E. Wagner, David I. Yule, and James Sneyd. A kinetic model of the inositol trisphosphate receptor based on single-channel data. *Biophysical Journal*, 96:4053–4062, 2009. ISSN 15420086. doi: 10.1016/j.bpj.2008.12.3964.

Talita Glaser, Vanessa Fernandes Arnaud Sampaio, Claudiana Lameu, and Henning Ulrich. Calcium signalling: A common target in neurological disorders and neurogenesis. *Seminars in Cell and Developmental Biology*, 95:25–33, 2019. ISSN 10963634. doi: 10.1016/j.semcdb.2018.12.002. URL `https://doi.org/10.1016/j.semcdb.2018.12.002`.

Shane O Grady and Maria P Morgan. Calcium transport and signalling in breast cancer : Functional and prognostic significance. *Seminars in Cancer Biology*, 72:19–26, 2021. ISSN 1044-579X. doi: 10.1016/j.semcancer.2019.12.006. URL `https://doi.org/10.1016/j.semcancer.2019.12.006`.

Jung Min Han, Akihiko Tanimura, Vivien Kirk, and James Sneyd. A mathematical model of calcium dynamics in hsy cells. *PLoS Computational Biology*, 13, 2 2017. ISSN 15537358. doi: 10.1371/journal.pcbi.1005275.

Molly Hawker and Ivo Siekmann. "people" meet "markovians"—individual-based modelling with hybrid stochastic systems. *Journal of Biological Systems*, 2023. doi: 10.1142/S0218339023400028. URL `https://doi.org/10.1142/S0218339023400028`. accepted.

Molly Hawker, Pengxing Cao, James Sneyd, and Ivo Siekmann. A ca^{2+} puff model based on integrodifferential equations, 2024. URL `https://arxiv.org/abs/2401.17326`.

Charlotte L. Hill and Gary J. Stephens. *An Introduction to Patch Clamp Recording*, pages 1–19. Springer US, New York, NY, 2021. ISBN 978-1-0716-0818-0. doi: 10.1007/978-1-0716-0818-0_1. URL `https://doi.org/10.1007/978-1-0716-0818-0_1`.

Katri Hituri and Marja Leena Linne. Comparison of models for ip3 receptor kinetics using stochastic simulations. *PLoS ONE*, 8, 4 2013. ISSN 19326203. doi: 10.1371/journal.pone.0059618.

References

A L Hodgkin and A F Huxley. A quantitative description of membrane current and its application to conduction and excitation in nerve. *Journal of Physiology*, pages 500–544, 1952.

V Ilyin and I Parker. Role of cytosolic ca2+ in inhibition of insp3-evoked ca2+ release in xenopus oocytes. *The Journal of Physiology*, 477(3):503–509, 1994. doi: https://doi.org/10.1113/jphysiol.1994.sp020211. URL `https://physoc.onlinelibrary.wiley.com/doi/abs/10.1113/jphysiol.1994.sp020211`.

Paola Imbrici, Antonella Liantonio, Giulia M. Camerino, Michela De Bellis, Claudia Camerino, Antonietta Mele, Arcangela Giustino, Sabata Pierno, Annamaria De Luca, Domenico Tricarico, Jean-Francois Desaphy, and Diana Conte. Therapeutic approaches to genetic ion channelopathies and perspectives in drug discovery. *Frontiers in Pharmacology*, 7, 2016. ISSN 1663-9812. doi: 10.3389/fphar.2016.00121. URL `https://www.frontiersin.org/journals/pharmacology/articles/10.3389/fphar.2016.00121`.

Md. Shahidul Islam. *Calcium Signaling*. Springer International Publishing, 2nd edition, 2020. ISBN 9783030124564. doi: 10.1007/978-3-030-12457-1.

Hristina Ivanova, Tim Vervliet, Ludwig Missiaen, Jan B. Parys, Humbert De Smedt, and Geert Bultynck. Inositol 1,4,5-trisphosphate receptor-isoform diversity in cell death and survival. *Biochimica et Biophysica Acta - Molecular Cell Research*, 1843:2164–2183, 2014. ISSN 18792596. doi: 10.1016/j.bbamcr.2014.03.007.

Kimberly J. Jasmer, Kristy E. Gilman, Kevin Muñoz Forti, Gary A. Weisman, and Kirsten H. Limesand. Radiation-induced salivary gland dysfunction: Mechanisms, therapeutics and future directions. *Journal of Clinical Medicine*, 9, 2020. URL `https://api.semanticscholar.org/CorpusID:229685532`.

Yong Kang, Lingling Xu, Jinrui Dong, Yongzhi Huang, Xue Yuan, Ruiyan Li, Liqun Chen, Zhen Wang, and Xiaoyuan Ji. Calcium-based nanotechnology for cancer therapy. *Coordination Chemistry Reviews*, 481, 4 2023. ISSN 00108545. doi: 10.1016/j.ccr.2023.215050.

Gopal K Kanji. *100 Statistical Tests*, chapter The Tests. London: SAGE Publications Ltd, 2006.

James Keener and James Sneyd. Membrane ion channels. In *Mathematical Physiology*, pages 121–173. Springer, 2nd edition, 2009. ISBN 9780387758466.

Joel Keizer and Gary De Young. Simplification of a realistic model of ip3-induces ca2+ oscillations. *Journal of Theoretical Biology*, 166:431–442, 1994. doi: 10.1073/pnas.89.20.9895.

Martijn Kerkhofs, Bruno Seitaj, Hristina Ivanova, Giovanni Monaco, Geert Bultynck, and Jan B. Parys. Pathophysiological consequences of isoform-specific ip 3 receptor mutations. *Biochimica et Biophysica Acta - Molecular Cell Research*, 1865:1707–1717, 11 2018. ISSN 18792596. doi: 10.1016/j.bbamcr.2018.06.004.

Zaven S Khachaturian. Hypothesis on the regulation of cytosol calcium concentration and the aginf brain. *Neurobiology of Aging*, 8:345–346, 1987. doi: https://doi.org/10.1016/0197-4580(87)90073-X.

Zaven S. Khachaturian. Introduction and overview. *Annals of the New York Academy of Sciences*, 568:1–4, 1989. ISSN 17496632. doi: 10.1111/j.1749-6632.1989.tb12485.x.

Edda Klipp and Wolfram Liebermeister. Mathematical modeling of intracellular signaling pathways. *BMC Neuroscience*, 7, 10 2006. ISSN 14712202. doi: 10.1186/1471-2202-7-S1-S10.

Benjamin Klocke, Kylie Krone, Jason Tornes, Carter Moore, Hayden Ott, and Pothitos M. Pitychoutis. Insights into the role of intracellular calcium signaling in the neurobiology of neurodevelopmental disorders. *Frontiers in Neuroscience*, 17, 2023. ISSN 1662453X. doi: 10.3389/fnins.2023.1093099.

Paul Kvam, Brani Vidakovic, and Seong-joon Kim. *Nonparametric statistics with applications to science and engineering with R*. Hoboken, New Jersey : Wiley, 2 edition, 2023. ISBN 9781119268130.

Fawcett Lee. Chapter 2 bayes' theorem for distributions, 2014. URL `https://www.mas.ncl.ac.uk/~nlf8/teaching/mas2317/notes/chapter2.pdf`.

M D Leslie and S Dische. Parotid gland function following accelerated and conventionally fractionated radiotherapy. *Radiotherapy and Oncology*, 22:133–139, 1991.

Yue-Xian Li and John Rinzel. Equations for insp3 receptor-mediated [ca2+]i oscillations derived from a detailed kinetic model: A hodgkin-huxley like formalism. *Journal of Theoretical Biology*, 166:461–473, 1994.

References

Q. Y. Liu, F. A. Lai, E. Rousseau, R. V. Jones, and G. Meissner. Multiple conductance states of the purified calcium release channel complex from skeletal sarcoplasmic reticulum. *Biophysical Journal*, 55:415–424, 1989. ISSN 00063495. doi: 10.1016/S0006-3495(89)82835-8.

Jacopo Magistretti and Angel Alonso. Multiple conductance substates in pharmacologically untreated na + channels generating persistent openings in rat entorhinal cortex neurons. *Journal of Membrane Biology*, 214:165–180, 11 2006. ISSN 00222631. doi: 10.1007/s00232-006-0068-4.

Don On Daniel Mak, John E. Pearson, King Pan Campion Loong, Suman Datta, Marisabel Fernández-Mongil, and J. Kevin Foskett. Rapid ligand-regulated gating kinetics of single inositol 1,4,5-trisphosphate receptor ca2+ release channels. *EMBO Reports*, 8:1044–1051, 2007. ISSN 1469221X. doi: 10.1038/sj.embor.7401087.

J. S. Marchant and Ian Parker. Role of elementary ca2+ puffs in generating repetitive ca2+ oscillations. *The EMBO Journal*, 20:65–76, 1 2001. ISSN 14602075. doi: 10.1093/emboj/20.1.65.

Jonathan S. Marchant and Colin W. Taylor. Rapid activation and partial inactivation of inositol trisphosphate receptors by inositol trisphosphate. *Biochemistry*, 37:11524–11533, 8 1998. ISSN 00062960. doi: 10.1021/bi980808k.

Rukmankesh Mehra and Kasper Planeta Kepp. Understanding familial alzheimer's disease: The fit-stay-trim mechanism of γ-secretase. *Wires computational molecular science*, 2021. doi: 10.1002/wcms.1556.

Claude Meunier and Idan Segev. Playing the devil's advocate: Is the hodgkin-huxley model useful? *Trends in Neurosciences*, 25:558–563, 2002. ISSN 01662236. doi: 10.1016/S0166-2236(02)02278-6.

In Jae Myung. Tutorial on maximum likelihood estimation. *Journal of Mathematical Psychology*, 47:90–100, 2003. doi: 10.1016/S0022-2496(02)00028-7.

Erwin Neher and Bert Sakmann. Single-channel currents recorded from membrane of denervated frog muscle fibres. *Nature*, 260:799–802, 1976. doi: https://doi.org/10.1038/260799a0.

Navid Paknejad and Richard K. Hite. Structural basis for the regulation of inositol trisphosphate receptors by ca2+ and ip3. *Nature Structural and*

Molecular Biology, 25:660–668, 8 2018. ISSN 15459985. doi: 10.1038/s41594-018-0089-6.

Suman Panda, Oishika Chatterjee, Laboni Roy, and Subhrangsu Chatterjee. Targeting ca2+ signaling: A new arsenal against cancer. *Drug Discovery Today*, 27:923–934, 3 2022. ISSN 18785832. doi: 10.1016/j.drudis.2021.11.012.

Michael J. Panik. *Advanced statistics from an elementary point of view*. Elsevier Academic Press, 1 edition, 2005. ISBN 0-12-088494-1.

I Parker and Y Yao. Ca2+ transients associated with openings of inositol trisphosphate-gated channels in xenopus oocytes. *The Journal of Physiology*, 491(3):663–668, 1996. doi: https://doi.org/10.1113/jphysiol.1996.sp021247. URL `https://physoc.onlinelibrary.wiley.com/doi/abs/10.1113/jphysiol.1996.sp021247`.

Richard Payne, Thomas M. Flores, and Alan Fein. Feedback inhibition by calcium limits the release of calcium by inositol trisphosphate in limulus ventral photoreceptors. *Neuron*, 4:547–555, 1990. ISSN 08966273. doi: 10.1016/0896-6273(90)90112-S.

Ekaterina Pchitskaya, Elena Popugaeva, and Ilya Bezprozvanny. Calcium signaling and molecular mechanisms underlying neurodegenerative diseases. *Cell Calcium*, 70:87–94, 2018. ISSN 0143-4160. doi: 10.1016/j.ceca.2017.06.008. URL `https://doi.org/10.1016/j.ceca.2017.06.008`.

Matjaž Perc, Anne K. Green, C. Jane Dixon, and Marko Marhl. Establishing the stochastic nature of intracellular calcium oscillations from experimental data. *Biophysical Chemistry*, 132(1):33–38, 2008. ISSN 0301-4622. doi: https://doi.org/10.1016/j.bpc.2007.10.002. URL `https://www.sciencedirect.com/science/article/pii/S0301462207002372`.

John R Pollard, Nelsm Arispe, Eduardo Rojas, and Harvey B Pollard. A geometric sequence that accurately describes allowed multiple conductance levels of ion channels: The "three halves (*Biophysical journal*, 67(2):647–655, 1994. URL `https://doi.org/10.1016/S0006-3495(94)80525-9`.

Stephen Jp Pratt, Erick Hernández-Ochoa, and Stuart S. Martin. Calcium signaling: breast cancer's approach to manipulation of cellular circuitry. *Biophysical Reviews*, 12:1343–1359, 2020. ISSN 18672469. doi: 10.1007/s12551-020-00771-9.

References

David L. Prole and Colin W. Taylor. Structure and function of ip3 receptors. *Cold Spring Harbor Perspectives in Biology*, 11, 2019. ISSN 19430264. doi: 10.1101/cshperspect.a035063.

Hong Qi, Yandong Huang, Sten Rüdiger, and Jianwei Shuai. Frequency and relative prevalence of calcium blips and puffs in a model of small ip3r clusters. *Biophysical Journal*, 106:2353–2363, 6 2014. ISSN 15420086. doi: 10.1016/j.bpj.2014.04.027.

Taufiq Rahman and Colin W. Taylor. Dynamic regulation of ip3 receptor clustering and activity by ip3. *Channels*, 3:226–232, 2009. ISSN 19336969. doi: 10.4161/chan.3.4.9247.

Behnaz Rahmani, Samuel Jelbart, Vivien Kirk, and James Sneyd. Understanding broad-spike oscillations in a model of intracellular calcium dynamics. 1 2024. URL `http://arxiv.org/abs/2401.16839`.

Raffael Bechara Rameh, Elizabeth M. Cherry, and Rodrigo Weber dos Santos. Single-variable delay-differential equation approximations of the fitzhugh-nagumo and hodgkin-huxley models. *Communications in Nonlinear Science and Numerical Simulation*, 82, 3 2020. ISSN 10075704. doi: 10.1016/j.cnsns.2019.105066.

Lynn A. Raymond. Striatal synaptic dysfunction and altered calcium regulation in huntington disease. *Biochemical and Biophysical Research Communications*, 483:1051–1062, 2 2017. ISSN 0006-291X. doi: 10.1016/J.BBRC.2016.07.058.

Chiara Di Resta and Andrea Becchetti. Introduction to ion channels. *Advances in experimental medicine and biology*, 2012. doi: 10.1007/978-1-4419-6066-5_2.

Andre S. Ribeiro. Stochastic and delayed stochastic models of gene expression and regulation. *Mathematical Biosciences*, 223:1–11, 2010. ISSN 00255564. doi: 10.1016/j.mbs.2009.10.007. URL `http://dx.doi.org/10.1016/j.mbs.2009.10.007`.

Fathalla A Rihan. *Delay Differential Equations and Applications to Biology*. Springer, 2021. ISBN 978-981-16-0625-0. doi: https://doi.org/10.1007/978-981-16-0626-7. URL `http://www.springer.com/series/13386`.

Alex Rodriguez and Alessandro Laio. Clustering by fast search and find of density peaks. *Science*, 344(6191):1492–1496, 2014. doi: 10.1126/science.

1242072. URL https://www.science.org/doi/abs/10.1126/science.1242072.

Martin Rückl, Ian Parker, Jonathan S Marchant, Chamakuri Nagaiah, Friedrich W Johenning, and Sten Rüdiger. Modulation of elementary calcium release mediates a transition from puffs to waves in an ip 3 r cluster model. *PLoS Computational Biology*, 11, 2015. doi: 10.1371/journal.pcbi.1003965.

Sten Rüdiger. Stochastic models of intracellular calcium signals. *Physics Reports*, 534:39–87, 2013. ISSN 0370-1573. doi: 10.1016/j.physrep.2013.09.002. URL http://dx.doi.org/10.1016/j.physrep.2013.09.002.

Sten Rüdiger and Jianwei Shuai. Modeling of stochastic ca2+ signals. In *Computational Glioscience*, pages 91–114. Springer International Publishing, 2019. ISBN 9783030008178. doi: 10.1007/978-3-030-00817-8. URL http://dx.doi.org/10.1007/978-3-030-00817-8_4.

Gideon Schwarz. Estimating the dimension of a model. *The Annals of Statistics*, 6:461–464, 1978.

Jianwei Shuai, Heather J. Rose, and Ian Parker. The number and spatial distribution of ip3 receptors underlying calcium puffs in xenopus oocytes. *Biophysical Journal*, 91:4033–4044, 2006. ISSN 00063495. doi: 10.1529/biophysj.106.088880.

Ivo Siekmann, Larry E Wagner Ii, David Yule, Colin Fox, David Bryant, and Edmund J Crampin. Mcmc estimation of markov models for ion channels. *Biophysical Journal*, 100:1919–1929, 2011. ISSN 0006-3495. doi: 10.1016/j.bpj.2011.02.059. URL http://dx.doi.org/10.1016/j.bpj.2011.02.059.

Ivo Siekmann, Larry E Wagner II, David Yule, Edmund J Crampin, and James Sneyd. A kinetic model for type i and ii ip 3 r accounting for mode changes. *Biophysical Journal*, 103:658–668, 2012. doi: 10.1016/j.bpj.2012.07.016.

Ivo Siekmann, James Sneyd, and Edmund J Crampin. Statistical analysis of modal gating in ion channels. *Proceedings of the Royal Society A: Mathematical, Physical and Engineering Sciences*, 470, 2014. doi: https://doi.org/10.1098/rspa.2014.0030.

Ivo Siekmann, Mark Fackrell, J Crampin, and Peter Taylor. Modelling modal gating of ion channels with hierarchical markov models. *Proceedings of the*

References

Royal Society A: Mathematical, Physical and Engineering Sciences, 472, 2016. doi: http://dx.doi.org/10.1098/rspa.2016.0122.

Ivo Siekmann, Pengxing Cao, James Sneyd, and Edmund J Crampin. Data-driven modelling of the inositol trisphosphate receptor (ip3r) and its role in calcium-induced calcium release (cicr). In *Computational Glioscience*, pages 39–67. Springer International Publishing, 2019. ISBN 9783030008178. doi: 10.1007/978-3-030-00817-8. URL `http://dx.doi.org/10.1007/978-3-030-00817-8_2`.

Alexander Skupin and Martin Falcke. Statistical analysis of calcium oscillations. *The European Physical Journal Special Topics*, 187:231–240, 2010. doi: 10.1140/epjst/e2010-01288-9.

Ian F Smith, Steven M. Wiltgen, and Ian Parker. Localization of puff sites adjacent to the plasma membrane; functional and spatial characterization of ca2+ signaling in sh- sy5y cells utilizing membrane-permeant caged ip3. *Cell Calcium*, 45:65–76, 2009. ISSN 15378276. doi: 10.1016/j.ceca.2008.06.001.Localization.

J. Sneyd, M. Falcke, J. F. Dufour, and C. Fox. A comparison of three models of the inositol trisphosphate receptor. *Progress in Biophysics and Molecular Biology*, 85:121–140, 6 2004. ISSN 00796107. doi: 10.1016/j.pbiomolbio.2004.01.013.

James Sneyd, Jung Min Han, Liwei Wang, Jun Chen, Xueshan Yang, Akihiko Tanimura, Michael J. Sanderson, Vivien Kirk, and David I. Yule. On the dynamical structure of calcium oscillations. *Proceedings of the National Academy of Sciences of the United States of America*, 114:1456–1461, 2017. ISSN 10916490. doi: 10.1073/pnas.1614613114.

Stan-Development-Team. *Stan Modeling Language Users Guide and Reference Manual*. 2.28 edition, 2019. URL `https://mc-stan.org`.

Stan-Development-Team. Rstan: the r interface to stan., 2020. URL `http://mc-stan.org/`.

David A. Stephens. Maximum likelihood estimation, 2004. URL `https://www.ma.imperial.ac.uk/~das01/MyWeb/M2S1Previous/2004/Handouts/Mle.pdf`.

D. Swaminathan, G. Ullah, and P. Jung. A simple sequential-binding model for calcium puffs. *Chaos*, 19, 2009. ISSN 10541500. doi: 10.1063/1.3152227.

Karl Swann. Sperm-induced ca2+ release in mammalian eggs: The roles of plcζ, insp3, and atp. *Cells*, 12, 12 2023. ISSN 20734409. doi: 10.3390/cells12242809.

Stèphane Swillens, Laurent Combettest, and Philippe Champeil. A model based on regulatory ca2+ - binding sites along the permeation pathway pcdom-ccyto. *Proceedings of the National Academy of Sciences of the United States of America*, 91:10074–10078, 1994.

Stèphane Swillens, Geneviève Dupont, Laurent Combettes, and Philippe Champeil. From calcium blips to calcium puffs: Theoretical analysisof the requirements for interchannel communication. *PNAS*, 1999. URL `www.pnas.org`.

Allison Tambeaux, Yuriana Aguilar-Sánchez, Demetrio J. Santiago, Madeleine Mascitti, Karyn M. DiNovo, Rafael Mejía-Alvarez, Michael Fill, S. R. Wayne Chen, and Josefina Ramos-Franco. Ligand sensitivity of type-1 inositol 1,4,5-trisphosphate receptor is enhanced by the d2594k mutation. *Pflugers Archiv European Journal of Physiology*, 5 2023. ISSN 14322013. doi: 10.1007/s00424-023-02796-x.

C W Taylor and A J Laude. Ip3 receptors and their regulation by calmodulin and cytosolic ca2+. *Cell Calcium*, 32:321–334, 2002. doi: 10.1016/S0143-4160(02)00185-9.

Pieter Rein ten Wolde, Nils B. Becker, Thomas E. Ouldridge, and Andrew Mugler. Fundamental limits to cellular sensing. *Journal of Statistical Physics*, 162:1395–1424, 3 2016. ISSN 00224715. doi: 10.1007/s10955-015-1440-5.

Leyla Y. Teos, Yu Zhang, Ana P. Cotrim, William Swaim, Jon H. Won, Julian Ambrus, Long Shen, Lolita Bebris, Margaret Grisius, Shyh Ing Jang, David I. Yule, Indu S. Ambudkar, and Ilias Alevizos. Ip3r deficit underlies loss of salivary fluid secretion in sjögrens syndrome. *Scientific Reports*, 5, 9 2015. ISSN 20452322. doi: 10.1038/srep13953.

Lara E. Terry, Kamil J. Alzayady, Amanda M. Wahl, Sundeep Malik, and David I. Yule. Disease-associated mutations in inositol 1,4,5-trisphosphate receptor subunits impair channel function. *Journal of Biological Chemistry*, 295:18160–18178, 2020. ISSN 1083351X. doi: 10.1074/jbc.RA120.015683. URL `http://dx.doi.org/10.1074/jbc.RA120.015683`.

References

E. C. Thrower, H. Mobasheri, S. Dargan, P. Marius, E. J.A. Lea, and A. P. Dawson. Interaction of luminal calcium and cytosolic atp in the control of type 1 inositol (1,4,5)-trisphosphate receptor channels. *Journal of Biological Chemistry*, 275:36049–36055, 11 2000. ISSN 00219258. doi: 10.1074/jbc.M000970200.

Kevin Thurley and Martin Falcke. Derivation of ca2+ signals from puff properties reveals that pathway function is robust against cell variability but sensitive for control. *PNAS*, 108:427–432, 2011. doi: 10.1073/pnas.1008435108.

Kevin Thurley, Ian F Smith, Stephen C Tovey, Colin W Taylor, Ian Parker, and Martin Falcke. Timescales of ip 3 -evoked ca2+ spikes emerge from ca2+ puffs only at the cellular level. *Biophysical Journal*, 101:2638–2644, 2011. ISSN 0006-3495. doi: 10.1016/j.bpj.2011.10.030. URL `http://dx.doi.org/10.1016/j.bpj.2011.10.030`.

Kevin Thurley, Alexander Skupin, Rüdiger Thul, and Martin Falcke. Fundamental properties of ca2+ signals. *Biochimica et Biophysica Acta - General Subjects*, 1820:1185–1194, 2012. ISSN 03044165. doi: 10.1016/j.bbagen.2011.10.007. URL `http://dx.doi.org/10.1016/j.bbagen.2011.10.007`.

Agne Tilūnaitė, Wayne Croft, Noah Russell, Tomas C. Bellamy, and Rüdiger Thul. A bayesian approach to modelling heterogeneous calcium responses in cell populations. *PLoS Computational Biology*, 13, 10 2017. ISSN 15537358. doi: 10.1371/journal.pcbi.1005794.

P. Tiraboschi, L. A. Hansen, L. J. Thal, and J. Corey-Bloom. The importance of neuritic plaques and tangles to the development and evolution of ad. *Neurology*, 62(11):1984–1989, 2004. doi: 10.1212/01.WNL.0000129697.01779.0A. URL `https://www.neurology.org/doi/abs/10.1212/01.WNL.0000129697.01779.0A`.

Benjamin Chun Kit Tong, Aston Jiaxi Wu, Min Li, and King Ho Cheung. Calcium signaling in alzheimer's disease & therapies. *Biochimica et Biophysica Acta - Molecular Cell Research*, 1865:1745–1760, 2018. ISSN 18792596. doi: 10.1016/j.bbamcr.2018.07.018. URL `https://doi.org/10.1016/j.bbamcr.2018.07.018`.

Aslak Tveito and Glenn T Lines. *Computing Characterizations of Drugs for Ion Channels and Receptors Using Markov Models*. Springer Open, 2016. ISBN 9783319300290. doi: https://doi.org/10.1007/978-3-319-30030-6.

Ghanim Ullah, Peter Jung, and Khaled Machaca. Modeling ca2+ signaling differentiation during oocyte maturation. *Cell Calcium*, 42:556–564, 2007. ISSN 01434160. doi: 10.1016/j.ceca.2007.01.010.

Ghanim Ullah, Don on Daniel Mak, and John E Pearson. A data-driven model of a modal gated ion channel : The inositol 1 , 4 , 5-trisphosphate receptor in insect sf9 cells. *The Journal of General Physiology*, 140:159–173, 2012a. doi: 10.1085/jgp.201110753.

Ghanim Ullah, Ian Parker, Don On Daniel Mak, and John E. Pearson. Multiscale data-driven modeling and observation of calcium puffs. *Cell Calcium*, 52:152–160, 2012b. ISSN 15321991. doi: 10.1016/j.ceca.2012.04.018.

Aki Vehtari, Andrew Gelman, and Jonah Gabry. Practical bayesian model evaluation using leave-one-out cross-validation and waic. *Statistics and Computing*, 27:1413–1432, 2017. ISSN 15731375. doi: 10.1007/s11222-016-9696-4.

Tomáš Vejchodský, Radek Erban, and Philip K. Maini. Reduction of chemical systems by delayed quasi-steady state assumptions. *arXiv: Dynamical Systems*, 6 2014. URL `http://arxiv.org/abs/1406.4424`.

Carlos A. Villalba-Galea and Alvin T. Chiem. Hysteretic behavior in voltage-gated channels. *Frontiers in Earth Science*, 11, 11 2020. ISSN 22966463. doi: 10.3389/fphar.2020.579596.

Larry E. Wagner and David I. Yule. Differential regulation of the insp3 receptor type-1 and -2 single channel properties by insp3, ca2+ and atp. *Journal of Physiology*, 590:3245–3259, 2012. ISSN 00223751. doi: 10.1113/jphysiol.2012.228320.

Sumio Watanabe. Asymptotic equivalence of bayes cross validation and widely applicable information criterion in singular learning theory. *Journal of Machine Learning Research*, 11:3571–3594, 2010. ISSN 15324435.

Liyong Wu, Pedro Rosa-Neto, Ging-Yuek R. Hsiung, A. Dessa Sadovnick, Mario Masellis, Sandra E. Black, Jianping Jia, and Serge Gauthier. Early-onset familial alzheimer's disease (eofad). *Canadian Journal of Neurological Sciences*, 39(4):436–445, 2012. doi: 10.1017/S0317167100013949.

Yong Yao, John Choi, and Ian Parker. Quantal puffs of intracellular ca2+ evoked by inositol trisphosphate in xenopus oocytes. *Journal of Physiology*, 482:533–553, 1995. doi: 10.1113/jphysiol.1995.sp020538.